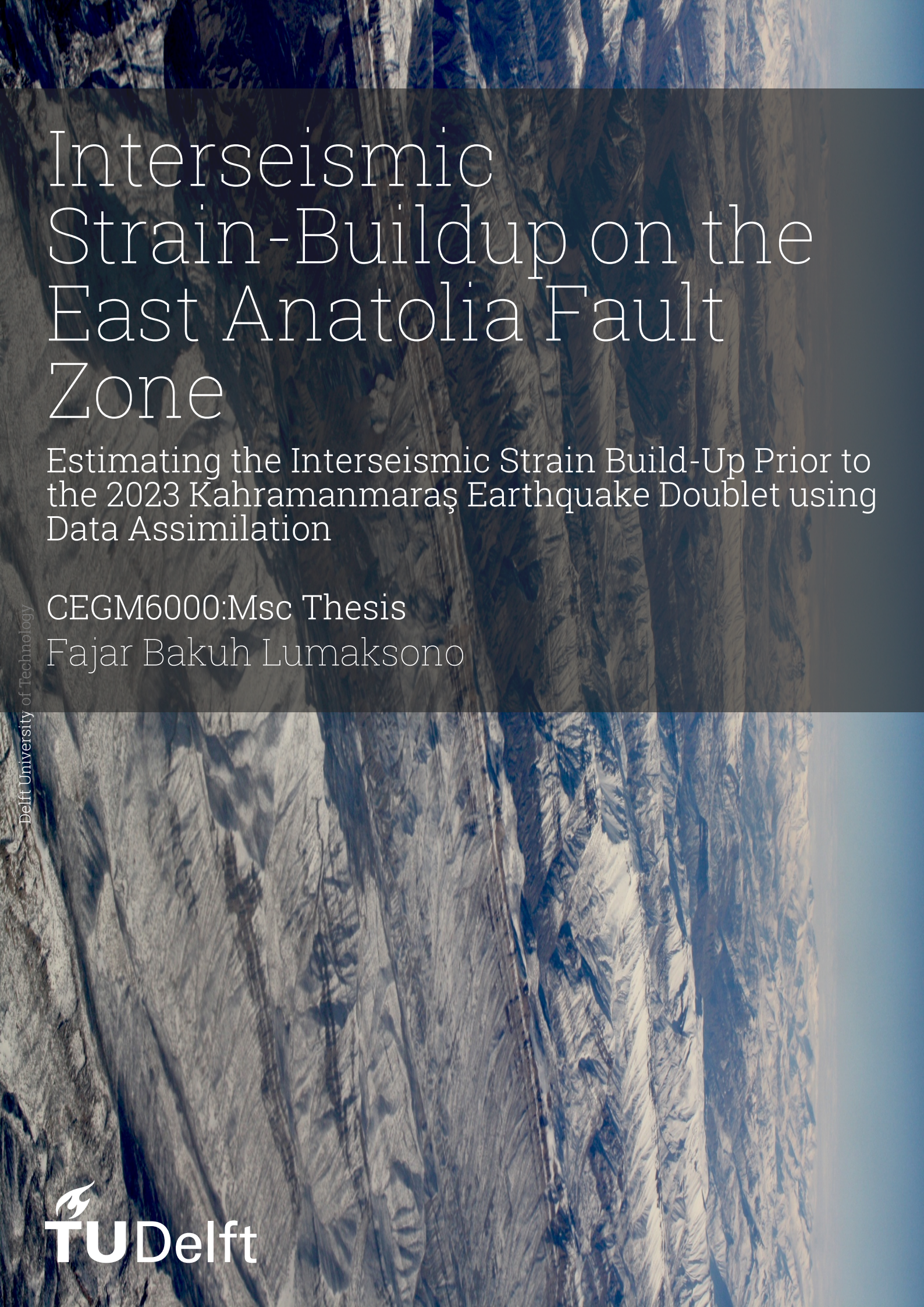

Interseismic Strain-Buildup on the East Anatolia Fault Zone

Estimating the Interseismic Strain Build-Up Prior to the 2023 Kahramanmaraş Earthquake Doublet using Data Assimilation

CEGM6000:Msc Thesis

Fajar Bakuh Lumaksono

Delft University of Technology

TU Delft

Interseismic Strain-Buildup on the East Anatolia Fault Zone

Estimating the Interseismic Strain Build-Up Prior to the 2023 Kahramanmaraş Earthquake Doublet using Data Assimilation

by

Fajar Bakuh Lumaksono

Fajar Bakuh Lumaksono

6068502

Main Supervisor:	Dr.ir. D.B.T. Broerse
Supervisor I:	Dr.sc.nat. Max Ramgraber
Advisor :	Dr. Rob Govers
Faculty :	Faculty of Civil Engineering and Geosciences, Delft

Cover:	Taurus Mountain Range (Photo by milapalim on Flickr, used with permission.)
Style:	TU Delft Report Style, with modifications by Daan Zwaneveld

TU Delft

Preface

Preface

I want to say thank you to everyone who has been involved in this project. I am very grateful for these past six months conducting studies on the interseismic strain build-up prior to the Kahramanmaraş earthquake doublet. I learned a lot about the theory behind the phenomena. The slip deficit, strain build-up, and how to use data assimilation. But most importantly, I learned how to do research almost from the ground up. I remember that I really started from scratch in this research, faced many challenges throughout this project, both academically and non-academically. Academically, the model set-up was far more challenging than I expected, and I had difficulties even until the middle part of this project. But my supervisors believed that I was able to do it, and they gladly offered their help and insight to help me overcome the challenges.

I am very thankful to both of my supervisors, Dr Ir. Taco Broerse and Dr. M.Sc. nat. Max Ramgraber. They sincerely guided me through challenges, providing clear directions and believing in me to deliver the results of this thesis. I also want to mention Dr Rob Govers for his input on this project, as his insight has been very valuable for this project from the start. They provided valuable insight, especially for my academic writing, which has never been my forte, and I learned so much from them.

I hope the insight from this research can make a valuable contribution to humanity. I come from Indonesia, where earthquakes occur almost every year, and I have seen firsthand how an earthquake can devastate a region. So, it is my desire that this research helps us to gain more understanding about this type of event. I also want to give my appreciation to the friends and staff at TU Delft. The academic staff has created a fantastic learning environment, while my friends, in particular from the Earth Observations track, Snellius, and PPI (Indonesian Student Association) at Delft, have made this journey much more enjoyable. I am also grateful to my sponsor, LPDP, who has also provided financial backing throughout my academics and to my parents and sister, who supported me throughout the process up till the end of my thesis. I only wish I had more time because I genuinely loved doing this research, albeit with all the challenges. I must also admit that there remain many aspects that could be improved, both in this project and in myself as a person.

This thesis overall has been an incredible journey, one that I will not forget. The struggles of facing new challenges and problems during the thesis, but also the moments of brilliance when good results were achieved. I hope this thesis is not the end of my journey, but rather the beginning of a path to pursue truth and knowledge, and to share them for the benefit of humanity.

Abstract

On February 9, 2023, two significant earthquakes of magnitudes $M_w7.8$ and $M_w7.7$ struck southern Turkey, devastating the Kahramanmaraş region, causing nearly 50,000 fatalities, and displacing millions of people (Zhang et al., 2023). The first earthquake ruptured the Nurdağı–Pazarcık Fault, a subsidiary of the East Anatolian Fault Zone (EAFZ), while the second occurred about 90 km away on the Çardak–Sürgü Fault. This event later became known as the Kahramanmaraş earthquake doublet. With a combined magnitude of M_w8, it represents the largest recorded continental strike-slip earthquake sequence. The main strand of the EAFZ is a well-known seismically active zone, with many seismic records and studies that has been conducted on the area. In contrast, the earthquake on the Çardak–Sürgü Fault was unexpected, as it had remained quiet for several centuries. This has left the Çardak–Sürgü Fault relatively understudied compared to the main strand of the EAFZ, particularly in terms of its kinematics and seismic risk.

In this study, we estimate the slip deficit along the main strand of the East Anatolian Fault Zone (EAFZ) and the Çardak–Sürgü Fault prior to the Kahramanmaraş earthquake doublet, using elastic strike-slip and dip-slip models combined with data assimilation. We find that the slip-deficit rates for the EAFZ are estimated at 2–8 mm/yr in the Anatolia-fixed frame and 0–11 mm/yr in the Arabia-fixed frame. For the Çardak–Sürgü Fault, slip-deficit rates are 1–4 mm/yr in the Anatolia-fixed frame and 2–11 mm/yr in the Arabia-fixed frame. Dip-slip rates show wider variability. Along the EAFZ, they range from 0 to –12 mm/yr in the Anatolia-fixed frame and from –12 to 2 mm/yr in the Arabia-fixed frame. For the Çardak–Sürgü Fault, dip-slip rates range from –4 to 5.5 mm/yr in the Anatolia-fixed frame and from –3 to 10 mm/yr in the Arabia-fixed frame.

To further evaluate our estimates, we compared the interseismic slip deficit with coseismic slip distributions from the 2023 Kahramanmaraş earthquakes. The results indicate that the estimated slip deficit is broadly consistent with the observed coseismic slip for the Amanos and Çardak segments, but underestimates slip for the Pazarcık, Erkenek, and Göksun segments. A key limitation of the approach is that the locking depth remains poorly constrained in the joint inversion, particularly when using GNSS velocities in the Arabia-fixed frame rather than the Anatolia-fixed frame. In addition, the choice of kinematic representation for the joint fault mechanism exerts a strong influence on the results, leading to notable differences in the estimated slip deficit.

Keywords: Slip deficit, East Anatolia Fault Zone, Çardak–Sürgü Fault, Locking depth, Interseismic, Data assimilation

Contents

List of Figures

List of Tables

Nomenclature

Abbreviations

Abbreviation	Definition
NAFZ	North Anatolia Fault Zone
EAFZ	East Anatolia Fault Zone
EnKF	Ensemble Kalman Filter
EnKS	Ensemble Kalman Smoother
AEM	Analytic Element Method
MF	Malatya Fault
TF	Tuzgolu Fault
DSFZ	Dead Sea Fault Zone
ENU	East - North - Up
ECEF	Earth Centred, Earth Fixed

Symbols

Symbol	Definition	Unit
v	Velocity	[m/s]
ρ	Density	[kg/m^3]
A	Cross-sectional area	[m^2]
$F\perp$	Force	[N]
l_0	Original length of the specimen	[m]
Y	Young's modulus (modulus of elasticity)	[Pa]
N	Ensemble Members	
V_s	Slip-Rate	[mm/year]
V_d	Dip-Slip Rate	[mm/year]
D	Locking Depth	[kilometer]
δ	Dip Angle	[degree (^{o})]
θ_{rot}	Rotation Rate	[mm/year/km]
M_w	Moment Magnitude	
R_{enu}	Rotation Matrix from ECEF to ENU	
T	Coordinate Transformation Matrix	
ϕ	Angle	[degree($^\circ$)]
Δ	Gradient	

1

Introduction

1.1. Introduction

Earthquakes are among the most destructive natural hazards, capable of causing severe damage and widespread catastrophe. Throughout history, we have seen how earthquakes devastated a region, from the 1906 San Francisco earthquakes that caused nearly 30,000 deaths and half of population displaced from their homes (Zoback, 2006); the 2004 Indian Ocean earthquakes and tsunami that reached 224,000 fatalities and obliterated the coastal area in the Southeast Asia (Rossetto et al., 2007); the 2011 Tohoku earthquakes in Japan that generated a 10 m tsunami leading to nearly 20,000 life loss and hundreds of house destroyed (Uchida & Bürgmann, 2021); and the 2021 Haiti earthquakes that resulted in 2,200 fatalities and effected million of people (Miyamoto et al., 2024). Together, these four events accounted for more than 250,000 deaths and millions of casualties worldwide, underlining the catastrophic potential of large-magnitude earthquakes.

More recently, on February 9 2023, two earthquakes with a moment magnitude of $M_w 7.8$ and $M_w 7.7$ struck the region of southern Turkey. This incident left the Kahramanmaraş region fatally destroyed, causing a death toll of up to 50,000 and leaving millions of people displaced from their homes (Zhang et al., 2023). The first $M_w 7.8$ earthquake struck the Kahramanmaraş region, with its epicentre located approximately 40 km south of the city, along the Nurdağı–Pazarcık Fault (NPF), a subsidiary fault of the East Anatolian Fault. The observed peak coseismic slip for the first earthquake is recorded around 8 m near the Pazarcık segments. Nine hours later, a second earthquake of magnitude $M_w 7.7$ ruptured the Çardak–Sürgü fault, about 95 km north of the first event, on the northern side of the EAFZ main strand, with a more concentrated coseismic slip that reached up to 10 m, as reported by Jia et al. (2023). The $M_w 7.8$ earthquake reportedly ruptured three primary fault segments, namely the Amanos, Pazarcık, and Erkenek, as well as the two secondary faults, the Nurdagi and Yarbasi and the $M_w 7.7$ earthquake ruptured four fault segments, the Göksun, Sürgü, Çardak, and Maras Fault (Zhang et al., 2023).

Combined, these two earthquakes managed to reach a total moment magnitude of $M_w 8$, which was recorded as the biggest magnitude earthquake in terms of continental strike-slip fault. This event would later be known as the Kahramanmaraş doublet earthquake, as two concurrent earthquakes occurred almost simultaneously in time, and the locations between them are only 90 km apart. Consecutive earthquakes occurring in time and space proximity are rare, since a mainshock is usually followed only by aftershocks, which typically have lower magnitudes than the main event. Before this event, the main strand of the East Anatolia Fault Zone(EAFZ) had already experienced numerous seismic events and therefore been the focus of several studies, as evidenced by the 1513 Pazarcık, 1822 Antakya, 1893 Çelikhan, 1905 Pütürge, and 1971 Bingöl earthquakes (Duman & Emre, 2013; Taymaz et al., 1991), and more recently the Elazığ earthquake in 2020 (Pousse-Beltran et al., 2020). On the other hand, the second $M_w 7.6$ is not well accounted for, as the Çardak–Sürgü Fault has been relatively understudied, with historical sources indicating its last major ruptures occurred in 1544, while Guidoboni et al. (1994) also reports an event in 584 along the Çardak segments. Although several earthquakes have occurred in the past hundred years, almost none have exceeded a magnitude of $M_w 6$ in the Çardak–Sürgü area

according to data from the Boğaziçi University Kandilli Observatory and Earthquake Research Institute National Earthquake Monitoring Centre (KOERI-RETMC, 2021). Because these events have generally been small and treated as negligible, research on the Çardak–Sürgü segments has remained limited, leaving their seismic potential and kinematics insufficiently characterised (Koç & Kaymakcı, 2013).

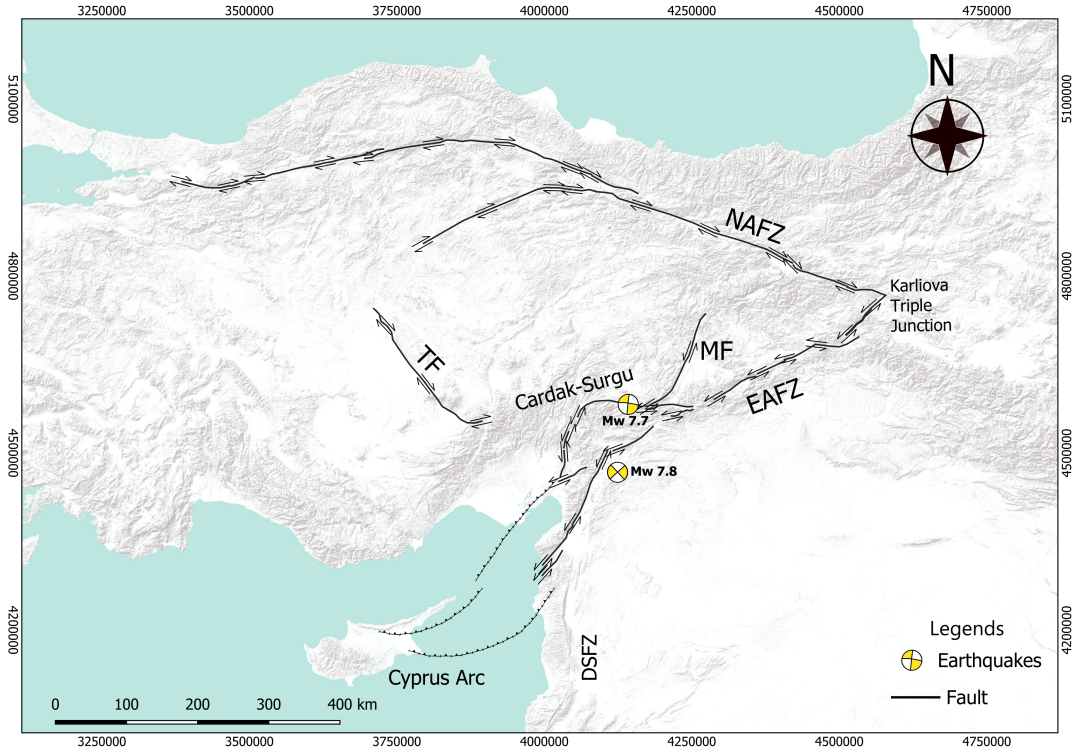

Figure 1.1: Region of Southern Turkey. Fault data from Styron and Pagani (2020), moment tensors obtained from U.S. Geological Survey (n.d.).

The east Anatolia region is home to several fault segments, the most prominent of which are the East Anatolia Fault Zone (EAFZ) and its counterpart, the North Anatolia Fault Zone (NAFZ). Duman and Emre (2013) states that the EAFZ comprises multiple fault segments and bends, with strike orientations ranging from east-west to approximately N75 ° E. Besides the main faults of the East Anatolia Fault and the North Anatolia Fault, the Anatolia Plate also has multiple branches of faults, such as the Tuzgölü, Malatya, and one of the faults that hosts the second earthquake, the Çardak–Sürgü Fault.

It was suspected that the Kahramanmaraş doublet earthquake was driven by the interaction along a segment of the plate boundary that remained mechanically locked during the interseismic period. During an earthquake, the locked portion of the fault interface ruptured, allowing sudden slip along the plate boundary and releasing the accumulated strain through elastic rebound (Govers et al., 2018). The phenomenon of interlocking at fault lines, which predominantly occurs at plate boundaries, causes motion near the fault to lag behind the far-field displacement of the plates (Herman et al., 2018). This difference between the imposed tectonic displacement and the actual fault slip is known as the slip deficit.

Slip deficit arises from the interlocking mechanism that takes place several kilometres beneath the Earth's surface. Despite modern technological advances, it remains impossible to observe the subsurface movement directly, especially at such depth. Thus, to approach this problem, several models have been developed to link the geodetic measurements to the slip-deficit mechanism occurring beneath the surface. These models provide a crucial connection between the measurements obtained from various observational techniques, such as InSAR, GNSS, and levelling, which primarily capture the Earth's surface deformation, to the underlying slip deficit mechanism occurring beneath the Earth's surface. By using these models, we can better understand the slip-deficit mechanism. The study of slip

deficit itself has been conducted since the 1970s, as can be seen from the research done by Savage and Burford (1973) that provides the 2D screw dislocation model. The 2D screw dislocation model treats the strike-slip fault as infinitely long in an elastic half-space and assumes the fault is locked at a certain depth below the surface. Significant modifications to the models have been made since the introduction of the 2D screw dislocation model for estimating the slip deficit. A prominent example of the modified model is the work of Hussain et al. (2018) in estimating the North Anatolia Fault Zone slip deficit. In his research, Hussain et al. (2018) adds the rotational term to take into account the internal rotation rate of the Anatolia plate and the static offset to have zero velocity on the plates that were taken as a reference in measuring the slip deficit. The rotational terms are applied because it has been indicated from (Kurt et al., 2023) that there is an internal rotational effect on the Anatolia Plate.

Before the Kahramanmaraş earthquake doublet, several studies were also conducted to understand how the slip-deficit in this region behaves. The study of the slip-deficit is derived from the geodetic measurements and geological studies. Based on geodetic and geological studies, it's been found that the main strand of EAFZ has slip deficits ranging from $9-10$ mm/year in the Kahramanmaraş region and 3 mm/year in the southern part of the EAFZ (Aktug et al., 2016; Koç & Kaymakcı, 2013). Reilinger et al. (2006) also shows a $9-10$ mm/year in the main strand part of the East Anatolia fault and systematically decreases towards the west part of the fault.

These results are also coherent with more recent studies provided from Kurt et al. (2023), which indicates that the EAFZ shows a slip deficit around $9-10$ mm/year. As previously noted, there has been limited research on the Çardak–Sürgü Fault, particularly before the Kahramanmaraş earthquake. This is mainly because the fault has remained inactive for the past 500 years, and as stated before, there are no earthquakes that exceeded a magnitude of M_w6(KOERI-RETMC, 2021); the occurrence of the $M_w7.6$ event was therefore not anticipated. This earthquake has highlighted the need for further study of the kinematics and potential of the Çardak–Sürgü Fault, underscoring the importance of more thorough investigations of its segments to better understand the potential risks and hazards they pose to the surrounding region. Two studies examining the kinematics of the Çardak–Sürgü Fault, conducted after the Kahramanmaraş earthquake doublet that also include analyses of the main strand of the EAFZ, were conducted by Vavra et al. (2024) and Özbey et al. (2024). The slip-deficit of the EAFZ, especially in the western segment of the EAFZ, from the Amanos to the Erkenek segments, has been reported to range from 2.0–5.0 mm/year, while the Çardak–Sürgü fault is estimated to experience a slip deficit of approximately 4.0 mm/year (Vavra et al., 2024). While Özbey et al. (2024) estimates a slip deficit of around 5.0 mm/year for the western EAFZ and around 2.0 mm/year for the Çardak fault, their kinematic framework suggests that the Çardak fault continues into the Malatya Fault rather than the Sürgü Fault. These previous observations highlight both the variability and the uncertainties in slip-deficit estimates across the EAFZ and its connected faults. While they provide important context, they also emphasise the need for a more comprehensive framework capable of jointly evaluating the EAFZ and the Çardak–Sürgü fault.

The main objective of this research is to identify the slip deficit that occurred in the Kahramanmaraş during the interseismic period, particularly in the segments affected by the earthquake doublet at the end of the interseismic period, and to identify how the main strand of EAFZ and the Çardak–Sürgü fault contribute to this mechanism, especially the Çardak–Sürgü fault, since the kinematics and the slip deficit that occur in that area are relatively understudied. In this research, we will use the approach of Savage and Burford (1973). Savage and Burford (1973) provides a framework for estimating slip deficit using a simple elastic model, which will be the model that we use in this research. The estimated slip deficit will be determined, and its correlation with the recent earthquakes will be evaluated. In this study, the slip deficit will be estimated using an inversion approach. Specifically, we employ an inversion estimation framework based on data assimilation. Data assimilation is a sequential statistical estimation methodology for incorporating observations into numerical models, in order to obtain an improved description of the evolving state of a system (Evensen et al., 2022). This approach will help estimate the target parameters and assess the suitability of data assimilation methods for such applications. Specifically, this research aims to use a joint inversion on both faults simultaneously, thus incorporating the effects of both the EAFZ and the Çardak–Sürgü. Moreover, the study will explore how the estimated slip deficits align with those observed coseismic slip during the 2023 Kahramanmaraş earthquake. By increasing our understanding of these slip-deficit events, the findings will ultimately support safety initiatives and preventive measures for the community and activities in the affected

regions.

1.2. Research Question(s)

In line with the problem statement in the introduction part, the main research question is formulated as such.

Main Question : **What is the estimated slip deficit rate along the East Anatolian Fault Zone and the Çardak–Sürgü Fault during the interseismic period, and how does it align with the 2023 Kahramanmaraş doublet?**

Question 1 What is the estimated slip-deficit rate along the main strand of EAFZ and Çardak–Sürgü Fault during the interseismic period?

Question 2 How well does each model set-up fit the observation data for this research?

Question 3 How does the estimated slip-deficit align with the 2023 Kahramanmaraş earthquake doublet?

1.3. Thesis outline

This research is organised as follows: Chapter 2 will provide a literature review that outlines the theoretical foundations of the study area, seismic cycle, and fault kinematics. Chapter 3 outlines the data that will be used in this research. Chapter 4 introduces the model that we used for this research. In Chapter 5, we will describe the methodologies used, as well as the steps taken to address the research problem and how to invert both faults at the same time using data assimilation. Chapter 6 reports the results obtained from the applied methodologies and discussion, while Chapter 7 provides the discussion from the final. Finally, an appendix is included to support the main text.

2

Literature Review

2.1. Study Area and Research Background

The study area of this research is in Turkey, specifically in the southern region of Turkey. Other research would sometimes call this region the East Anatolia, as shown in Ergintav et al. (2023). This region has been the subject of studies for understanding plate tectonics due to the existence of the plate boundaries between the Arabian, Anatolian, and Eurasian Plates and their numerous records of seismic activity. The Anatolian Sub-Plate is a continental block situated between the Arabian and Eurasian plates. Its southern boundary interacts with the Arabian Plate, while its eastern boundary is in contact with the Eurasian Plate.

Multiple fault systems confine this region, including the North Anatolia Fault Zone (NAFZ), East Anatolia Fault Zone (EAFZ), and several minor faults such as the Çardak–Sürgü Fault, Malatya Fault (MF), Tuzgolu Fault (TF), Cyprus Arc, and South Anatolia Thrust Zone. The kinematic character of this region is primarily governed by two mechanisms: the Hellenic–Cyprus subduction zone and the continental collision between the Arabian and Eurasian plates in the west (Balkaya et al., 2023; Duman & Emre, 2013; Reilinger et al., 2006). The latter collision has induced left-lateral strike-slip motion along the EAFZ, while the boundary between the Eurasian and Anatolian plates accommodates right-lateral strike-slip motion along the NAFZ. The Anatolia sub-plate shows an increase in velocities towards the Hellenic and Cyprus arc subduction zone. These observations indicate that the subduction of the Eurasian Plate beneath the African Plate is the primary driver of the Anatolian Plate kinematics, which caused the Anatolian Plate to have a west/southwest movement by a counterclockwise rotation. Previous research has shown that the Anatolian plate moves at a rate of ≈20 – 25 mm/year relative to the Eurasia plate (Ergintav et al., 2023; Kurt et al., 2023). The entire area of this research region is visible in Figure 1.1, which also includes some of the fault networks provided by (Styron & Pagani, 2020).

2.1.1. East Anatolia Fault Zone (EAFZ)

The EAFZ is a ≈600-km-long left-lateral strike-slip fault zone located between the Arabia - Eurasia - Anatolia Plate Boundary(Arpat & Saroglu, 1972). The fault zone starts from the northeast of the Karliova triple junction up to the Dead Sea Fault Zone in the southwest of the EAFZ (Balkaya et al., 2023). There are many debates concerning the termination of the EAFZ in the west; either it assimilates on the Levant Fault and continues southwards, or it terminates at the junction of the EAFZ and DSFZ (Güvercin et al., 2022). Duman and Emre (2013) divide the EAFZ area into two strands: the northern and the main strand. The main strand is further divided into seven segments. From east to west, the main strand is divided into the Karliova, Ilica, Palu, Pütürge, Erkenek, Pazarcık and Amanos segments. The EAFZ, along with the Bitlis-Zagros Fold and Thrust Belt and the Caucasus Fold, accommodates the relative motion between Eurasia and Arabia (Vavra et al., 2024). Recent seismic observations allow us to identify the stress regime in the eastern part of the EAFZ, where it showcases both maximum and minimum compressional stress alongside left-lateral strike-slip movements that define the movement of this fault (Kiratzi, 1993).

East Anatolia Fault Main strand

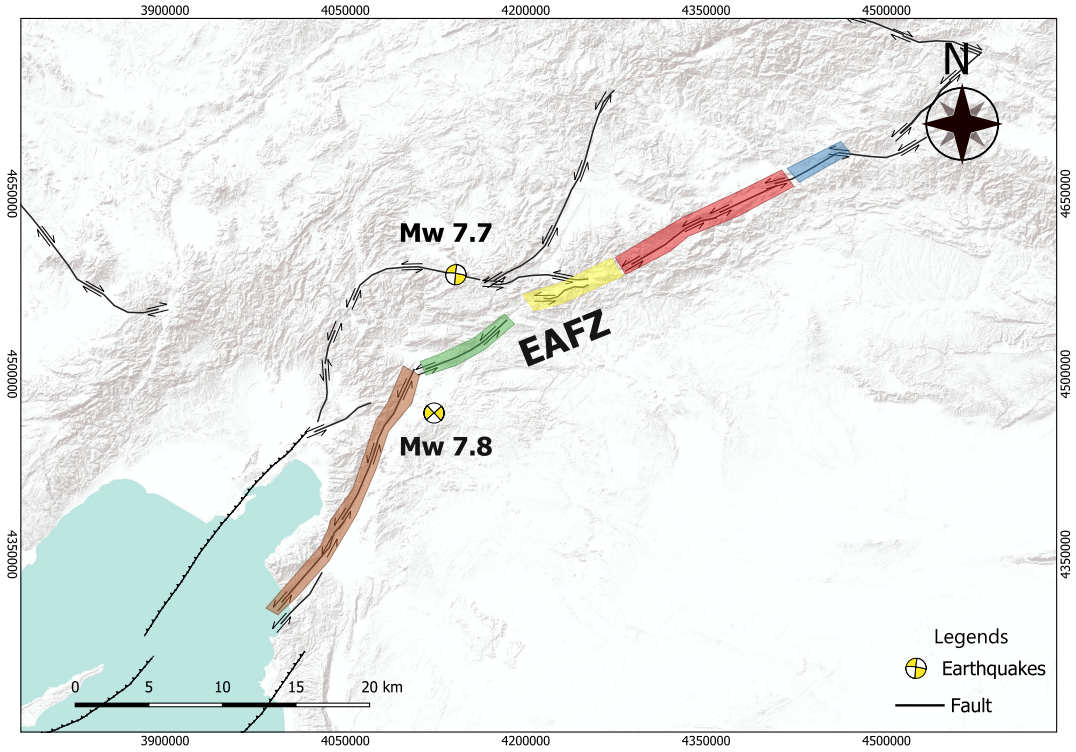

Figure 2.1: East Anatolia Fault Zone with segmentation shown by colored polygons: Amanos (brown), Pazarcik (green), Erkenek (yellow), Pütürge (red), and Palu (blue).

This region itself has been the subject of recurring seismic events in the area, such as the earthquake on the Amanos fault in the 19th century, with recorded $M_w 7.5$ and $M_w 7.2$ in 1822 and 1872, respectively (Ambraseys & Jackson, 1998). Earthquake in 1513 with $M_w 7.4$, 1114 $M_w 7.8$ earthquake in Pazarcık, and most recently the Elazığ earthquake near the Pütürge segments. (Pousse-Beltran et al., 2020). Previous research on slip deficit related to this study is available both immediately before and after the Kahramanmaraş earthquake doublet. Before the Kahramanmaraş earthquake doublet, geodetic and geological studies reported slip deficits of 9–10 mm/yr along the main strand of the EAFZ near Kahramanmaraş, decreasing to about 3 mm/yr towards the southern segments (Aktug et al., 2016; Koç & Kaymakcı, 2013; Reilinger et al., 2006). More recent work confirmed similar values of 9–10 mm/yr (Kurt et al., 2023; Vavra et al., 2024).

2.1.2. Çardak–Sürgü Fault

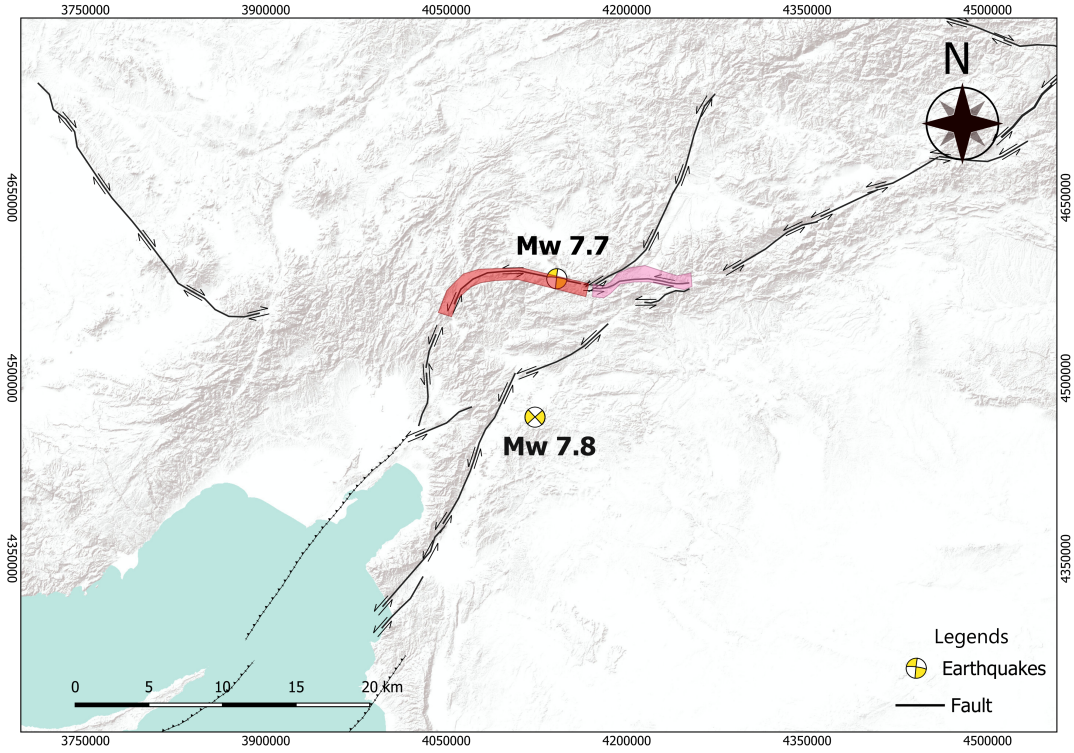

Figure 2.2: Çardak–Sürgü Fault with segmentation shown by colored polygons: Cardak(Red), Surgu(Pink)

The Çardak–Sürgü fault is approximately 160 km long and classified as the northern strand of the East Anatolian Fault Zone (EAFZ) (Duman & Emre, 2013). In comparison to the main strand of the East Anatolian Fault, the Çardak–Sürgü segment has a limited historical record of seismic activity. Çardak–Sürgü Fault has been relatively understudied, with historical sources indicating its last major ruptures occurred in 1544, while Balkaya et al. (2023) and Guidoboni et al. (1994) also reports an event in 584 along the Çardak segments. Besides the lack of sufficient seismic records, all earthquakes documented along the Çardak–Sürgü Fault fall below $M_w 6$(KOERI-RETMC, 2021) and are therefore considered minor. Consequently, research on this fault has remained limited, and its seismic potential and kinematics are still not well understood (Koç & Kaymakcı, 2013). The lack of previous studies and the absence of well-documented seismic events that could serve as benchmarks for identifying the Çardak–Sürgü Fault have led to ongoing debate regarding its kinematics. Koç and Kaymakcı (2013) suggest that the western segments of the Sürgü Fault are characterised by dextral strike-slip motion with a reverse component, whereas the eastern segment shows a normal component. In contrast, Duman and Emre (2013) describe the Sürgü Fault as predominantly left-lateral strike-slip. In the Kahramanmaraş earthquake doublet event, the derived moment tensor predominantly shows left-lateral strike-slip motion (Jia et al., 2023). After the Kahramanmaraş earthquake doublet, more research was put on the Çardak–Sürgü fault to understand the kinematics and underlying slip deficit that occur in this area during the interseismic period. Özbey et al. (2024) and Vavra et al. (2024) investigate the slip deficit in the main strand of EAFZ and Çardak–Sürgü Fault, they found that the slip deficit occurring in those areas is $2-5$ mm/yr for the western EAFZ (Amanos–Erkenek) and about $2-4$ mm/yr for the Çardak–Sürgü Fault. Balkaya et al. (2023) provided evidence that the Çardak–Sürgü Fault is capable of producing an earthquake of this magnitude, given its segment length and the fact that the last major event occurred in 584 (Balkaya et al., 2023; Duman & Emre, 2013), allowing strain to accumulate over more than a thousand years.

Sürgü Fault

The SürgüFault is an active sinistral-strike slip fault that extends for about 70 km. Balkaya et al. (2023) proceeds to explain that the Sürgü Fault is dipping in different directions, with the eastern segments dipping 85 degrees to the north, and the western segments dipping to the south. The 50 km long section of the fault starts in the south of Elikhan, passes through the village of Sürgü and ends in the village of Küçüklü, which runs in an east direction (Balkaya et al., 2023).

Çardak Fault

The Çardak fault is a ≈80 km long fault, located between Nurhak and Göksun. The fault runs through Göksun with a concave geometry (Balkaya et al., 2023). The Çardak fault is generally divided into two sections, one 35-km-long eastern section that has a strike orientation of N75°W and connects with the Nurhak fault, and another section located at the 50-km-long western part of the Çardak Fault that cuts the old thrusts and folds with a left-lateral fault morphology, This section includes the Go¨ksun bend, which trends N45°E at its western tip (Duman & Emre, 2013).

2.2. Earthquake Cycle

An earthquake, by definition and by its name, is a quake or tremor that occurs in the lithospheric part of the Earth. Earthquake magnitudes range from very small, when no one can feel them, to very large, which can generate tsunamis or destroy entire regions within seconds. The shaking during an earthquake results from accumulated strain that is suddenly released by rupture along the fault interface, releasing energy and generating seismic waves (Reid, 1910). This is why most earthquakes occur in areas where faults are present. Earthquakes follow a cycle, which refers to the phenomenon of repeated events on the same fault as a result of continual stress accumulation and periodic stress release in the same area (Scholz, 2002). In general, the earthquake cycle is divided into four stages: interseismic, coseismic, early post-seismic, and late post-seismic (Golriz et al., 2021).

The interseismic period is the long phase prior to an earthquake, marked by the gradual accumulation of strain over years to centuries. This build-up is driven by coupling across plate boundary segments, where the interface remains mechanically locked between earthquakes. During the coseismic stage, the locked section of the plate interface suddenly decouples, allowing slip to occur and initiating the elastic rebound that releases seismic waves. Observed horizontal and vertical surface displacements are well reproduced by elastic half-space models with fault slip consistent with seismological data (Govers et al., 2018). When the accumulated stress exceeds the rupture threshold, the fault breaks and both sides rebound toward their previous positions, releasing stored elastic strain. When the interseismic slip deficit is combined with the coseismic slip, their sum equals the long-term motion of the plate(Segall, 2013).

The early postseismic period begins immediately after rupture and is characterised by aseismic afterslip on surrounding or deeper fault patches (Marone et al., 1991; Perfettini & Avouac, 2004). Afterslip often persists for months to years and can explain rapid transient deformation observed geodetically (Freed, 2007). Additional processes, such as poroelastic rebound in the crust, may contribute to this phase. Afterslip may last from weeks to several years and contributes significantly to rapid post-earthquake deformation.

Finally, the late postseismic period is dominated by viscoelastic relaxation in the lower crust and upper mantle, redistributing stresses over decades to centuries (Hu & Wang, 2016; Pollitz et al., 2003). These processes gradually dissipate coseismic stress and restore the fault system toward interseismic conditions, completing the cycle.

2.3. Plate Boundaries

According to Palin and Santosh (2021), a plate is defined as a discrete mass of lithosphere, which may be entirely continental, entirely oceanic, or a combination of both. The zones of interaction between neighbouring plates are referred to as the plate boundaries according to Eagles (2020). Plate boundaries are further classified based on their kinematics and the effects they have on the surrounding area. Plate boundaries are classified as divergent, convergent, and conservative boundaries, with a subclassification depending on the component of the lithosphere (Dong et al., 2025).

Transform Settings

Continental transform faults are major strike-slip faults that cut through the continental lithosphere and connect continental plate boundaries. Transform faults are further classified based on the type of plate boundary they intersect. Dong et al. (2025) classifies the continental transform boundary further into rift-suture zone type, subduction-subduction zone type, and subduction-suture zone type. The region of interest of this research, the East Anatolia Fault, is a strike-slip fault that connects the Arabia and Anatolia Plates. The East Anatolia Fault is categorised as a subduction-suture zone type, as seen from the map, where in the southwest part of the fault, the EAFZ is connected to the triple junction between the Cyprus Arc and the Dead Sea Fault, where the subduction on the Cyprus Arc and rifting on the Dead Sea Fault Zone occurred. In the north eastern part of this fault, we can see that the EAFZ connects to Karliova Triple, where collision tectonics is observed (Emre et al., 2011; Şengör et al., 2014).

Although transform faults are primarily driven by strike-slip motion, which serves as their main kinematic mechanism, they can also be influenced by dip-slip components, as observed along the East Anatolia Fault. In such cases, the strike-slip motion remains dominant, but minor dip-slip components may arise due to local compression or extension across the fault. When both components act simultaneously, the resulting displacement is termed oblique slip, in which the fault exhibits a combination of strike-slip and dip-slip motion.

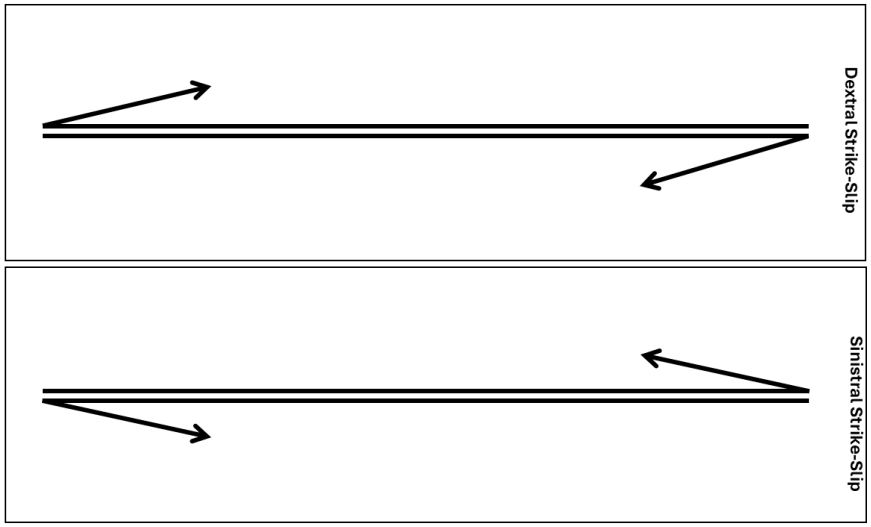

Figure 2.3: Strike-Slip Fault. Top Images show Dextral Strike-Slip and Bottom Images show Sinistral Strike-Slip

2.4. Slip Deficit

The phenomenon of interlocking at fault lines, which predominantly occurs at plate boundaries, causes motion near the fault to lag behind the far-field displacement of the plates and thus accumulate slip-deficit at a relative rate of the plate velocity (Herman et al., 2018). Figures below will show the illustration of the slip-deficit that happens between a transform plate boundary.

In the ideal case, both sides of the fault should move relative to each other at a uniform velocity (2.4a), regardless of the perpendicular distance to the fault, but due to the locking mechanism, the velocities of the plates near the fault when the interlocking happens slow down considerably (2.4b). The slip-deficit that accumulated for years would eventually be released during an earthquake, and that sudden release of accumulated slip during those years created the earthquake.

Researchers have been studying the slip deficit since the early 1960s. One of the simplest and oldest models is the 2D Screw Dislocation Model by Savage and Burford (1973). This model assumes fault as an infinitely long object from the surface to the centre of the Earth, assuming there is no friction between the atmosphere and the Earth's outer layer, and it lies in a half-space. This model remains widely used in research due to its simplicity and ability to estimate the slip deficit. Vavra et al. (2024) correlates the estimated accumulated slip deficit with the coseismic slip released during the earthquakes. By calcu-

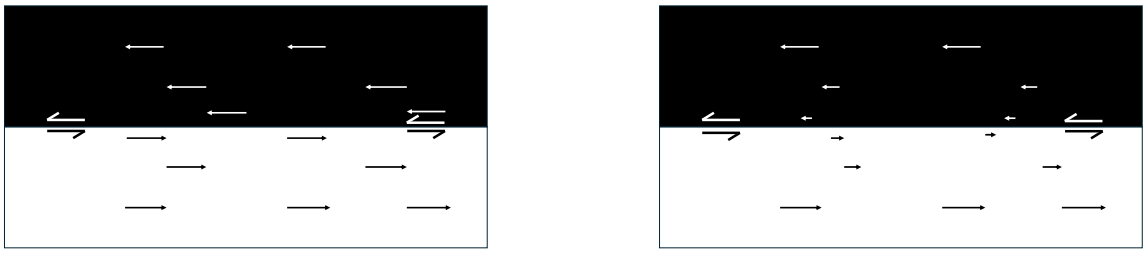

(a) Plate tectonics (idealised).

(b) Plate tectonics with an interlocking fault.

Figure 2.4: Comparison between (a) idealised plate tectonics and (b) plate tectonics with an interlocking fault in a strike-slip fault.

lating the slip deficit rate and the recurrence interval of seismic activity, it becomes possible to forecast the potential magnitude of future earthquakes. The estimation of slip deficit during the interseismic period would allow for the implementation of preventive measures to mitigate future hazards, reducing both potential losses and fatalities.

3

Data

This chapter outlines the datasets and methodological steps used to achieve the research objectives. It begins with a general description of the data sources, followed by a brief overview of the methodologies. The research methods are divided into three main parts: velocity transformation and projection to the fault, model set-up, and configuring the data assimilation process. Each step and method is then discussed in detail to provide a clear understanding of the overall research framework.

3.1. Data

The GNSS data used in this study are provided by Kurt et al. (2023). The dataset spans the period 1992–2020 and comprises 836 stations across the Anatolian Plate and its boundaries, with 78% campaign-type sites and 22% continuous stations. These observations were collected through the joint efforts of several projects and authorities, including the Turkish National Fundamental GPS Network (TNFGN), the CORS-TR network, TÜBİTAK's MAGNET network, the Turkish National Sea Level Monitoring System, and various municipal agencies (BUSKI, SASKI, ISKI). The raw phase data were processed using the GAMIT/GLOBK software package, daily solutions were aligned to ITRF2014, and the final velocities were expressed in a stable Eurasia reference frame after correcting for offsets, seasonal signals, and outliers.

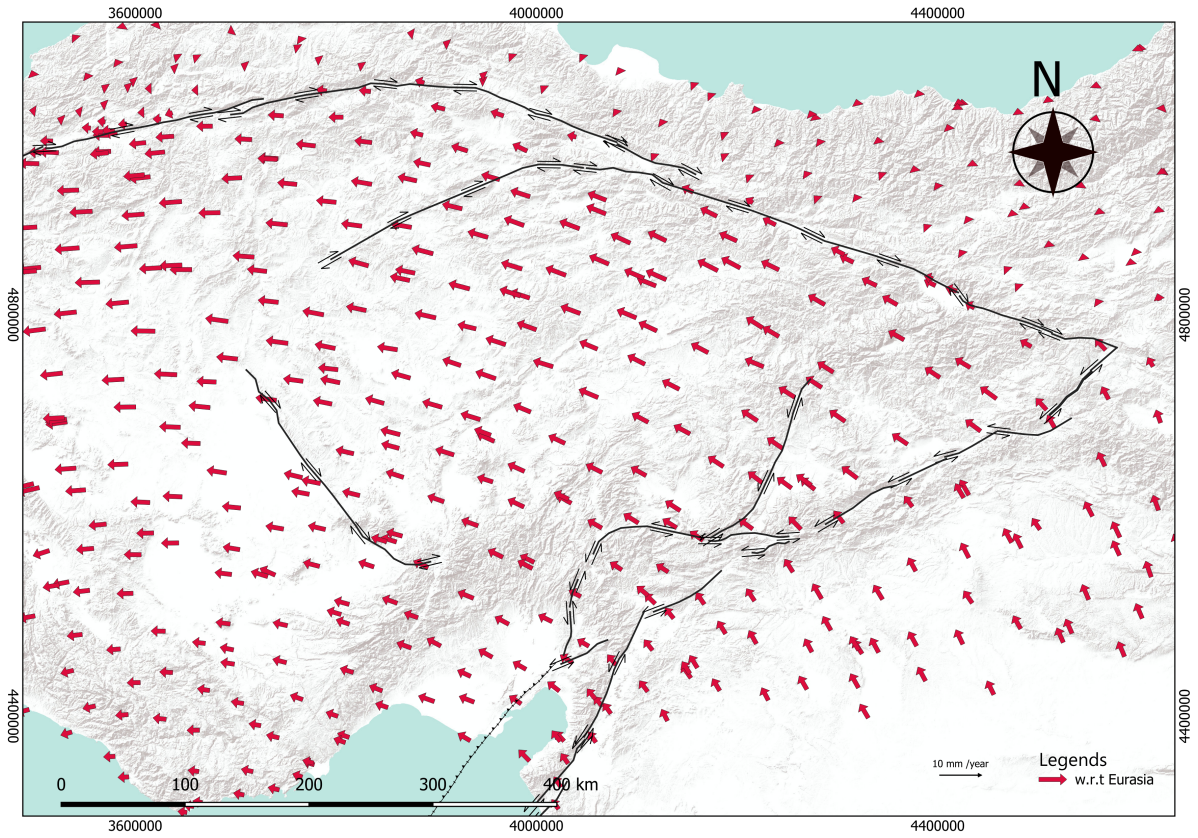

Figure 3.1: GPS Observations with velocity w.r.t Eurasian Plate (Kurt et al., 2023)

Table 3.1: Examples of GPS station coordinates and velocity components from (Kurt et al., 2023)

Station	Lat [°]	Lon [°]	V_E [mm/yr]	V_N [mm/yr]	σ_E	σ_N	ρ_{EN}
KBSK_GPS	35.36931	37.56012	-15.79	6.50	0.39	0.46	-0.092
BUNY_GPS	35.88127	38.87002	-17.31	7.18	0.26	0.26	-0.070
OGUZ_GPS	36.18838	38.65116	-16.48	7.82	0.22	0.24	-0.013
ADN1_GPS	35.34374	37.00418	-13.34	6.23	0.21	0.22	0.001

3.2. Velocity Transformation and Projection

This section will explain the information about the projection and transformation of velocity in detail

3.2.1. Velocity Frame Transformation

The dataset in this study came from previous studies by Kurt et al. (2023). This data is still showing the velocity relative to the Eurasia plate. This research will use the velocity relative to the Anatolia and Arabia plates since the EAFZ is located between these two plates. The transformation is done based on the Euler-Pole theorem. The Euler Pole of the Anatolia Plate with respect to Eurasia is provided by Kurt et al. (2023).

$$\mathbf{Pole} = \begin{bmatrix} \phi \\ \lambda \\ \Omega \end{bmatrix} = \begin{bmatrix} 26.880^\circ \\ 32.643^\circ \\ 0.84^\circ/\text{Myr} \end{bmatrix}$$

Using the obtained Euler Pole, the transformation of the velocity from the Eurasian reference to the Anatolia reference is performed using several steps as seen in Algorithm 1.

Algorithm 1 Velocity Frame Transformation

1: **Input:**
$\vec{v}_{\text{obs}}$: Observed ENU velocity (GPS)
Euler poles : $(\phi, \lambda, \dot{\theta})$ in degrees and deg/Myr
GPS station coordinates: latitude and longitude in degrees

2: **Output:**
$\vec{v}_{\text{rel}}$: GPS velocity relative to a reference frame

3: **Steps:**
4: Convert ϕ, λ from degrees to radians
5: Convert angular velocity $\dot{\theta}$ to radians per year:

$$\dot{\theta}_{\text{rad}} \leftarrow \dot{\theta} \cdot \frac{\pi}{180} \cdot \frac{1}{10^6}$$

6: Compute angular velocity vector $\vec{\omega}$:

$$\vec{\omega} = \begin{bmatrix} \dot{\theta}_{\text{rad}} \cdot \cos\phi \cdot \cos\lambda \\ \dot{\theta}_{\text{rad}} \cdot \cos\phi \cdot \sin\lambda \\ \dot{\theta}_{\text{rad}} \cdot \sin\phi \end{bmatrix}$$

7: Compute unit vector $\vec{r}$ from station coordinates:

$$\vec{r} = \begin{bmatrix} \cos\phi \cdot \cos\lambda \\ \cos\phi \cdot \sin\lambda \\ \sin\phi \end{bmatrix}$$

8: Compute plate velocity in XYZ:

$$\vec{v}_{xyz} = \vec{\omega} \times \vec{r}$$

9: Transform to ENU velocity using rotation matrix R_{enu}:

$$R_{\text{enu}} = \begin{bmatrix} -\sin\lambda & \cos\lambda & 0 \\ -\sin\phi\cos\lambda & -\sin\phi\sin\lambda & \cos\phi \\ \cos\phi\cos\lambda & \cos\phi\sin\lambda & \sin\phi \end{bmatrix}$$

$$\vec{v}_{enu} = R_{\text{enu}} \cdot \vec{v}_{xyz}$$

10: Convert units:

$$\vec{v}_{\text{plate}} = \vec{v}_{enu} \cdot 10^3 \quad \text{(m/yr to mm/yr)}$$

11: Compute plate rotation relative to Arabia:

$$\vec{\omega}_{\text{Eurasia w.r.t. Arabia}} = \vec{\omega}_{\text{Eurasia w.r.t. IGS}} - \vec{\omega}_{\text{Arabia w.r.t. IGS}}$$

$$\vec{v}_{\text{Eurasia w.r.t. Arabia}} = \vec{\omega}_{\text{Eurasia w.r.t. Arabia}} \times \vec{r}$$

12: Compute relative velocity:

$$\vec{v}_{\text{rel}} = \vec{v}_{\text{obs}} - \vec{v}_{\text{plate}}$$

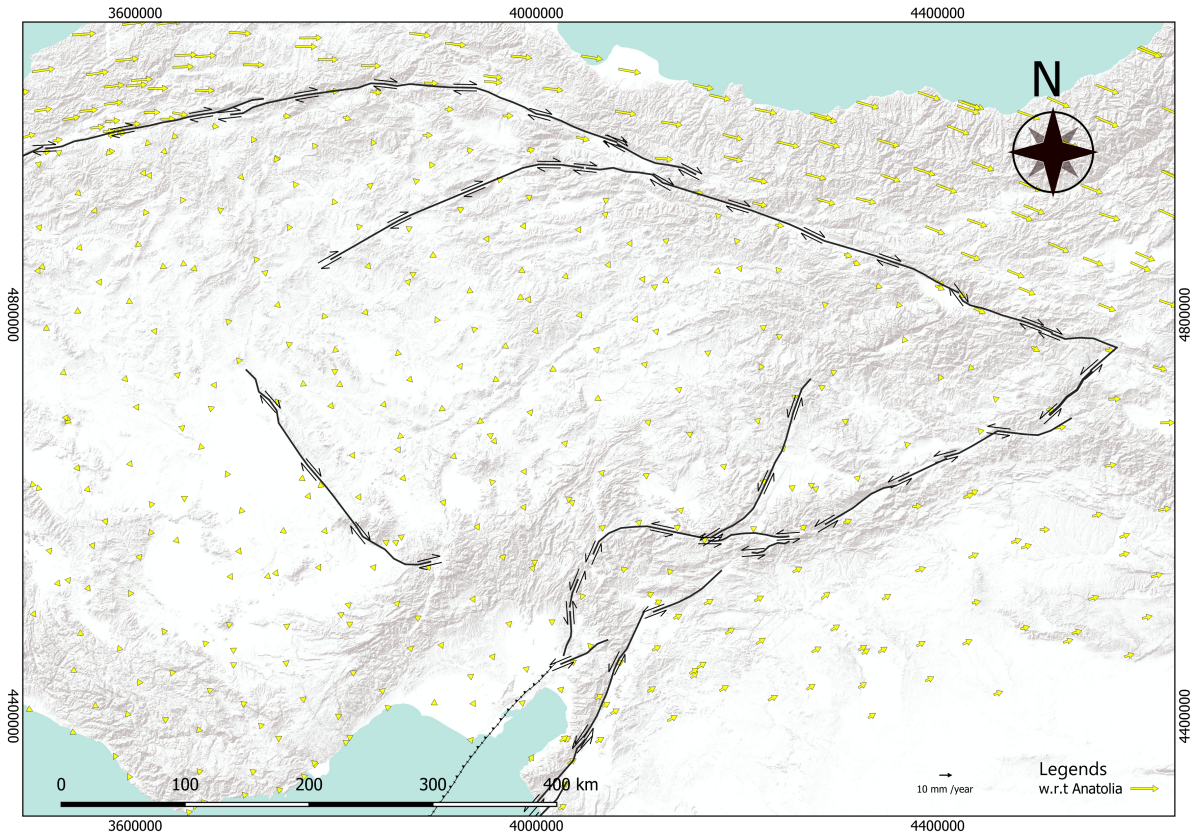

Figure 3.2: GPS Observations with velocity w.r.t Anatolia Plate

This figure shows the transformed velocity from the Eurasian reference plate with respect to the Anatolia plate. We can clearly see the distinction between the velocity with respect to the Anatolia plate and the Eurasian Plate. The GPS station located in the reference plate, in this case, the Anatolia plate, has smaller velocities in comparison with the GPS stations located in the Arabia or Eurasia plate. This phenomenon occurs because when using a specific plate as a reference, the GPS stations that are located on that plate are going toward zero. Similarly, velocities with respect to the Eurasian plate are smaller for stations located on the Eurasian plate. Using a similar procedure to obtain the velocity from the Eurasia to the Anatolia plate, we also transform the velocity relative to the Arabia plate.

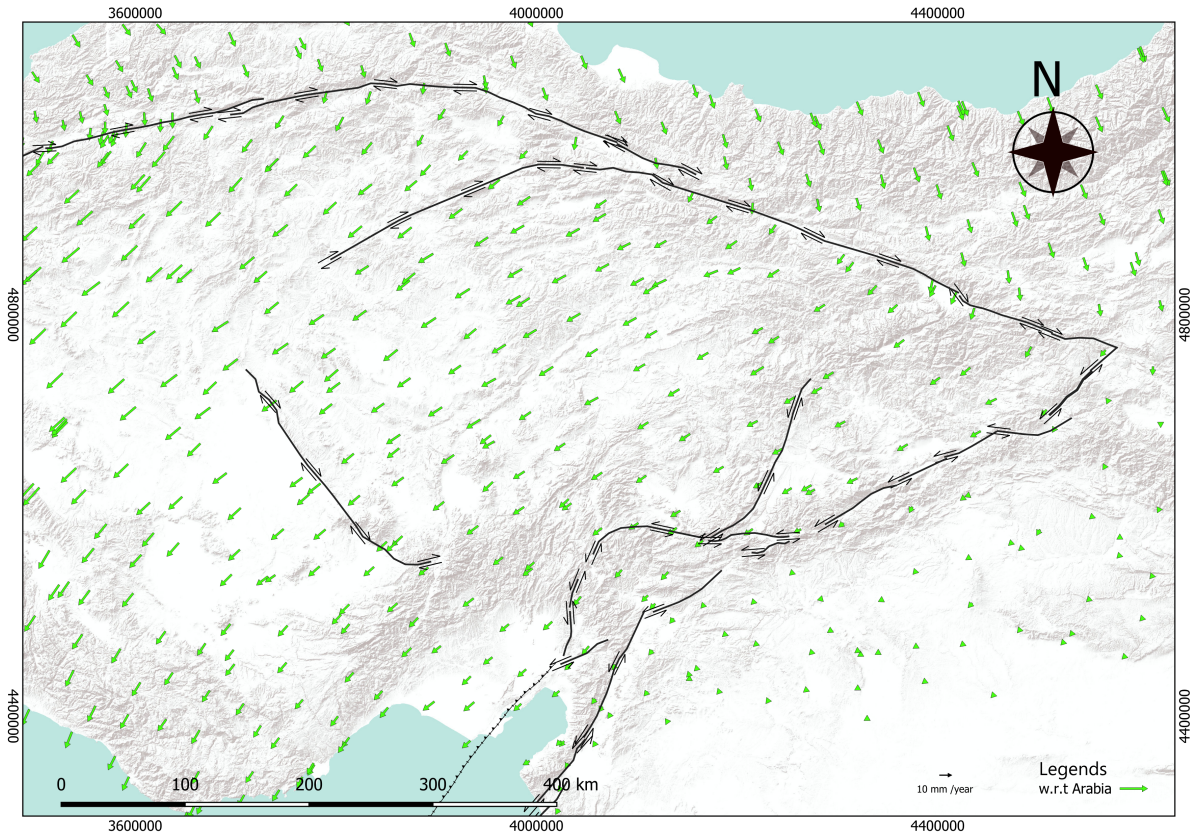

Figure 3.3: GPS Observations with velocity w.r.t Arabia Plate

This figure shows the transformed velocity from the Eurasian reference plate with respect to the Arabian plate.

4

Model

In this research, we employ the elastic 2D screw dislocation model proposed by Savage and Burford (1973) together with the 2D dip–slip formulation of Segall (2013). These models are used simultaneously to capture the combined deformation mechanisms, namely strike–slip and dip-slip along the main strand of the EAFZ and Çardak–Sürgü Fault. We assume an elastic half–space for the lithosphere (Savage & Burford, 1973; Segall, 2013), which demonstrated that over interseismic timescales, long-term displacement can be assumed to have an elastic behaviour. Previous research that uses this model can be seen in Savage and Prescott (1978) with some modification on its part in Hussain et al. (2018) and Shen et al. (2024) and Aktug et al. (2016).

4.1. Elastic Strike-Slip Model

The elastic strike-slip model assumes that the fault is locked from the surface down to a specified depth during the interseismic period, while uniform slip takes place below the locked zone (Savage & Burford, 1973). The Earth and underlying mantle are treated as an elastic half-space, and the fault is considered vertical and assumes there is no interaction between the crust and the atmosphere (Segall, 2013).

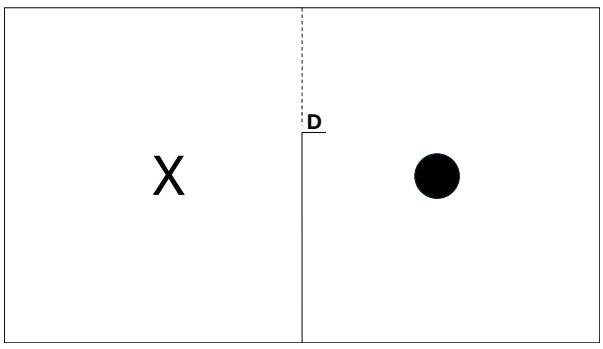

Figure 4.1: Illustration of a Screw Dislocation Model. The circle represents the side of the fault that goes out of the plane, and the cross represents the side of the fault that goes into the plane. The dashed line indicates the interlocking part of the fault, while the continuous line indicates the continuous slip beneath the locking depth.

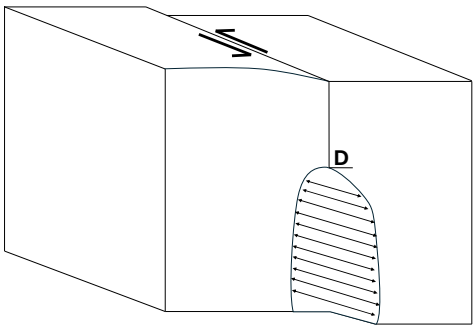

Figure 4.2: Illustration of an interseismic model of a locked fault. The fault is locked up until depth D, and beneath the locking depth, the fault moves uniformly. Images reproduced from (Savage & Burford, 1973)

Figures 4.1 and 4.2 illustrate the elastic strike-slip fault model, represented by a screw dislocation in a half-space. The images with circles illustrate the side of the plates going inwards from the image, and the cross illustrates the side of the plates going outwards from the image. The dashed line represents the locking depth of the fault, the part where the fault does not slip up until a point D. Beneath the locking depth D, the fault is assumed to be uniformly slipping as seen in Figure 4.2.

$$v_{\text{par}}(y) = \frac{V_s}{\pi} \arctan\left(\frac{x}{D}\right) \tag{4.1}$$

In Equation 4.1 and other equations that follow, the slip deficit is denoted as V_s, the locking depth as D and x as the distance perpendicular to the fault. Another variation of the elastic dislocation model introduces a modified model with an offset α. The offset is meant to accommodate the influence of other driving forces that the equation does not take into account. As a result, the surface expression of slip deficit is:

$$v_{\text{par}}(y) = \frac{V_s}{\pi} \arctan\left(\frac{x}{D}\right) + \alpha \tag{4.2}$$

Outlook on the Elastic Strike-Slip Model

This section provides a more detailed examination of how each parameter in the elastic strike-slip model used in this study influences the results. Several graphs are presented to illustrate these effects and to provide clear examples of the model's behaviour.

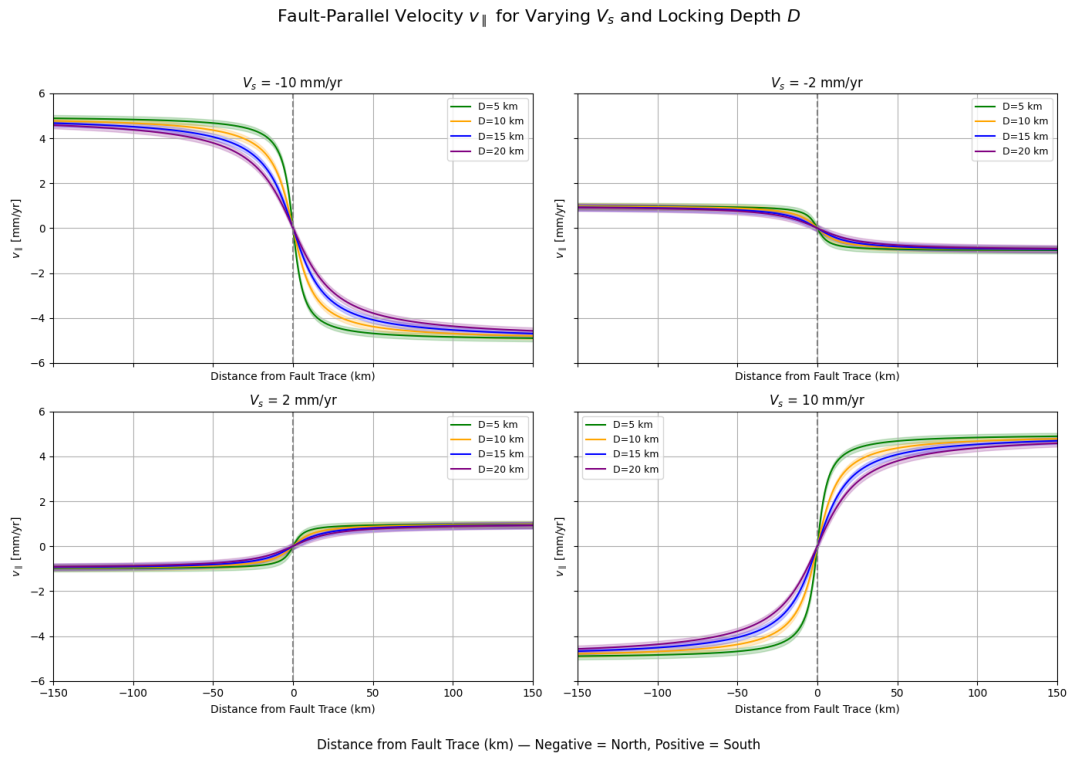

Figure 4.3: Image is reproduced based on the Strike-Slip Model by Savage and Burford (1973)

Figure 4.3 shows how the model works in a varied strike-slip rate and locking depth. From the graph, we can observe that indeed the velocities from each side of the fault are different. As seen in the figures, the graph shows that when the slip deficit (V_s) is small, the difference between the velocities at each side of the fault is also small, indicated by the small discourse at the fault ($X = 0$). $Vs = 10$ shows a larger disparity in the fault compared to $Vs = 5$. This graph also demonstrates that the fault-parallel velocity asymptotically approaches half of the slip rate at locations far from the fault trace (e.g., $x = 150$), as mentioned in (Hussain et al., 2018). In our case, the negative slip rates indicate a right-lateral strike slip, and the positive slip rate indicates left-lateral strike slip.

The next variable that will be discussed is the locking depth. A shallow locking depth would show a more abrupt/steeper shift in velocity near the fault, while a deeper locking depth shows the other way round. As the D goes to ∞, the arctan function term approaches a straight line, producing a nearly linear velocity profile. This indicates that the surface deformation is distributed very broadly across the crust, or the fault behaves as if it were fully creeping. This implies that a larger locking depth spreads the velocity gradient over a wider region, whereas a small locking depth localises all deformation at the fault trace.

Ideally, the model should demonstrate zero parallel velocity at the fault (4.3, with a differing velocity direction across the fault, similar to what is shown in Figure 2.4. However, due to various forces that affect plate movement, it is common to find locations where the model does not show zero velocity at the fault and where the velocities are moving in the same direction. The bias term α (or offset) is introduced to account for additional forces or background block motions. In many applications, the offset is taken as $Vs/2$, which corresponds to the far-field velocity on either side of the fault, having α to $Vs/2$ will result in having 0 parallel velocity at one side of the fault. But in some cases it‘s found that the offsets are more than $Vs/2$ because there‘s another driving forces that possibly drive the plate motion.

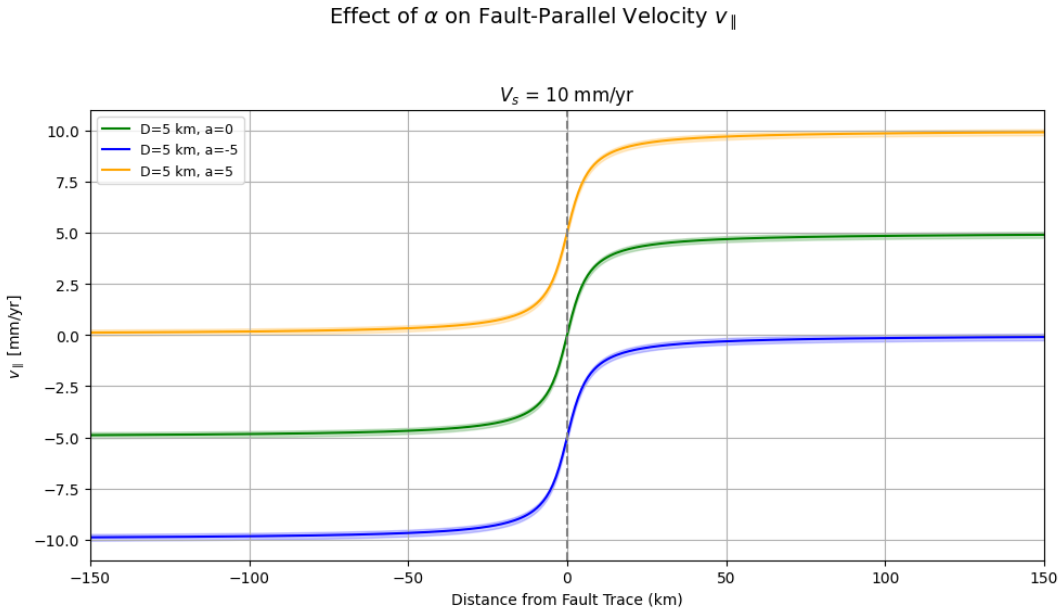

Figure 4.4: Strike slip model with various α

4.2. Elastic Dip-Slip Model

The original model was designed specifically for strike-slip fault settings, as it was initially developed to estimate the slip deficit on a strike-slip fault (Savage & Burford, 1973). The East Anatolian Fault Zone (EAFZ) primarily exhibits left-lateral strike-slip motion. However, the main strand of EAFZ and the Çardak-Sürgü Fault also show evidence of reverse and normal faulting (Balkaya et al., 2023; Duman & Emre, 2013; Güvercin et al., 2022). It has also been noted that even a strike-slip fault would have extension and shortening at some point (Dong et al., 2025), which means the force that acts on the fault is not purely strike-slip motion; thus, to achieve a more accurate estimation of slip behaviour, it is essential to account for dip–slip motion as well. In this research, I incorporate dip–slip deformation following the approach proposed by Segall (2013). Similar to the strike–slip model, the dip–slip formulation assumes that the fault is locked to a depth D, while uniform slip occurs below the locking depth, with the lithosphere approximated as an elastic half-space.

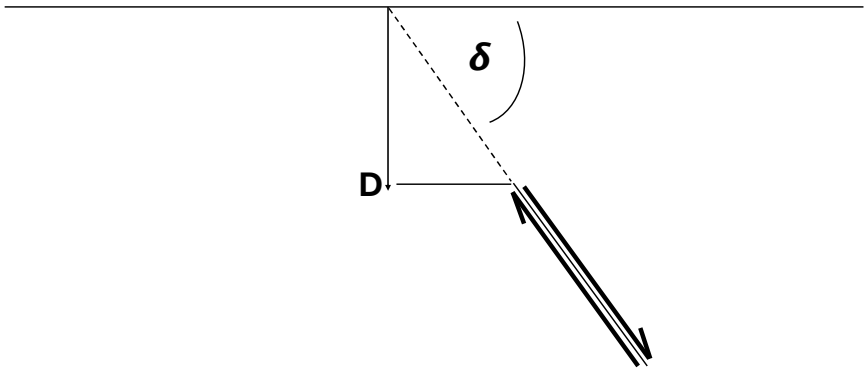

Figure 4.5: Illustration of a Dip-Slip Model

$$v_{\text{per}}(x) = \frac{V_d}{\pi}[\cos\delta \arctan\left(\frac{x}{D}\right) + \frac{\sin\delta - \frac{x}{D}\cos\delta}{1 + \left(\frac{x}{D}\right)^2}] + \beta \tag{4.3}$$

Here, V_d denotes the dip-slip rate, δ the dip angle, while x and D represent the perpendicular distance to the fault and the locking depth, respectively. The parameter β, similar to α in Equation 4.1, is an offset term introduced to account for additional forces and background motions. Similar to $Vs/2$ that was the far-field effect of parallel velocity, the corresponding far-field effect of dip-slip is given by $\frac{V_d}{2}\cos\delta$. In this study, the analysis is restricted to the horizontal component of the dip-slip model, while the model in Segall (2013) also took into account the vertical component.

Outlook on the Elastic Dip-Slip Model

In this research, we will limit our analysis to the horizontal components of the model. The original formulation by Segall (2013) introduces d_{offset} to represent the possibility that the interlocking mechanism in the subsurface is not perfectly aligned with the surface fault trace. In this study, however, we assume $d_{offset} = 0$. The following graph illustrates how each parameter, namely V_d, δ, and D, affects the outcome of the model.

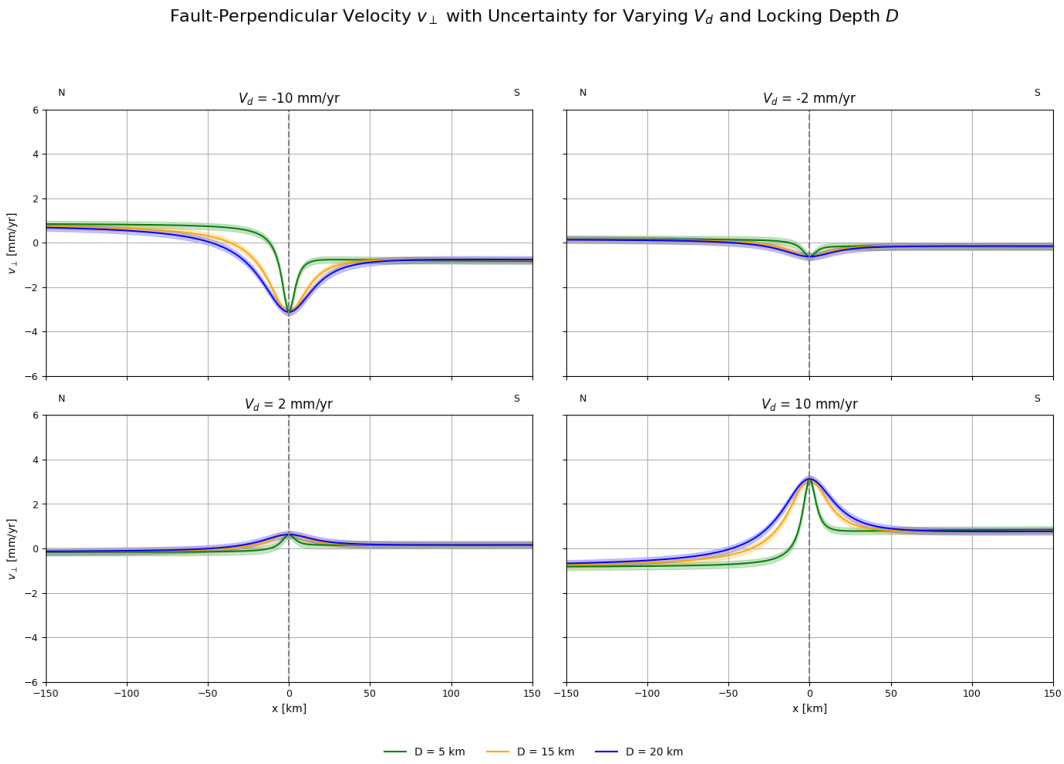

Figure 4.6: Dip-Slip Model Outlook with Dip Angle 80° (Segall, 2013)

From Segall (2013), a positive dip-slip value indicates that both sides of the fault move away from the fault plane, representing an extensional regime, whereas a negative dip-slip value indicates that both sides of the fault move towards the fault plane, corresponding to a compressional regime. As the dip angle in this research is constrained to only be around $0 < x < \pi/2$. A larger dip-slip deficit increases the difference in perpendicular velocities on either side of the fault, while the locking depth has a similar effect in the dip-slip model as in the strike-slip model: a larger locking depth causes the crustal movement to be distributed over a wider region, whereas a smaller locking depth localises the deformation closer to the fault.

From these figures, we can compare how the dip angle influences the behaviour of the model. As the dip angle approaches $\frac{\pi}{2}$, the asymmetry of perpendicular velocity diminishes, and the perpendicular velocities on both sides of the fault become nearly identical. The bias term is introduced to account for background motion or external influences, allowing the model to remain flexible and better approximate observed perpendicular velocities. This effect can be generalised by considering the far–field term on each side of the fault, $\frac{V_d}{2}\cos\delta$, which results in zero perpendicular velocity on one side of the fault, similar to the addition of the α term as $V_s/2$ in the strike–slip case, and also similar to the strike slip sometimes the far-field effect is not able to constraint the velocity of other fault to be zero, meaning there‘s additional forces besides the far-field effect that drive the plate movement.

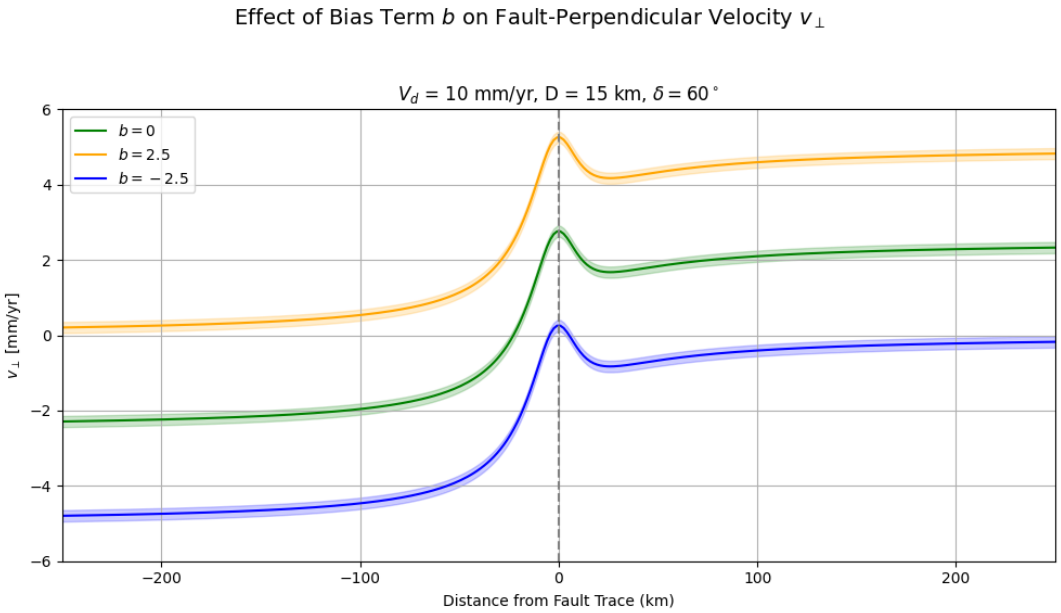

Figure 4.7: Dip-Slip Model with different β (Segall, 2013)

Here, Figure 4.7 shows that if β goes to $\frac{V_d}{2}\cos\delta$, one of the sides of the fault will have 0 perpendicular velocity.

4.3. Model Set-Up

In this research, there are 2 model setups that will be tested. The first model will consist of Eq. 4.1 with Eq.4.3 using the Anatolia Observations, and another using data with respect to the Arabian plates.

4.3.1. Model 1: Strike−slip & Dip-Slip in Respect to Anatolia

$$v_{par}(x) = \frac{V_s}{\pi}\arctan\left(\frac{x}{D}\right) + \alpha \tag{4.4}$$

$$v_{\text{per}}(x) = \frac{V_d}{\pi}[\cos\delta\arctan\left(\frac{x}{D}\right) + \frac{\sin\delta - \frac{x}{D}\cos\delta}{1+\left(\frac{x}{D}\right)^2}] + \beta \tag{4.5}$$

4.3.2. Model 2: Strike−slip & Dip-Slip in Respect to Arabia

$$v_{par}(x) = \frac{V_s}{\pi}\arctan\left(\frac{x}{D}\right) - \alpha \tag{4.6}$$

$$v_{\text{per}}(x) = \frac{V_d}{\pi}[\cos\delta\arctan\left(\frac{x}{D}\right) + \frac{\sin\delta - \frac{x}{D}\cos\delta}{1+\left(\frac{x}{D}\right)^2}] - \beta \tag{4.7}$$

5

Methodologies

5.1. Methodology

This section will explain the sequential steps taken in this research from the dataset up until the inversion result from the data assimilation

The first step of this research is to apply the conformal mapping. Conformal Mapping embedded in the Analytic Element Method (AEM) Toolbox on the fault and the GPS station. This is done since the output of the elastic dislocation model shown in Equation 4.1 is defined in terms of velocities parallel and perpendicular to the fault, which is why it is essential to project the observed GPS velocities accordingly. The AEM Toolbox facilitates this by first transforming both the fault geometry and GPS station coordinates into a complex space. Once the parallel and perpendicular components are obtained in this transformed space, the results are converted back into the original coordinate system. This projection step is performed for both the East Anatolian Fault Zone (EAFZ) and the Çardak–Sürgü Fault, where the geometry of both faults is defined in Figure 2.1, ensuring that the GPS velocity components are properly aligned with the domain of the model output.

The elastic model in this research is implemented across a series of cross-sections oriented perpendicular to the fault. These cross-sections are introduced in detail in subsection 5.2.4, where the corresponding figures are presented. They are initially defined in the complex space using the AEM Toolbox, which facilitates fault-aligned transformations, as explained in subsection 5.2.1. Once defined, the cross-sections are converted back into the original geographic coordinate system and serve as spatial representations of the model domain. Because the model outputs are generated along these cross-sections, a mathematical interpolation is required to relate the results to the actual GPS observation points. In this study, a linear weighting scheme is adopted to project the modelled velocity components from the nearest cross-section to the location of each observation point, as outlined in section 5.3. This approach ensures that the forecasted results can be directly compared with the observed surface velocities for further analysis.

Since this research applies data assimilation to both faults, it is necessary to convert the previously obtained parallel and perpendicular velocity components back into the East-North-Up (ENU) reference frame. This step ensures consistency, as each fault has a different geometry, resulting in different orientations for the projected velocity components. Reprojecting into the common ENU frame allows for coherent assimilation. The data assimilation employed in this research is the Ensemble Kalman Smoother (EnKS), which serves as the primary inversion method. The EnKS is chosen because the forward model is time-invariant. This makes the observations to be assimilated simultaneously to estimate the posterior state and parameters. The whole flow chart of this research is shown in Figure 5.1.

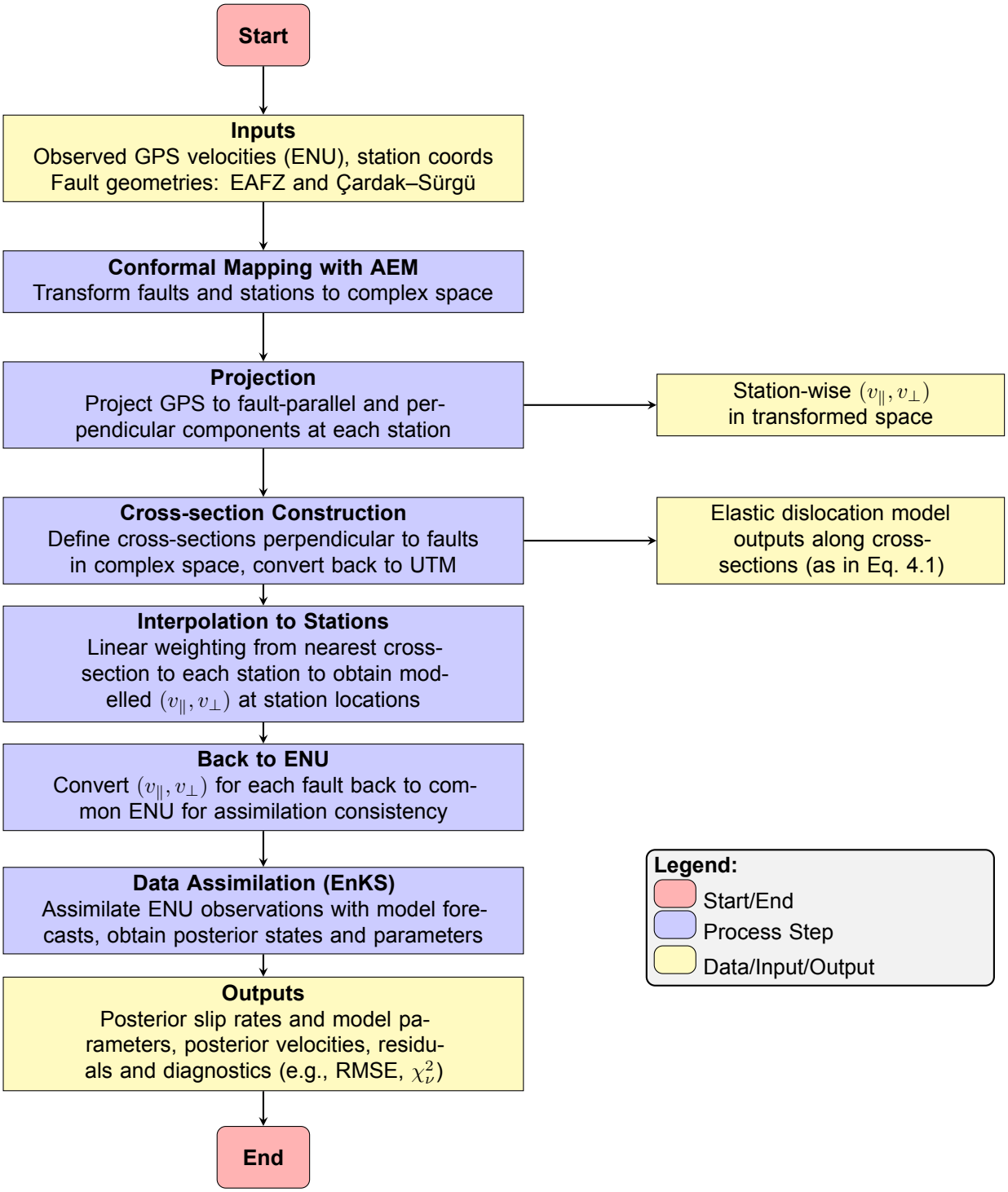

Figure 5.1: Workflow for fault-aligned projection using AEM, cross-section based modelling, interpolation to GPS stations, re-projection to ENU, and Ensemble Kalman Smoother assimilation.

5.2. Analytic Element Method

The Analytic Element Method (AEM) used in this study follows the open-source AEM Toolbox of Ramgraber (2019). In AEM, the two-dimensional steady-state flow field is represented by a complex potential,

$$\Omega = \Phi + i\Psi,$$

Where Φ is the head (hydraulic) potential and Ψ is the stream function, evaluated at complex coordinates $z = x+iy$. The global solution is built by linear superposition of analytic elements $f_e(z;\theta_e)$ (Strack, 2003). A key feature of the toolbox is the use of conformal mapping, an angle-preserving transformation in the complex plane. This is implemented through Möbius transformations (optionally combined with a Schwarz–Christoffel map) (Ramgraber, 2019). In practice, we employ this mapping to generate a flexible regional background flow, onto which local elements are superimposed. Because the transformation is conformal, lines constructed to be fault-parallel and fault-perpendicular in the complex plane remain consistent along the fault, ensuring that the model retains its intended orientation with respect to each fault in the mapped domain. Finally, the resulting fields are transformed from the complex z–plane to Universal Transverse Mercator (UTM) coordinates, so that values can be interpreted in real (canonical) space.

The analytic elements in this toolbox are divided into two categories: *Relative elements* (e.g., rate-specified wells, line sinks, area sinks/sources). Relative elements impose a change *relative* to the background. *Absolute elements* (e.g., prescribed-head segments, no-flow boundaries, polygonal inhomogeneities). Absolute elements enforce an *absolute* condition (Ramgraber, 2019; Strack, 2003). Faults are modelled as no-flow boundaries in this research, which enforce zero normal flux and make streamlines run parallel to the fault while equipotentials cross it perpendicularly. The projection of streamlines and equipotentials that cross perpendicular and parallel to the fault serves as the parallel and perpendicular projection for our research.

5.2.1. Projection using AEM Toolbox

The first step in this research involved transforming the fault and GPS data, originally defined in the original or canonical space, as we say, into a complex-valued space using the aforementioned Analytic Element Model Toolbox (Ramgraber, 2019). The transformation from the canonical to a complex space is pretty straightforward, as could be seen in Algorithm 2.

Algorithm 2 Converting LineString to Complex Array

Input:
  G: LineString geometry with coordinates (x_i, y_i)
Output:
  Z: Array of complex numbers $z_i = x_i + iy_i$

Initialise an empty list: $Z \leftarrow [\,]$
for each coordinate pair (x, y) in G **do**
  Compute $z \leftarrow x + iy$
  Append z to Z
end for
Convert list to Array: $Z \leftarrow \texttt{array}(Z)$
return Z

The head of discharge flow represents the perpendicular projection onto the fault, which is expressed as the real component of the z value in the complex space. The stream function represents the parallel projection of the fault and is expressed as the imaginary value of z. The AEM Toolbox also provides a built-in function that allows for retracting the gradient at every point. The gradient function will return the gradient of the imaginary and real components of each element, in this case, the GPS stations. By employing an arctangent function that considers the imaginary component over the real component of the gradient, we can determine the angle of the parallel and perpendicular projections relative to the East-North-Up (ENU) velocity frame.

$$\phi_i \leftarrow \arctan 2(\Im(\Delta z), \Re(\Delta z))$$

This approach enables us to measure the angle clockwise from East for each GPS station. Subsequently, this angle facilitates the transformation of the velocities from the standard ENU frame into components that are aligned with both the parallel and perpendicular orientations concerning the fault geometry.

5.2.2. Projection of the Fault

Projection in Complex Space

In this research, the East Anatolian Fault Zone (EAFZ) is projected into complex space starting from the Amanos region and extending to the Palu segment. The Illica and Karliova segments are not included in this projection, as the GPS data in those areas is significantly influenced by the neighbouring North Anatolian Fault Zone (NAFZ). On the other hand, the projection for the Çardak–Sürgü segments begins from the Sürgü area, continues along the Çardak Fault, and extends further to Yumurtalık and Toprakkale, similar to the research done by (Özbey et al., 2024). This is simply the kinematics of the Çardak–Sürgü that continues up until this point.

The projection of the velocities, both perpendicular and parallel, is performed in complex space using the AEM Toolbox, as explained in the previous sections. Once the projections in complex space are obtained, they are converted back to the canonical or original space. The calculated angle for each GPS station is then applied to the rotation matrix T, which is introduced in the following sections. In this way, the velocity components parallel and perpendicular to each fault are derived.

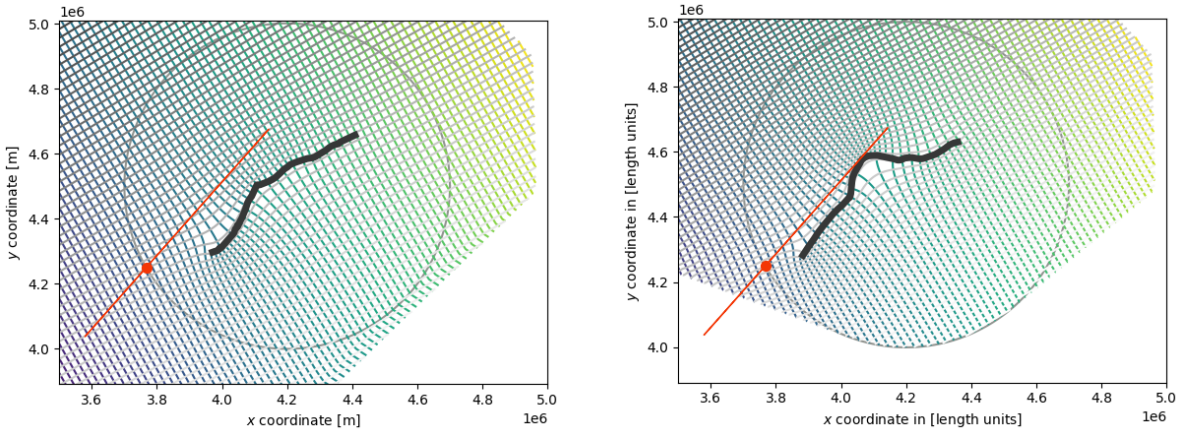

(a) Projection of the Main Strand of the EAFZ in AEM Toolbox

(b) Projection of the Çardak-Sürgü Fault in AEM Toolbox

Figure 5.2: Projection of Both Faults in AEM Toolbox.

As these projections are still in complex spaces, the first thing that we need to do to proceed with further processing is to bring these projections into the real space, in this case, the UTM.

Projection of the fault and perpendicular in UTM

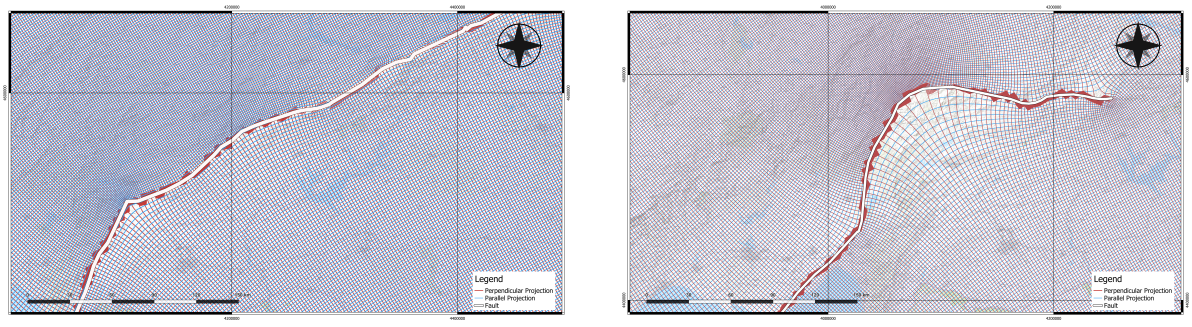

(a) Projection of the Main Strand of the EAFZ in AEM Toolbox

(b) Projection of the Çardak-Sürgü Fault in AEM Toolbox

Figure 5.3: Projection of the main strand of the EAFZ and the Çardak-Sürgü Fault shown side by side in UTM projection.

Figures 5.3 illustrate the parallel and perpendicular projections created in a transfer into a UTM projection. The imaginary and real values of z represent the parallel and perpendicular projections, respectively.

5.2.3. Transformation of Velocities to Parallel and Perpendicular Frame

The defined matrix T transforms the velocity from the standard ENU frame to the perpendicular and parallel projections to each corresponding fault. And the inverse of the T matrix serves to rotate the perpendicular and parallel velocity from the model back to the ENU reference frame.

$$T = \begin{bmatrix} \cos\theta & \sin\theta \\ -\sin\theta & \cos\theta \end{bmatrix}, \qquad T^{-1} = \begin{bmatrix} \cos\theta & -\sin\theta \\ \sin\theta & \cos\theta \end{bmatrix}$$

The procedure to transform velocities from the ENU reference frame to the parallel–perpendicular fault system, and vice-versa, is shown in Algorithm 3.

Algorithm 3 Project ENU Velocities to Fault-Aligned Frame (Parallel/Perpendicular) and Propagate Uncertainty

1: **Input:**
v_E, v_N: East and North velocity components
σ_E, σ_N: Standard deviations
ρ_{EN}: East-North correlation
θ: Rotation angle (radians)
`prefix`: Optional prefix for output columns

2: **Output:**
$v_\perp$, $v_\parallel$: Rotated velocity components
$\sigma_\perp$, $\sigma_\parallel$: Rotated standard deviations
$\rho_{\perp\parallel}$: Correlation in rotated frame

3: **Steps:**
4: : Define original covariance matrix:

$$\Sigma = \begin{bmatrix} \sigma_E^2 & \rho_{EN} \cdot \sigma_E \cdot \sigma_N \\ \rho_{EN} \cdot \sigma_E \cdot \sigma_N & \sigma_N^2 \end{bmatrix}$$

5: Define rotation matrix:

$$T = \begin{bmatrix} \cos(\theta) & -\sin(\theta) \\ \sin(\theta) & \cos(\theta) \end{bmatrix}$$

6: Rotate velocity vector:

$$\begin{bmatrix} v_\perp \\ v_\parallel \end{bmatrix} = R \cdot \begin{bmatrix} v_E \\ v_N \end{bmatrix}$$

7: Compute rotated covariance matrix:

$$\Sigma_{\text{rotated}} = T \cdot \Sigma \cdot T^\top$$

8: Extract from Σ_{rotated}:

$$\Sigma_{\text{rotated}} = \begin{bmatrix} \sigma_\perp^2 & \text{cov}_{\perp\parallel} \\ \text{cov}_{\perp\parallel} & \sigma_\parallel^2 \end{bmatrix}$$

9: Compute rotated standard deviations and correlation:

$$\sigma_\perp = \sqrt{\sigma_\perp^2}, \quad \sigma_\parallel = \sqrt{\sigma_\parallel^2}$$

$$\rho_{\perp\parallel} = \frac{\text{cov}_{\perp\parallel}}{\sigma_\perp \cdot \sigma_\parallel}$$

10: Results:
θ (radians and degrees)
$v_\perp$, $v_\parallel$
$\sigma_\perp$, $\sigma_\parallel$, $\rho_{\perp\parallel}$

Observed velocity vectors transformed from Easting–Northing components into parallel and perpendicular components with respect to the fault, using the projection angle from and the transformation algorithm are shown below.

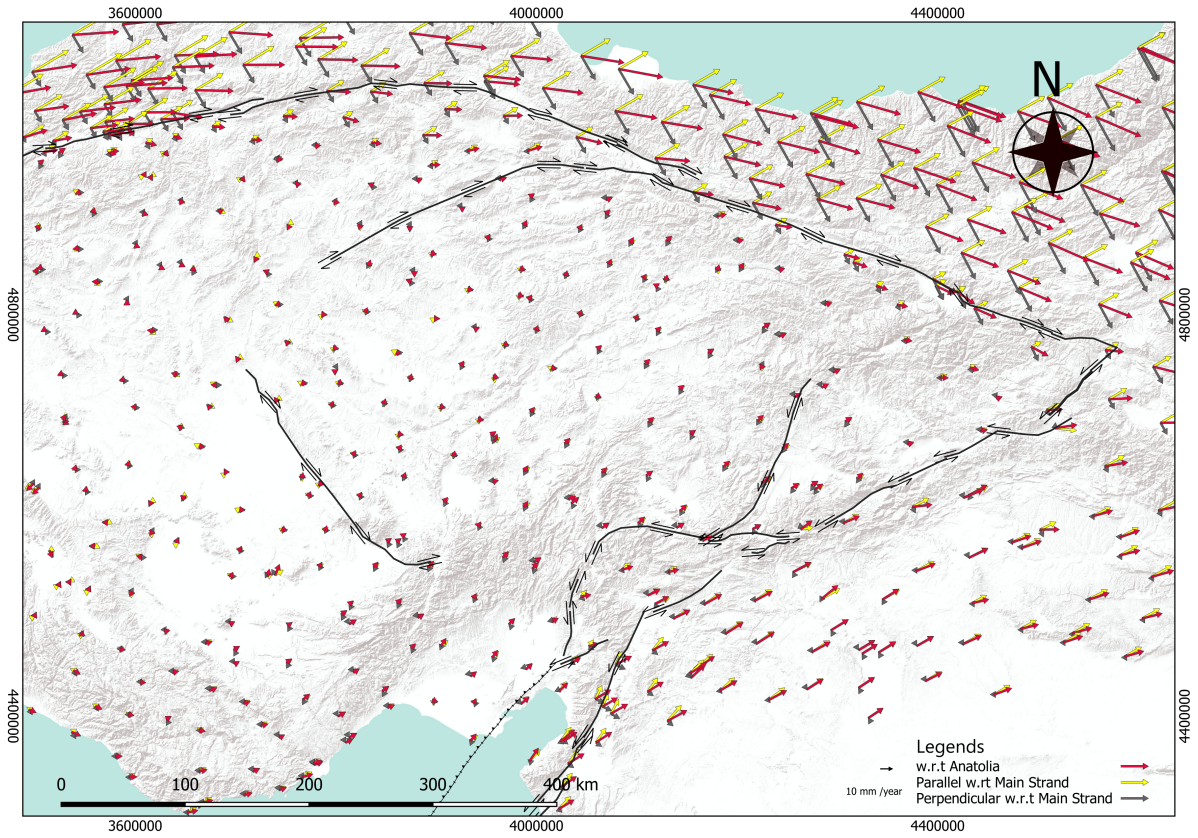

(a) Anatolia relative to Main Strand EAFZ

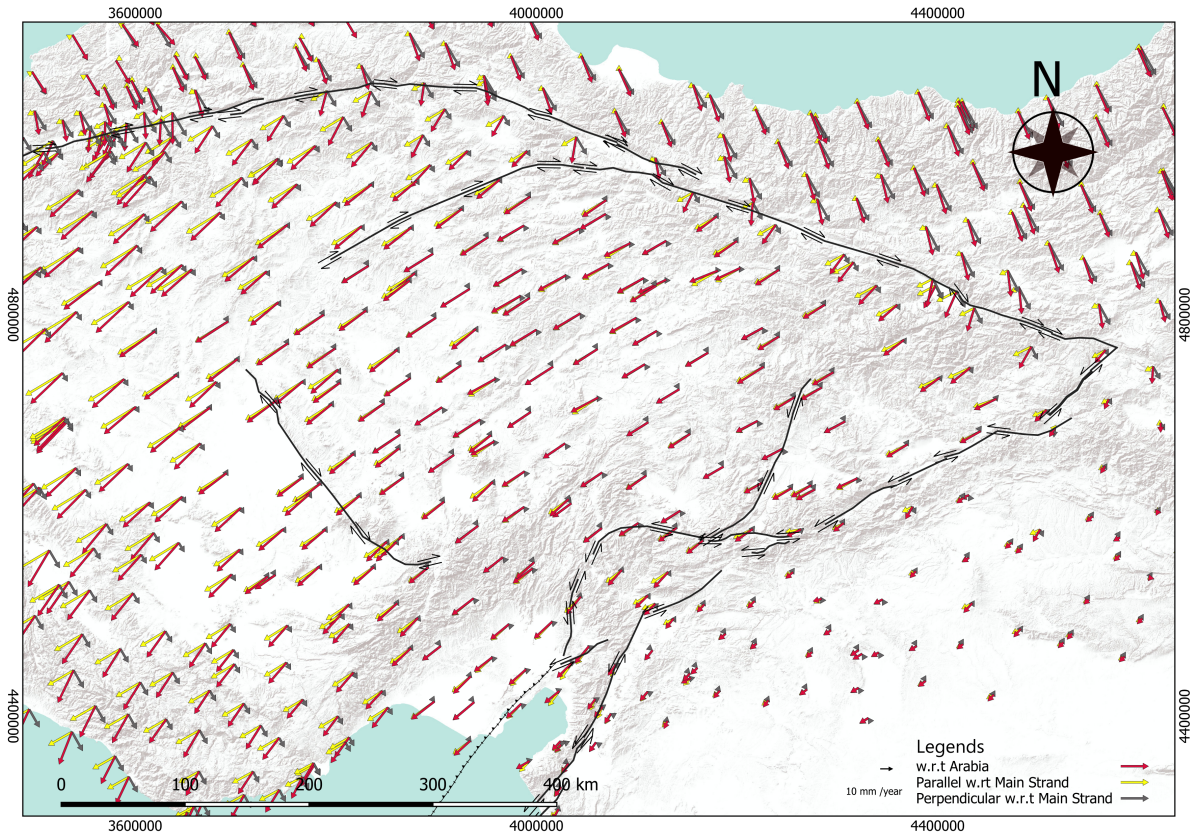

(b) Arabia relative to Main Strand EAFZ

Figure 5.4: Parallel and perpendicular velocity components relative to Anatolia and Arabia reference frames for the Main Strand of the East Anatolian Fault Zone (EAFZ).

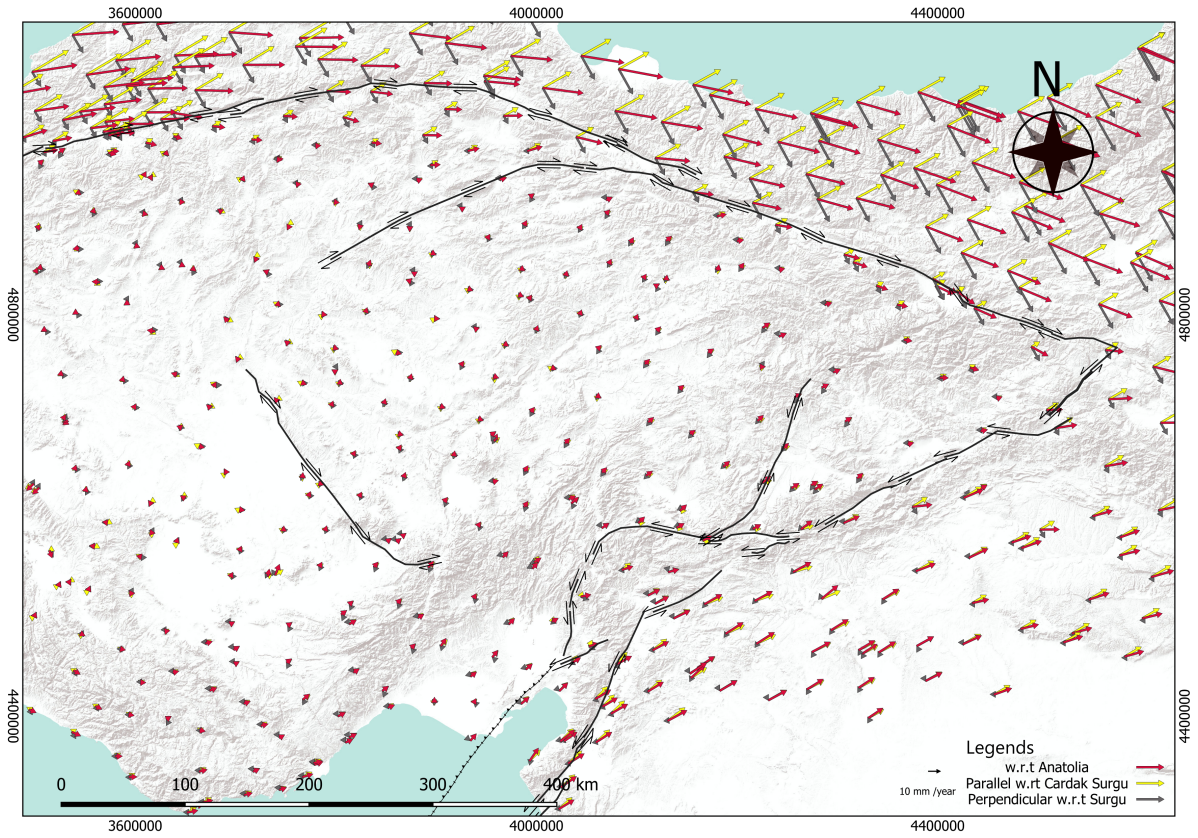

(a) Anatolia relative to Çardak–Sürgü Fault

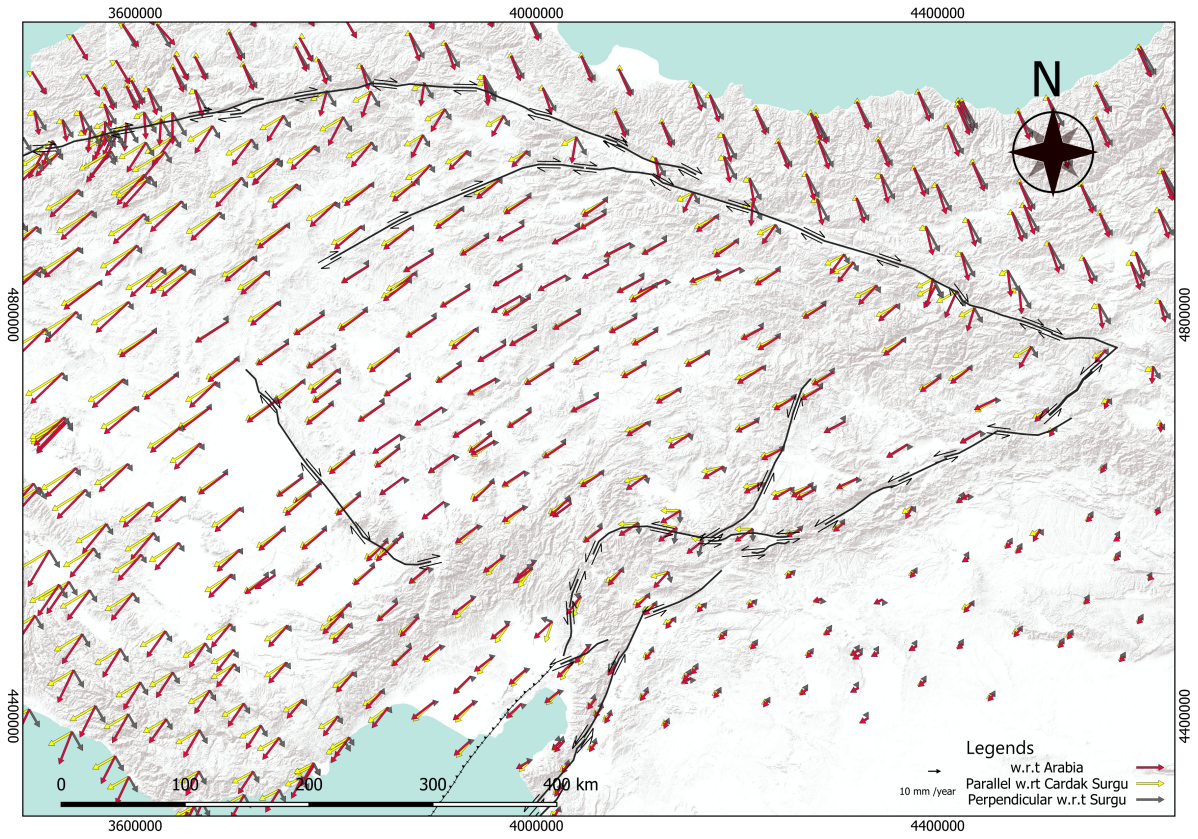

(b) Arabia relative to Çardak–Sürgü Fault

Figure 5.5: Parallel and perpendicular velocity components relative to Anatolia and Arabia reference frames for the Çardak–Sürgü Fault.

5.2.4. Cross Sections

The AEM Toolbox provides fault–aligned projections by evaluating the complex field in the plane $z = x + iy$ and projecting vectors onto the local fault–tangent and fault–normal directions. In our workflow, faults are modelled as *no–flow* boundaries. This makes the AEM solution discontinuous across the fault plane: normal (perpendicular) projection lines generated from one side terminate at the boundary and do not extend through to the other side. However, the model we use requires continuous cross–sections that represent both sides of the fault.

To construct such cross–sections, we proceed as follows:

1. Place an evenly spaced set of anchor points along the mapped fault trace.
2. At each anchor, compute the local strike α and the corresponding unit normal $\mathbf{n}$.
3. From each side of the fault, trace a short normal ray along $\pm\,\mathbf{n}$ (one ray per side) and sample the AEM fields (Φ, Ψ) and vector components $(v_{\parallel}, v_{\perp})$.
4. Stitch the two rays into a single *straight* cross–section that traverses the fault: we align their directions and merge them at the fault location to obtain one continuous line that spans both sides.

This integration of the two one–sided perpendicular projections is essential: the AEM enforces a discontinuity at the fault, whereas our representation demands a continuous cross–fault profile. By connecting the normals across the boundary, we create a geometrically consistent cross–section on which the fault–parallel and fault–perpendicular components can be evaluated and compared on both sides of the fault. Finally, coordinates are mapped back to UTM.

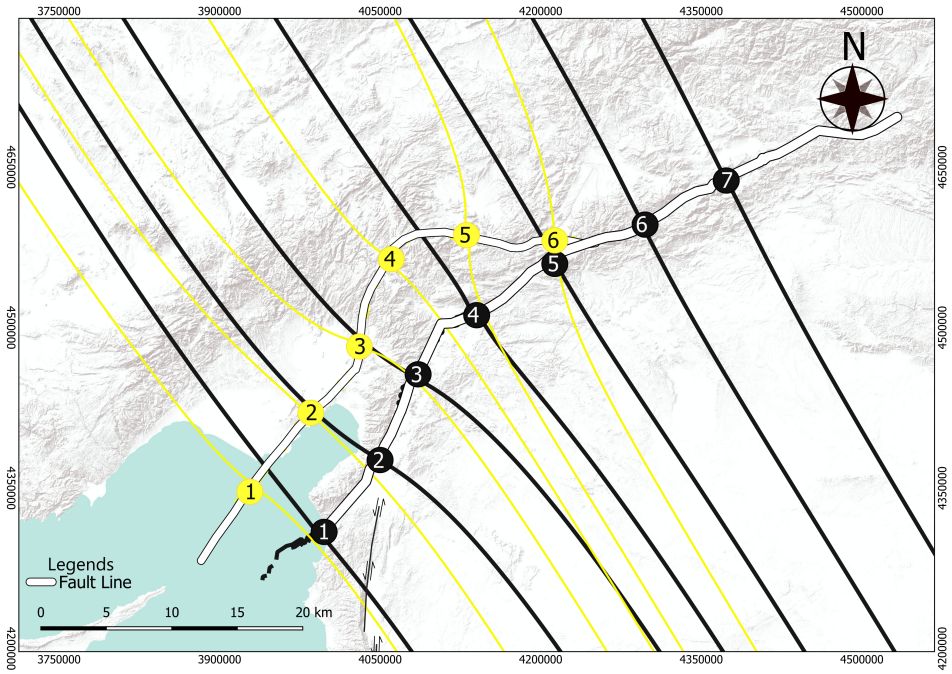

Figure 5.6: Cross Sections projection in UTM.
The yellow line shows the perpendicular projection with respect to the EAFZ Fault, and the Black line shows the perpendicular projection with respect to the Cardak Surgu Fault. Black dots represent the cross-section of the Cardak Surgu Fault, and White dots represent the cross-section of the Mainstrand Fault.

In this research, for the EAFZ, the spacing between the cross-sections is 90 Km and for the Çardak–Sürgü fault, it is 85 Km. These values are chosen to ensure adequate cross-sectional coverage of the model while allowing a sufficient number of observations per cross-section to reduce the risk of overfitting.

5.3. Linear Weighting

The ensemble produces fault–aligned velocity predictions along a set of predefined cross–sections (see Section 5.2.4). To compare these predictions with the GPS, we map the model output to each GPS station. With the AEM Toolbox, each station is represented in the complex plane as $Z = x+iy$. Because the perpendicular coordinate is the real part of the complex position, we use $\Re(Z)$ to compute the interpolation weights. Every station lies in a z coordinate, and they lie between two modeled sections at z_{low} and z_{high} with different real parts $\Re(z_{\text{low}})$ and $\Re(z_{\text{high}})$. The linear weights are

$$w_{\text{low}} = \frac{\Re(z_{\text{high}}) - \Re(z_{\text{GPS}})}{\Re(z_{\text{high}}) - \Re(z_{\text{low}})}, \qquad w_{\text{high}} = \frac{\Re(z_{\text{GPS}}) - \Re(z_{\text{low}})}{\Re(z_{\text{high}}) - \Re(z_{\text{low}})}, \qquad w_{\text{low}} + w_{\text{high}} = 1.$$

The fault–parallel and fault–perpendicular components at the station are then.

$$v_c(z_{\text{GPS}}) = w_{\text{low}}\, v_c(z_{\text{low}}) + w_{\text{high}}\, v_c(z_{\text{high}})$$

Applied member–wise to the ensemble.

If a station is influenced by two faults (Sürgü and the Main Strand of the EAFZ), we perform the same interpolation for each fault separately and then add the contributions from both faults:

$$v(z_{\text{GPS}}) = v^{(\text{Sürgü})}(z_{\text{GPS}}) + v^{(\text{Mainstrand})}(z_{\text{GPS}})$$

Below in Figure 5.7, we identify which GPS stations are influenced by both faults and which stations are constrained by the deformation of a single fault. Since the main strand of the EAFZ is longer than the Sürgü Fault, it is expected that some GPS stations are affected only by the EAFZ and not by the Çardak–Sürgü Fault. On the other hand, all GPS stations influenced by the Çardak–Sürgü Fault are also affected by the main strand of the EAFZ.

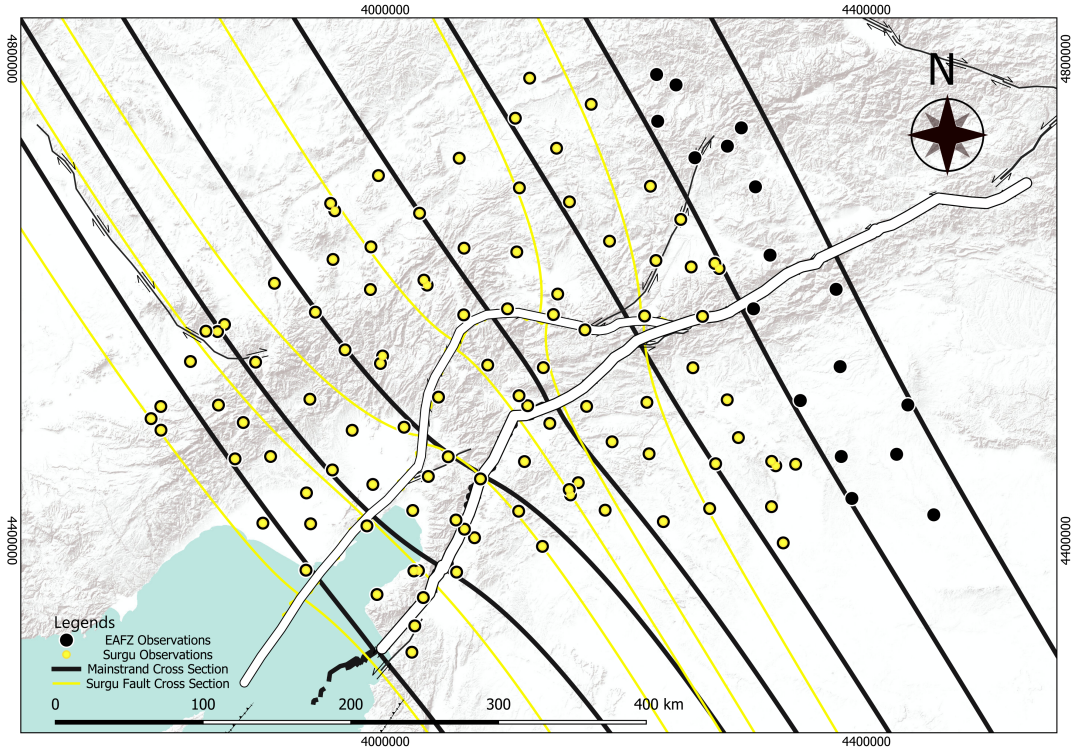

Figure 5.7: GPS Influence Scheme. Black dots represent stations primarily influenced by the main strand of the EAFZ, while yellow dots represent those influenced by the Çardak–Sürgü Fault. Stations shown with both black and yellow markers indicate sites where the observations are influenced by the mechanism of both faults.

5.4. Data Assimilation

Data assimilation combines prior information from a model with observed data to obtain the best estimates of a system along with its uncertainty. The basis of data assimilation lies in the Bayesian theorem. Data assimilation, in general, is divided into two steps, assimilation and forecasting steps, according to Carrassi et al. (2018). The assimilation steps consist of incorporating the observed data into the observed model to update its current states, and the forecasting steps predict the future behaviour of the model based on the updated state. Similarly, data assimilation can be used to estimate the model parameters, forcing or controls according to (Evensen et al., 2022). The aim of data assimilation in general is not only to produce the best fits but also to produce the best state or parameters that respect the underlying physics of an event.

Data assimilation can follow two approaches: sequential and non-sequential. In sequential assimilation, observations are incorporated step by step in time. After each assimilation step, the model is updated to provide a forecast based on the previous observations, until new observations become available and the assimilation process takes place again. On the other hand, non-sequential data assimilation uses current, past, and future observations. Here, future refers to observations that occur after the time of interest but are already available in the dataset. Non-sequential assimilation is therefore often applied for reanalysis or parameter inference(Carrassi et al., 2018).

5.4.1. Bayesian Theorem

Bayes' Theorem is a foundational concept in probability theory, initially developed in the 18th century by the English statistician and theologian Thomas Bayes. Bayes proposed this theorem to address problems of causality—reasoning about causes given observed effects. In its purest form, Bayes' Theorem is an initial belief modified by objective new information (McGrayne, 2011). Our initial beliefs (prior) using recent objective data would become the new and improved belief (posterior). Several years later, Bayes' Theorem resurfaced in a much simpler form, presented as a mathematical equation that we recognise today. The discovery or perhaps the resurgence of Bayes' Theorem originated with Pierre Simon Laplace during his studies on estimating the orbits and positions of astronomical objects in the universe, where observations were scarce and noisy. Laplace uses Bayes' theorem and probability as its basis to solve these problems. Today, Bayes' Theorem is widely used across disciplines, including statistics, machine learning, and decision theory, offering a rigorous framework for reasoning under uncertainty.

Bayes' Theorem is commonly written as:

$$P(A \mid B) = \frac{P(B \mid A)\, P(A)}{P(B)}. \tag{5.1}$$

In many applications, such as Bayesian inference, the probability $P(A|B)$ represents event A happening given observations B, and $P(B|A)$ is the likelihood of observing B when A is true. We are typically interested in how the observation of B influences our belief about various possible hypotheses from $P(A)$. In such cases, the denominator $P(B)$ is constant across different hypotheses $P(A)$. Since we are comparing posterior probabilities across varying $P(A)$ instead of $P(B)$, the normalising constant can be ignored. From Bayes' theorem, we can expand it to the Bayes' Rule, which shows the proportionality of posterior to the product of likelihood and prior.

$$P(A \mid B) \propto P(A) \cdot P(B \mid A). \tag{5.2}$$

5.4.2. Kalman Filter

The classic Kalman Filter is an algorithm that uses a series of measurements over time, including statistical noise, to produce estimates of unknown variables (Carrassi et al., 2018). The Kalman Filter operates in two main steps: prediction and update at each time step t=1,2,…,k. The filter first predicts the state and its uncertainty, and then updates this prediction using new observations.

$$y_k = H_k x_k + v_k, \qquad v_k \sim \mathcal{N}_m(0, R_k) \tag{5.3}$$
$$x_k = M_k x_{k-1} + w_k, \qquad w_k \sim \mathcal{N}_n(0, Q_k) \tag{5.4}$$

Equation 5.3 and equation 5.4 are the observations and forecast model, respectively with y_k being the prediction of data with m dimensional data vector at time k, x_k is the n - dimensional unobserved state vector of interest and v_k and w_k as the observation and forecast error. R_k and Q_k are the covariance matrices of the observation process noise. H_k is the observation matrix that relates the state to the observations linearly, and M_k is the propagator matrix that determines how the state evolves. This framework shows that the goal at every time point t = 1, 2,..., is to obtain the filtering distribution of the state after every timestep. In Bayesian terms, this is equivalent to the conditional distribution of x_k given $y_{1:k}$ and is denoted by $x_k|y_{1:k}$.

The prediction steps are created through a prescribed prior without any involvement regarding the observations that are made. On the other hand, the update steps incorporate the discrepancies by multiplying the difference between the observations and the predictions by the Kalman Gain. The Kalman Gain is a value which determines how much weight is given to the observation relative to the prior prediction. A high Kalman gain indicates that the observation is more trusted, so the filter firmly corrects the prior estimate using the measurement. A low Kalman Gain, on the other hand, suggests greater confidence in the prior, so the observation has less influence on the updated state. Mathematically, Kalman Gain is computed as the product of the cross-covariance between the state and the observation, and the inverse of the auto-covariance of the observation.

$$K = \underbrace{P_{xx} H^\top}_{P_{xy}} \underbrace{\left(H P_{xx} H^\top + R\right)^{-1}}_{P_{yy}^{-1}} \tag{5.5}$$

The KF updates the state estimate recursively and sequentially, processing each new observation as it becomes available. At every forecast step, it updates the mean and covariance, which means that the current estimates always depend on the results from previous time steps.

$$x_k^f = M_{k,k-1} x_{k-1}^a, \tag{5.6}$$
$$P_k^f = M_{k,k-1} P_{k-1}^a M_{k,k-1}^\top + Q_k. \tag{5.7}$$

$$x_k^a = x_k^f + K_k \left(y_k - H_k x_k^f\right) \tag{5.8}$$
$$P_k^a = (I - K_k H_k) P_k^f \tag{5.9}$$

As can be seen from the x_k^a and P_k^a, which represent the updated mean and covariance at time k respectively, while x_k^f and P_k^f represent the prediction of the model from previous time steps respectively.

Gaussian Assumption

The Kalman Filter assumes that both the forecast error and the observation error follow a Gaussian distribution. The Gaussian distribution only requires its mean and variance to represent the distribution, which then simplifies the representation and propagation of uncertainty within the filter. Gaussian distributions are also recursive because if the multivariate distribution is a Gaussian, then the conditional distribution of the multivariate Gaussian distribution would still be Gaussian, which again plays in our hands, as it only needs its mean and moments to define the distributions.

5.4.3. Ensemble Kalman Filter (EnKF)

The classic Kalman Filter is constrained to systems governed by linear state transition models and assumes that all probability density functions (PDFs)—including those associated with model and observation errors—are Gaussian. The Ensemble Kalman Filter (EnKF) addresses these limitations by representing the system's state distribution through a finite ensemble of state vectors (Katzfuss et al., 2016). Conceptually, the EnKF can be viewed as a Monte Carlo approximation of the standard Kalman Filter, wherein the state distribution is sampled using the mean and covariance of a prescribed prior. This ensemble, generated via stochastic sampling, reflects possible realisations of the system state and evolves.

Unlike the Kalman Filter, which requires the explicit propagation of a full covariance matrix, the EnKF estimates covariances directly from the ensemble members. Maintaining the fundamental structure of the Kalman Filter, the EnKF still consists of two sequential operations at each time step: a forecast (prediction) step and an update (assimilation) step. While the ensemble-based formulation allows the EnKF to operate effectively in nonlinear contexts, its performance remains optimal when the prior and error distributions are approximately Gaussian. Although the Monte Carlo sampling approach provides robustness against some non-Gaussian behaviour, the EnKF still fundamentally assumes Gaussian statistics, which may limit its accuracy in highly skewed settings or bi-modal distributions. Given an ensemble of realisations from a prescribed prior distribution for the states resembling:

$$\mathbf{X}^{f,a} = \begin{bmatrix} \mathbf{x}_1^{f,a} & \dots & \mathbf{x}_N^{f,a} \end{bmatrix} \in \mathbb{R}^{m \times N}, \tag{5.10}$$

The EnKF forecast steps are obtained using the state space model given in 5.4.

$$y_k^{(i)} = H_k x_k^{(i)} + v_k, \qquad v_k \sim \mathcal{N}_m(0, R_k) \tag{5.11}$$

$$x_k^{(i)} = M_k x_{k-1}^{(i)} + w_k, \qquad w_k \sim \mathcal{N}_n(0, Q_k) \tag{5.12}$$

Despite its differences, the Kalman Gain itself retains its original form, which is the product of cross-covariance and the inverse of the autocovariance.

$$\mathbf{P}_{xx} = \frac{1}{N-1}\mathbf{X}\mathbf{X}^\top, \tag{5.13}$$

$$\mathbf{P}_{xy} = \frac{1}{N-1}\mathbf{X}\mathbf{Y}^\top, \tag{5.14}$$

$$\mathbf{P}_{yy} = \frac{1}{N-1}\mathbf{Y}\mathbf{Y}^\top + \mathbf{R} \tag{5.15}$$

$$\boxed{\mathbf{K} = \mathbf{P}_{xy}\left(\mathbf{P}_{yy} + R\right)^{-1}} \tag{5.16}$$

The algorithm for EnKF is presented in Appendix A

5.4.4. Ensemble Kalman Smoother

The key difference between the Ensemble Kalman Filter (EnKF) and the Ensemble Kalman Smoother (EnKS) lies in the treatment of observational data. In EnKF, the analysis is performed sequentially, using observations at each time step y_{obs}^n. In contrast, the EnKS performs a smoother update by incorporating all available observations across time steps simultaneously. This allows the EnKS to correct past states or parameters using both current and future observations, making it particularly useful for parameters that do not change dynamically over time and static problems.

The algorithm of the Ensemble Kalman Filter (EnKS) that are used in this research. In the following algorithm, the notation for time could be represented by $\mathbf{x}_{1:K}^{i,f}$, meaning that the EnKS considers all current and future observations. To simplify those equation the $\mathbf{x}_{1:K}^{i,f}$ would be simplify to $\mathbf{x}^{i,f}$.

Algorithm 4 Ensemble Smoother (ES)

Input:
N: Number of ensemble members
$\{\mathbf{x}^i\}_{i=1}^N$: Prior ensemble of model parameters
$M(\cdot)$: Forecast model operator
$H(\cdot)$: Observation operator
$\mathbf{y}^{\text{obs}}$: Observed data vector
$\mathbf{R}$: Observation error covariance matrix

Output: Updated ensemble $\{\mathbf{x}^i\}_{i=1}^N$
Forecast Step:
for $i = 1$ to N **do**
  $\mathbf{x}^{i,f} \leftarrow M(\mathbf{x}^i) + v^i$
  $\hat{\mathbf{y}}^{i,f} \leftarrow H(\mathbf{x}^{i,f}) + w^i$
end for
Stack forecast ensembles:
  $\mathbf{x}^f = [\mathbf{x}^1, \ldots, \mathbf{x}^N]$
  $\hat{\mathbf{Y}}^f = [\hat{\mathbf{y}}^{1,f}, \ldots, \hat{\mathbf{y}}^{N,f}]$
Compute ensemble means:
  $\bar{\mathbf{x}}^f = \text{mean}(\mathbf{X}^f)$
  $\bar{\hat{\mathbf{y}}}^f = \text{mean}(\hat{\mathbf{Y}}^f)$
Compute anomalies:
  $\mathbf{X}' = \mathbf{X}^f - \bar{\mathbf{X}}^f$
  $\hat{\mathbf{Y}}' = \hat{\mathbf{Y}}^f - \bar{\hat{\mathbf{y}}}^f$
Estimate covariances:
  $\mathbf{P}_{xy} = \frac{1}{N-1}\mathbf{X}'(\hat{\mathbf{Y}}')^\top$
  $\mathbf{P}_{yy} = \frac{1}{N-1}\hat{\mathbf{Y}}'(\hat{\mathbf{Y}}')^\top$
Compute Kalman gain:
  $\mathbf{K} = \mathbf{P}_{xy}(\mathbf{P}_{yy} + \mathbf{R})^{-1}$
Analysis Step:
for $i = 1$ to N **do**
  Sample: $\boldsymbol{\varepsilon}^i \sim \mathcal{N}(0, \mathbf{R})$
  Perturbed obs: $\mathbf{y}^i = \mathbf{y}^{\text{obs}} + \boldsymbol{\varepsilon}^i$
  Innovation: $\boldsymbol{\delta}^i = \mathbf{y}^i - \hat{\mathbf{y}}^{i,f}$
  Update: $\mathbf{x}^{i,a} = \mathbf{x}^i + \mathbf{K}\boldsymbol{\delta}^i$
end for

5.5. Data Assimilation Set-Up

5.5.1. Generate Ensemble of Parameters

The model parameters follow the formulations of Savage and Burford (1973) and Segall (2013). Each parameter ensemble is assumed to follow a Gaussian distribution, requiring its first two moments (μ, σ) to describe the distribution. The joint inversion utilised the equations given in Eq. 4.3 and Eq. 4.1. In the initial setup, all parameters in these equations were assumed to follow independent Gaussian distributions $\mathcal{N}(\mu, \sigma)$. The ensemble size was set to 2,000, resulting in 2,000 realisations for each parameter.

The prior distributions for strike-slip velocity, dip-slip velocity, and locking depth were chosen based on values reported in previous research (Kurt et al., 2023; Özbey et al., 2024; Reilinger et al., 2006; Vavra et al., 2024), ensuring consistency with established estimates for the EAFZ and Çardak–Sürgü Fault. In contrast, the parameters α and β do not have direct sources in the literature, and the prior for α and β for both setups is presented in the Appendix along with a full table of the priors **??**.

Table 5.1: Prior distribution parameters used for generating the dip-slip ensemble. Strike-slip, dip-slip, and locking depth are based on values from previous studies, while α and β are exploratory parameters (see Appendix A.2).

Parameter	Mean (μ)	std.Dev (σ)
Strike-slip velocity, V_s	5	5
Dip-slip velocity, V_d	0	7
Locking depth, D	10	10
α	3	5
β	0	10

For the dip angle, the Çardak–Sürgü Fault is taken to have a value of $75°$. For the main strand of the EAFZ, the dip angles for each segment are adopted from Güvercin et al. (2022), except for the Amanos segment, where in this study a dip angle of $85°$ is assumed. The complete list of dip angles is provided in the table below.

Table 5.2: Assigned dip angles for the EAFZ cross-sections.

Cross-section	Dip angle (°)
1	85
2	85
3	85
4	60
5	70
6	70
7	70

5.5.2. Log-space transformation of locking depth priors

To ensure non-negative values for the locking depth, the ensemble is sampled in log-space. Data assimilation is carried out in log-space by converting the locking depth from the physical space. Gaussian parameters to the log-space parameters $(\mu_{\text{log}}, \sigma_{\text{log}})$, which are derived from the properties of the lognormal distribution:

$$\mu_{\text{log}} = \ln\left(\frac{\mu_{\text{phys}}^2}{\sqrt{\mu_{\text{phys}}^2 + \sigma_{\text{phys}}^2}}\right), \qquad \sigma_{\text{log}} = \sqrt{\ln\left(1 + \frac{\sigma_{\text{phys}}^2}{\mu_{\text{phys}}^2}\right)}. \tag{5.17}$$

Sampling is then performed in log-space:

$$D_{\text{log}} \sim \mathcal{N}(\mu_{\text{log}}, \sigma_{\text{log}}^2), \tag{5.18}$$

and values are mapped back to physical space through the exponential, since the model requires the real physical locking depth D:

$$D = e^{D_{\text{log}}}. \tag{5.19}$$

5.5.3. Observations

The observations that we use in this research as the original data are the velocity with respect to Anatolia, transformed from the original velocity with respect to the Eurasia plate. The transformations used are explained in the previous chapter, specifically the rotation matrix shown in algorithm 3. We translate the observation that we use in this research into a matrix.

$$\mathbf{y}_{\text{obs}} = \begin{bmatrix} v_{(1)} \\ v_{(2)} \\ v_{(3)} \\ v_{(4)} \\ \vdots \\ v_{(m)} \end{bmatrix}$$

The data assimilation process in this research is done on both faults simultaneously; hence, to make the assimilated velocity in a coherent velocity frame, I decide to use the velocity of the observation of the Easting and Northing components as the observations for the data assimilation process. Thus, the matrix has twice the observations as the velocity is decomposed into the Easting and Northing components, the following $\mathbf{y}_{\text{obs}}$ will then be presented in a $2m \times 1$ matrix.

$$\mathbf{y}_{\text{obs}} = \begin{bmatrix} v_E^{(1)} \\ v_N^{(1)} \\ v_E^{(2)} \\ v_N^{(2)} \\ \vdots \\ v_E^{(m)} \\ v_N^{(m)} \end{bmatrix}$$

5.5.4. Ensemble Matrix

Let C be the number of cross-sections, and let each cross–section use $d = 5$ parameters (strike–slip rate V_s, dip–slip rate V_d, locking depth D, and shape/rake parameters α, β). For cross–section c, define the parameter vector

$$\boldsymbol{\theta}_c \;=\; \begin{bmatrix} V_s^c \\ V_d^c \\ D^c \\ \alpha^c \\ \beta^c \end{bmatrix} \in \mathbb{R}^d.$$

Stacking all cross–sections gives the state vector.

$$\mathbf{x} \;=\; \begin{bmatrix} \boldsymbol{\theta}_1 \\ \boldsymbol{\theta}_2 \\ \vdots \\ \boldsymbol{\theta}_C \end{bmatrix} \in \mathbb{R}^{dC}.$$

The data assimilation uses an ensemble of N members. We arrange the prior ensemble as a matrix whose columns are members:

$$\mathbf{X}_{\text{prior}} \;=\; \begin{bmatrix} | & | & & | \\ \mathbf{x}^{(1)} & \mathbf{x}^{(2)} & \cdots & \mathbf{x}^{(N)} \\ | & | & & | \end{bmatrix} \;\in\; \mathbb{R}^{dC \times N}.$$

At each assimilation step, the algorithm updates (per cross–section) the strike–slip (V_s), dip–slip (V_d), locking depth (D), and the shape parameters (α, β); D is common to both the strike– and dip–slip components, but is inverted jointly within the same state. For each ensemble member, the forward model projects fault slip onto the cross-sections, and the resulting velocities are interpolated to the GPS stations using linear weights (see Section 5.2.4). The forecast matrix is defined as

$$\mathbf{Y}_{\text{forecast}} = \mathcal{H}(\mathbf{X}_{\text{prior}}) \;\in\; \mathbb{R}^{2m \times N},$$

Where $\mathcal{H}(\cdot)$ denotes the forward operator mapping slip parameters to station velocities, linear weighting. The predicted velocity for every station for every ensemble member n is

$$\widehat{\mathbf{v}}_i^{(n)} = w_{\text{low},i}\, \mathbf{v}^{(n)}(z_{\text{low},i}) + w_{\text{high},i}\, \mathbf{v}^{(n)}(z_{\text{high},i}), \qquad \widehat{\mathbf{v}}_i^{(n)} \in \mathbb{R}^2,$$

with $w_{\text{low},i}, w_{\text{high},i}$ the linear interpolation weights based on $\Re(z)$. Stacking the contributions from all m stations yields the forecast matrix $\mathbf{Y}_{\text{forecast}} \in \mathbb{R}^{2m \times N}$.

$$\mathbf{X}_{\text{prior}} \in \mathbb{R}^{dC \times N}, \quad \mathbf{y}_{\text{obs}} \in \mathbb{R}^{2m \times 1}, \quad \mathbf{Y}_{\text{forecast}} \in \mathbb{R}^{2m \times N}.$$

These three objects $(\mathbf{X}_{\text{prior}}, \mathbf{y}_{\text{obs}}, \mathbf{Y}_{\text{forecast}})$ are the inputs required by the EnKS algorithm (Algorithm 4).

$$\mathbf{Y}_{\text{forecast}} = \begin{bmatrix} v_E^{(1,1)} & v_E^{(1,2)} & \cdots & v_E^{(1,N)} \\ v_N^{(1,1)} & v_N^{(1,2)} & \cdots & v_N^{(1,N)} \\ v_E^{(2,1)} & v_E^{(2,2)} & \cdots & v_E^{(2,N)} \\ v_N^{(2,1)} & v_N^{(2,2)} & \cdots & v_N^{(2,N)} \\ \vdots & \vdots & \ddots & \vdots \\ v_E^{(m,1)} & v_E^{(m,2)} & \cdots & v_E^{(m,N)} \\ v_N^{(m,1)} & v_N^{(m,2)} & \cdots & v_N^{(m,N)} \end{bmatrix} \in \mathbb{R}^{2m \times N}$$

The EnKS proceeds with the filtering process and updates the prior by the observations, resulting in a newly obtained posterior for every parameter.

$$\mathbf{X}_{\text{prior}} = \begin{bmatrix} x_1^{(1)} & x_1^{(2)} & \cdots & x_1^{(N)} \\ x_2^{(1)} & x_2^{(2)} & \cdots & x_2^{(N)} \\ \vdots & \vdots & \ddots & \vdots \\ x_{dc}^{(1)} & x_{dc}^{(2)} & \cdots & x_{dc}^{(N)} \end{bmatrix} \in \mathbb{R}^{dc \times N}$$

This algorithm retrieves the posterior for the parameters X_{post}, and the predictions y_{pred} for every station. In the process of obtaining the Kalman Gain, we took the observation error covariance matrix into account. The error covariance matrix is a square matrix with dimensions $m \times m$.

$$\mathbf{R} = \begin{bmatrix} \sigma_{E,1}^2 & \rho_{EN,1}\sigma_{E,1}\sigma_{N,1} & 0 & 0 & \cdots & 0 \\ \rho_{EN,1}\sigma_{E,1}\sigma_{N,1} & \sigma_{N,1}^2 & 0 & 0 & \cdots & 0 \\ 0 & 0 & \sigma_{E,2}^2 & \rho_{EN,2}\sigma_{E,2}\sigma_{N,2} & \cdots & 0 \\ 0 & 0 & \rho_{EN,2}\sigma_{E,2}\sigma_{N,2} & \sigma_{N,2}^2 & \cdots & 0 \\ \vdots & \vdots & \vdots & \vdots & \ddots & \vdots \\ 0 & 0 & 0 & 0 & \cdots & \sigma_{N,m}^2 \end{bmatrix} \in \mathbb{R}^{2m \times 2m} \tag{5.20}$$

5.5.5. Output

After the filtering step, the posterior parameter values are obtained in a matrix form consistent with that of the prior ensemble. These updated parameters serve as inputs to the forward model. By propagating them through the model and applying the inversion procedure, we generate predictions that can be directly compared with the observations. This allows us to assess both the quality of the predicted velocities and the plausibility of the estimated parameters.

$$\mathbf{X}_{\text{posterior}} = \begin{bmatrix} x_1^{(1)} & x_1^{(2)} & \cdots & x_1^{(N)} \\ x_2^{(1)} & x_2^{(2)} & \cdots & x_2^{(N)} \\ \vdots & \vdots & \ddots & \vdots \\ x_{dc}^{(1)} & x_{dc}^{(2)} & \cdots & x_{dc}^{(N)} \end{bmatrix} \in \mathbb{R}^{dc \times N}$$

The y_{analysis} is the velocities obtained using the posterior parameters.

$$\mathbf{y}_{\text{analysis}} = \begin{bmatrix} v_E^{(1,1)} & v_E^{(1,2)} & \cdots & v_E^{(1,N)} \\ v_N^{(1,1)} & v_N^{(1,2)} & \cdots & v_N^{(1,N)} \\ v_E^{(2,1)} & v_E^{(2,2)} & \cdots & v_E^{(2,N)} \\ v_N^{(2,1)} & v_N^{(2,2)} & \cdots & v_N^{(2,N)} \\ \vdots & \vdots & \ddots & \vdots \\ v_E^{(m,1)} & v_E^{(m,2)} & \cdots & v_E^{(m,N)} \\ v_N^{(m,1)} & v_N^{(m,2)} & \cdots & v_N^{(m,N)} \end{bmatrix} \in \mathbb{R}^{2m \times N}$$

6

Results

This chapter presents the results of our model, followed by a discussion that also addresses its limitations and provides recommendations for future research

The estimate of EAFZ using the inversion and data obtained is presented in the table below.

6.1. Estimated Parameters for Mainstrand EAFZ

Table 6.1: Posterior parameter estimates for Main strand using GNSS data relative to Anatolia (Mean $\pm$ Std).

Segment	Slip Deficit Rate (mm/yr)	Dip Slip Deficit Rate (mm/yr)	Locking Depth (km)	α (mm/yr)	β (mm/yr)
1	3.21 ± 1.07	-7.47 ± 1.33	19.95 ± 6.33	3.10 ± 0.52	-0.90 ± 0.16
2	7.89 ± 0.69	-10.98 ± 0.97	50.20 ± 11.04	6.47 ± 0.41	0.13 ± 0.26
3	5.63 ± 0.46	-11.33 ± 1.06	24.75 ± 6.23	7.40 ± 0.30	-1.26 ± 0.32
4	4.42 ± 0.36	-0.59 ± 0.44	11.36 ± 2.18	7.71 ± 0.25	-3.32 ± 0.21
5	2.39 ± 0.33	-1.44 ± 0.69	0.39 ± 0.08	5.61 ± 0.19	-3.10 ± 0.17
6	6.18 ± 0.11	1.40 ± 0.26	10.60 ± 1.38	7.42 ± 0.04	-0.41 ± 0.04
7	6.59 ± 0.15	-6.74 ± 0.29	1.91 ± 0.43	6.99 ± 0.04	-0.92 ± 0.04

In hindsight, we could observe that the Slip-Deficit rate all have positive values, while the dip-slip rates around the main strand EAFZ are varied. The locking depth shows some variable results, from 1 Km to 41 Km.

6.1.1. Estimated Parameters for the Mainstrand EAFZ using GNSS data in the Arabia-fixed reference frame

Table 6.2: Posterior parameter estimates for the Main strand using GNSS data relative to Arabia (Mean $\pm$ Std).

Segment	Slip Deficit Rate (mm/yr)	Dip Slip Deficit Rate (mm/yr)	Locking Depth (km)	α (mm/yr)	β (mm/yr)
1	1.53 ± 1.11	-20.59 ± 1.35	5.76 ± 1.80	-2.04 ± 0.54	-4.85 ± 0.16
2	6.48 ± 0.67	-2.65 ± 0.98	28.61 ± 6.12	0.52 ± 0.40	-5.91 ± 0.25
3	10.39 ± 0.44	-12.15 ± 1.06	43.21 ± 10.92	1.98 ± 0.32	-6.98 ± 0.31
4	0.28 ± 0.36	-1.97 ± 0.56	5.03 ± 0.94	7.62 ± 0.25	-1.73 ± 0.21
5	0.15 ± 0.33	3.17 ± 0.67	5.64 ± 1.10	11.46 ± 0.19	-0.58 ± 0.18
6	9.32 ± 0.11	2.85 ± 0.26	40.42 ± 5.50	8.15 ± 0.04	0.43 ± 0.04
7	8.80 ± 0.15	-6.62 ± 0.30	6.40 ± 1.50	8.12 ± 0.04	1.33 ± 0.04

6.2. Estimated Parameters for Çardak-Sürgü Fault

Table 6.3: Posterior parameter estimates for Çardak - Sürgü Fault with velocity relative to Anatolia (Mean $\pm$ Std).

Segment	Slip Deficit Rate (mm/yr)	Dip Slip Deficit Rate (mm/yr)	Locking Depth (km)	α (mm/yr)	β (mm/yr)
1	1.64 ± 0.90	3.24 ± 1.10	5.15 ± 1.37	4.21 ± 0.45	0.52 ± 0.15
2	3.74 ± 0.33	-0.70 ± 0.48	27.15 ± 6.51	2.44 ± 0.27	-0.54 ± 0.22
3	1.18 ± 0.38	-6.65 ± 0.48	55.68 ± 12.39	-0.47 ± 0.31	-0.72 ± 0.34
4	3.50 ± 0.22	-4.01 ± 0.48	67.08 ± 14.01	-0.59 ± 0.23	1.70 ± 0.24
5	1.98 ± 0.39	-3.80 ± 0.62	3.12 ± 0.72	-1.29 ± 0.26	2.08 ± 0.23
6	1.63 ± 0.38	5.01 ± 0.74	25.82 ± 6.76	0.74 ± 0.19	3.84 ± 0.17

In the Çardak–Sürgü fault, we could also see that the slip deficit rate obtained all have positive values, while the dip-slip and locking depth rate varied along the fault.

6.2.1. Estimated Parameters for Çardak-Sürgü Fault using GNSS data in relative to Arabia

Table 6.4: Posterior parameter estimates for the Çardak-Sürgü Fault using GNSS data in relative to Arabia (Mean $\pm$ Std).

Segment	Slip Deficit Rate (mm/yr)	Dip Slip Deficit Rate (mm/yr)	Locking Depth (km)	α (mm/yr)	β (mm/yr)
1	2.48 ± 0.94	-3.62 ± 1.11	2.30 ± 0.62	12.14 ± 0.46	3.81 ± 0.15
2	10.17 ± 0.32	10.38 ± 0.49	70.96 ± 16.71	7.93 ± 0.26	6.65 ± 0.22
3	4.25 ± 0.36	4.88 ± 0.47	25.06 ± 5.35	6.49 ± 0.31	5.83 ± 0.33
4	5.42 ± 0.21	3.84 ± 0.44	163.13 ± 32.66	4.33 ± 0.24	5.68 ± 0.24
5	6.02 ± 0.38	-6.26 ± 0.64	49.91 ± 11.50	0.90 ± 0.26	1.05 ± 0.22
6	6.03 ± 0.38	-2.39 ± 0.73	1.55 ± 0.39	-4.05 ± 0.20	1.35 ± 0.17

6.3. Posterior, Observed and Residual

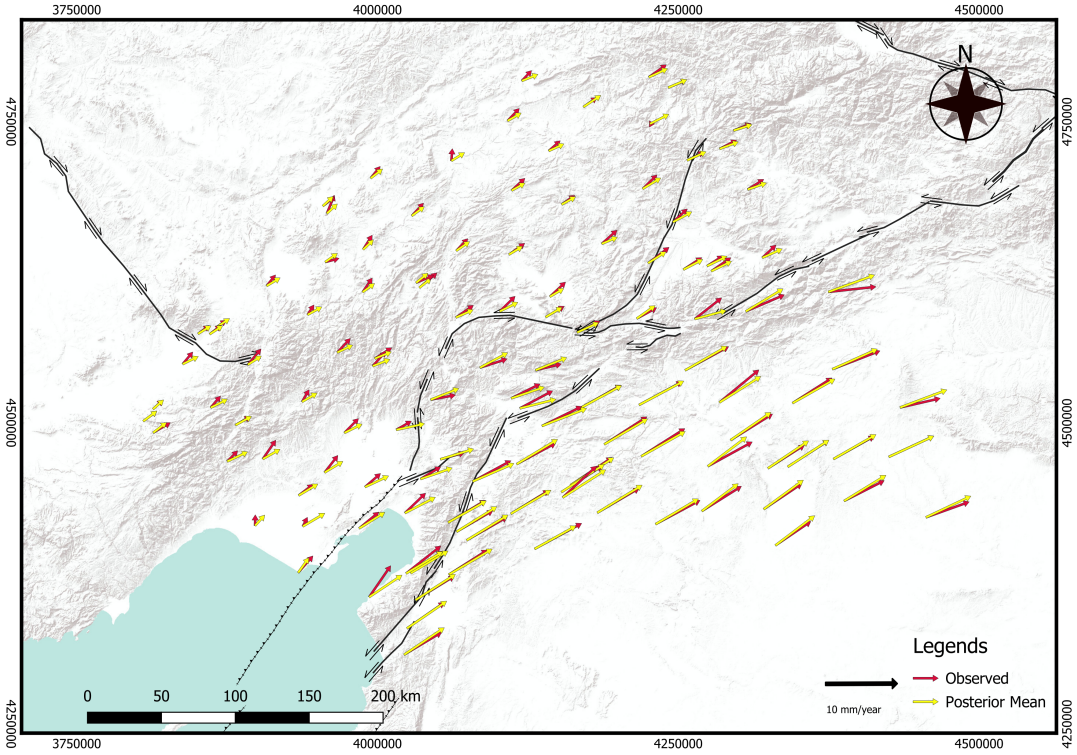

(a) Posterior vs Observations w.r.t Anatolia

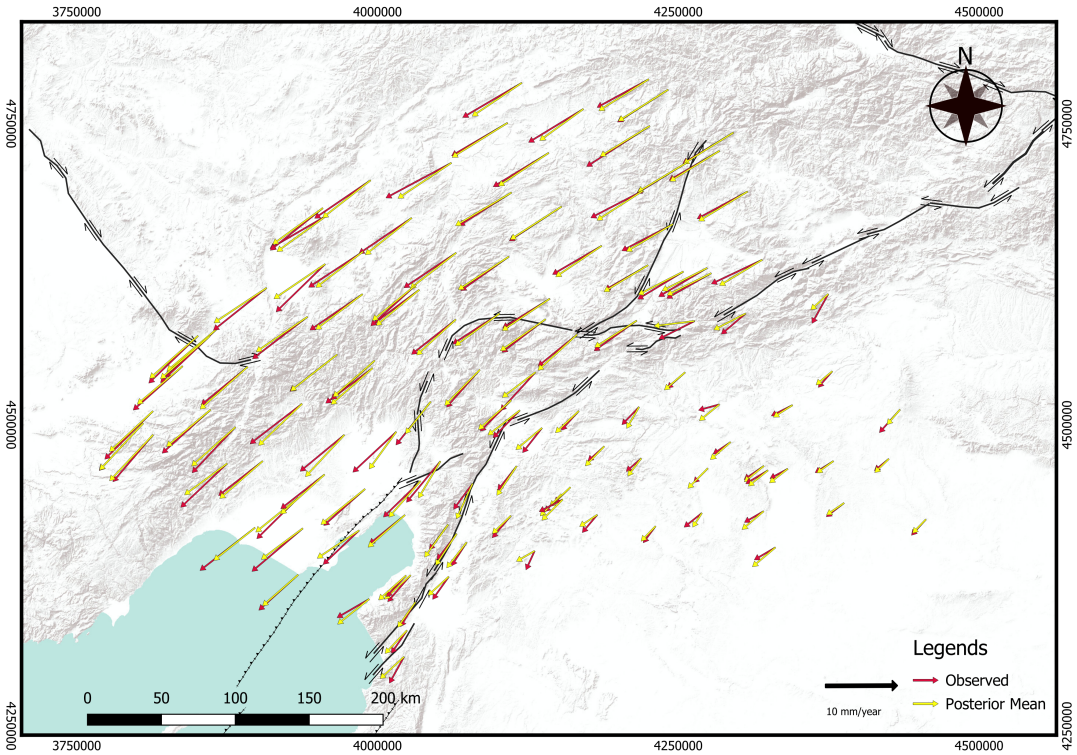

(b) Posterior vs Observations w.r.t Arabia

Figure 6.1: Comparison of posterior predictions with observations for (a) Anatolia and (b) Arabia.

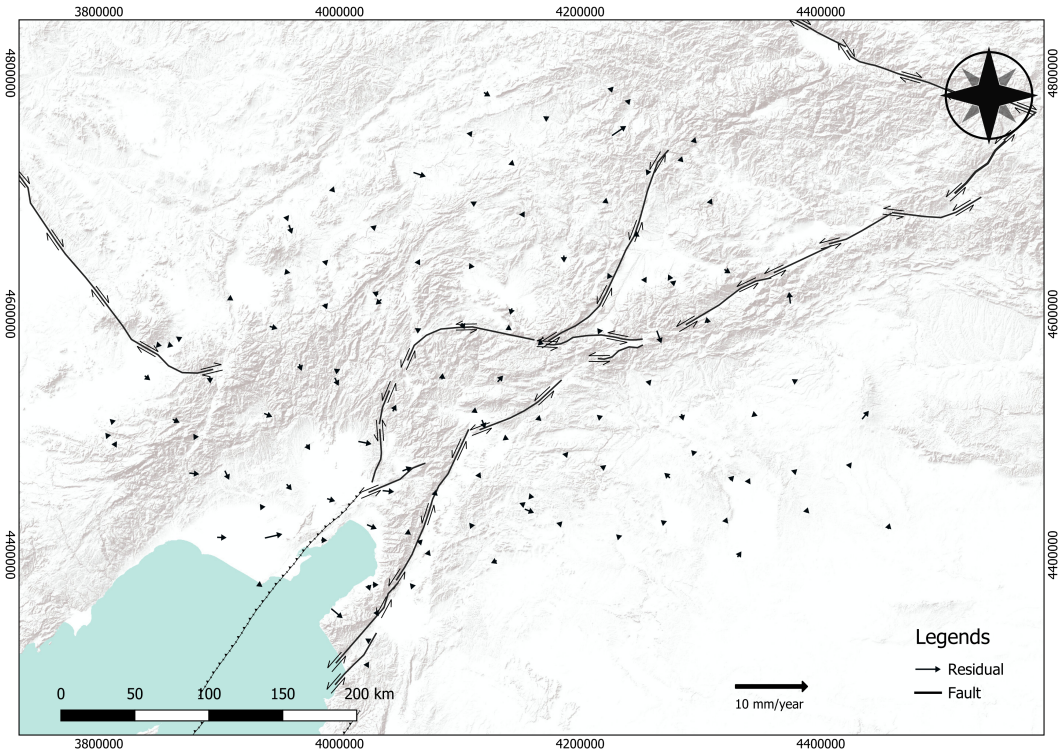

(a) Residual with respect to Anatolia

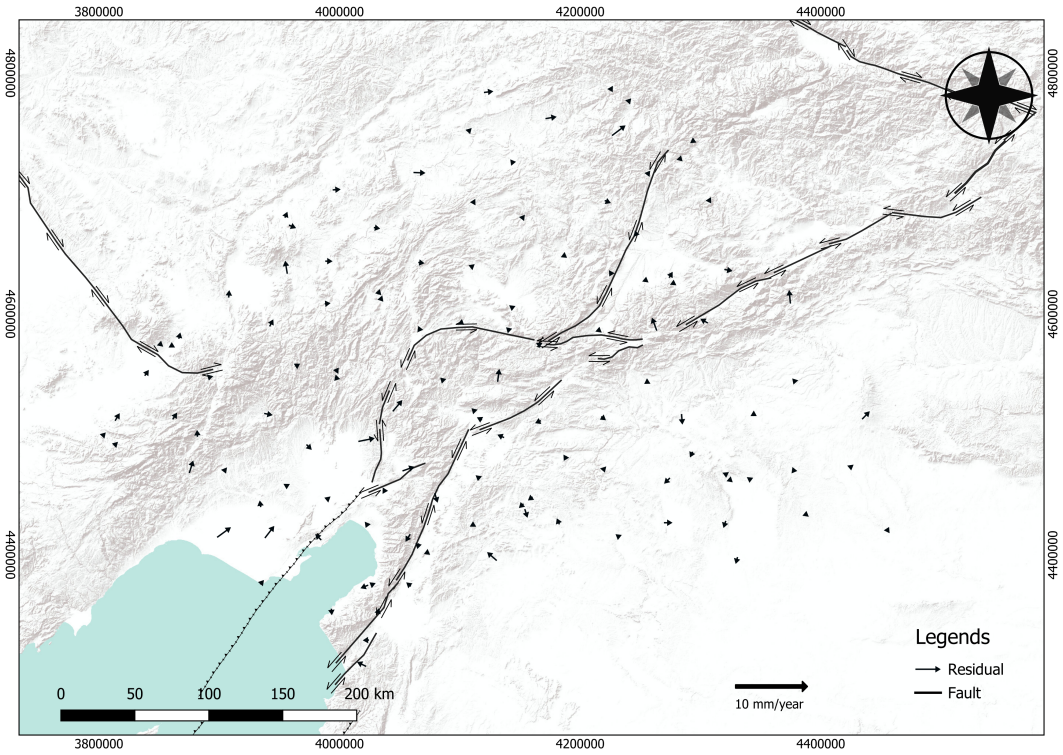

(b) Residual with respect to Arabia

Figure 6.2: Residual distributions comparing observations with posterior predictions for (a) Anatolia and (b) Arabia.

From Figure 6.1, we observe the velocities predicted using the posterior mean obtained through data assimilation and the model compared with the observations and Figure 6.2 presents the residuals,

shown for both the Arabia- and Anatolia-fixed relative velocity frames.

6.4. Parameter Distribution

6.4.1. Mainstrand EAFZ relative Anatolia

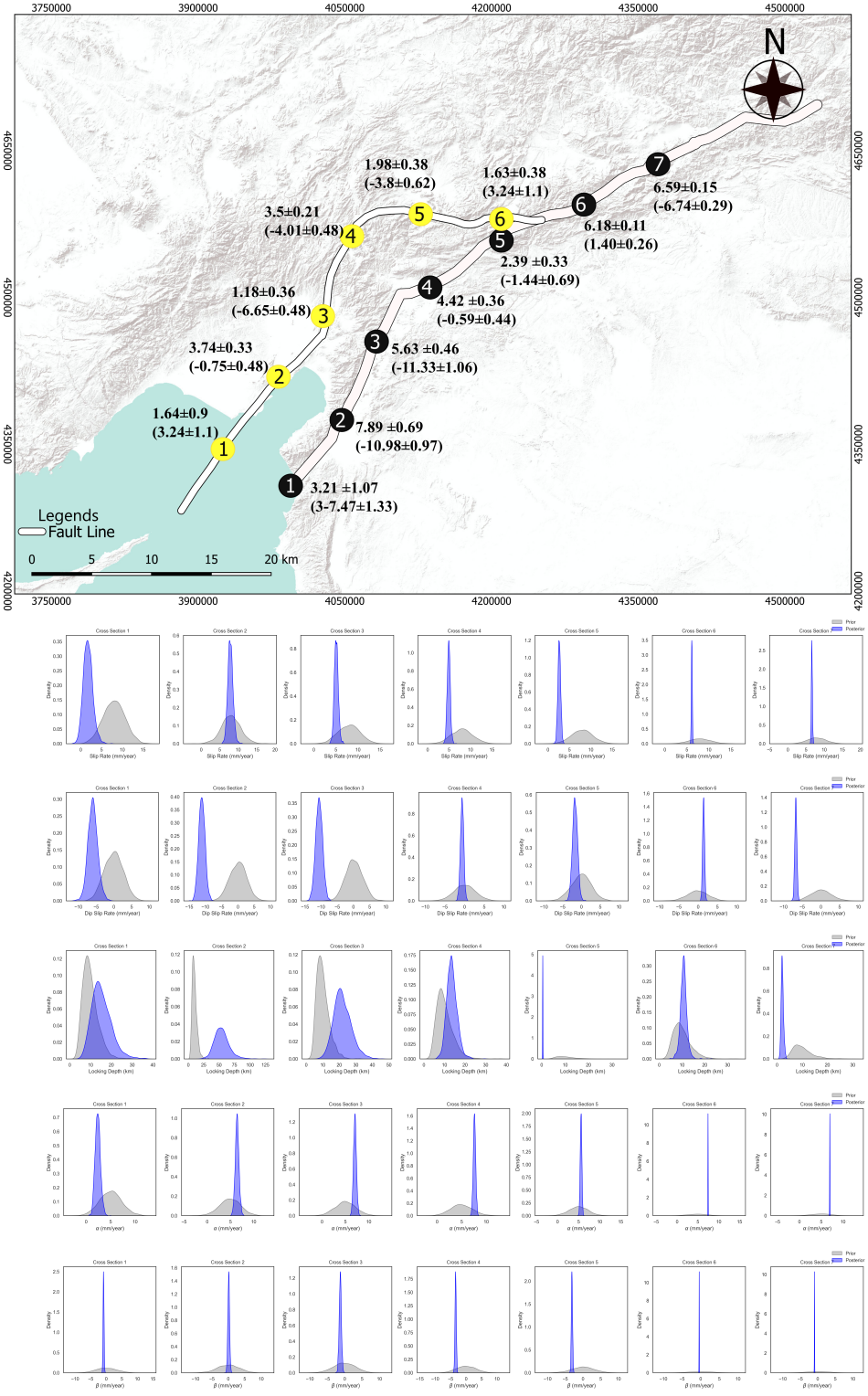

Posterior parameter distributions and estimation results for the Main Strand of the EAFZ.

6.4.2. Çardak–Sürgü relative Anatolia

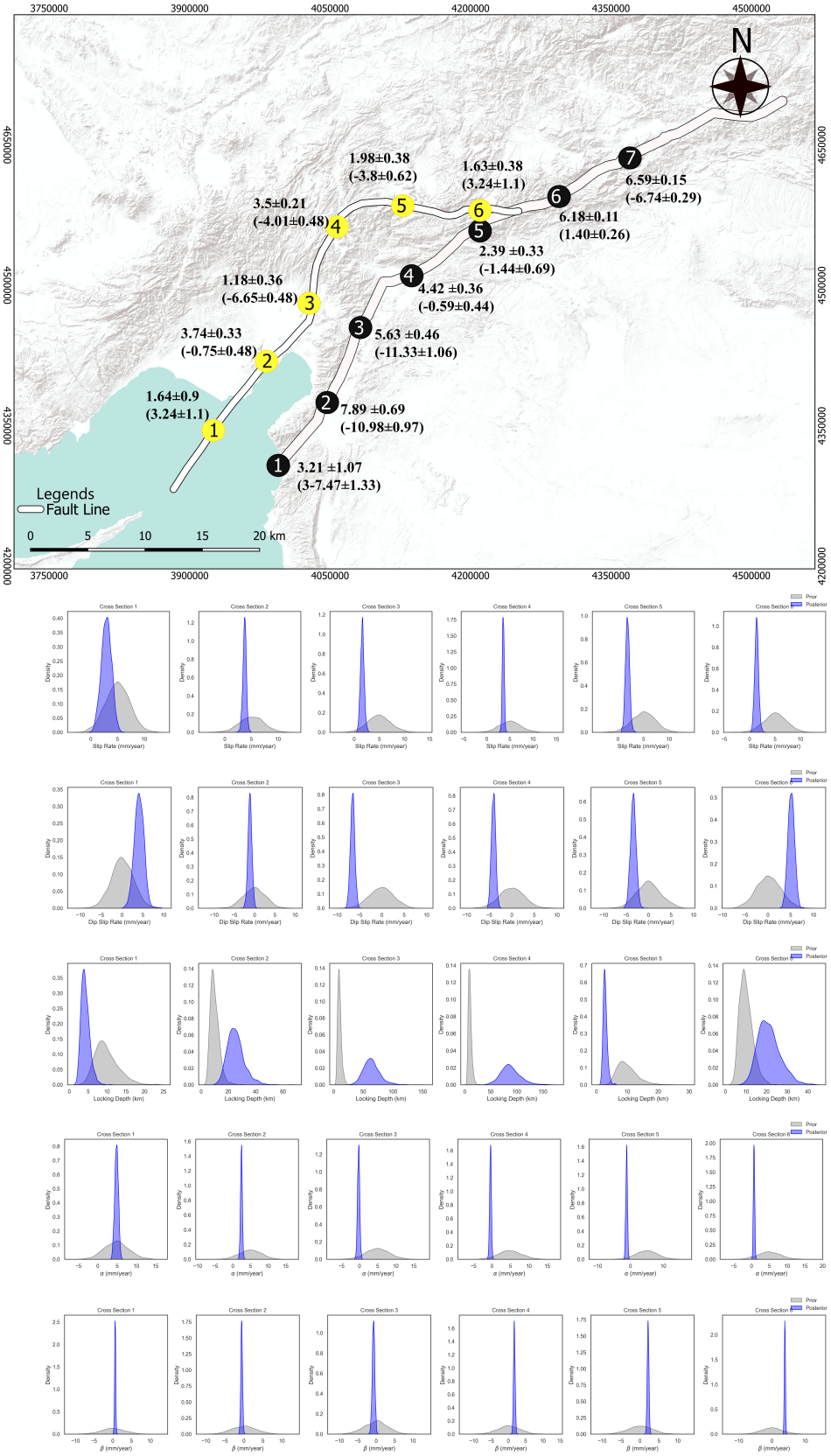

Posterior parameter distributions and estimation results for the Çardak–Sürgü segment of the EAFZ relative to Anatolia.

6.4.3. Main Strand EAFZ relative Arabia

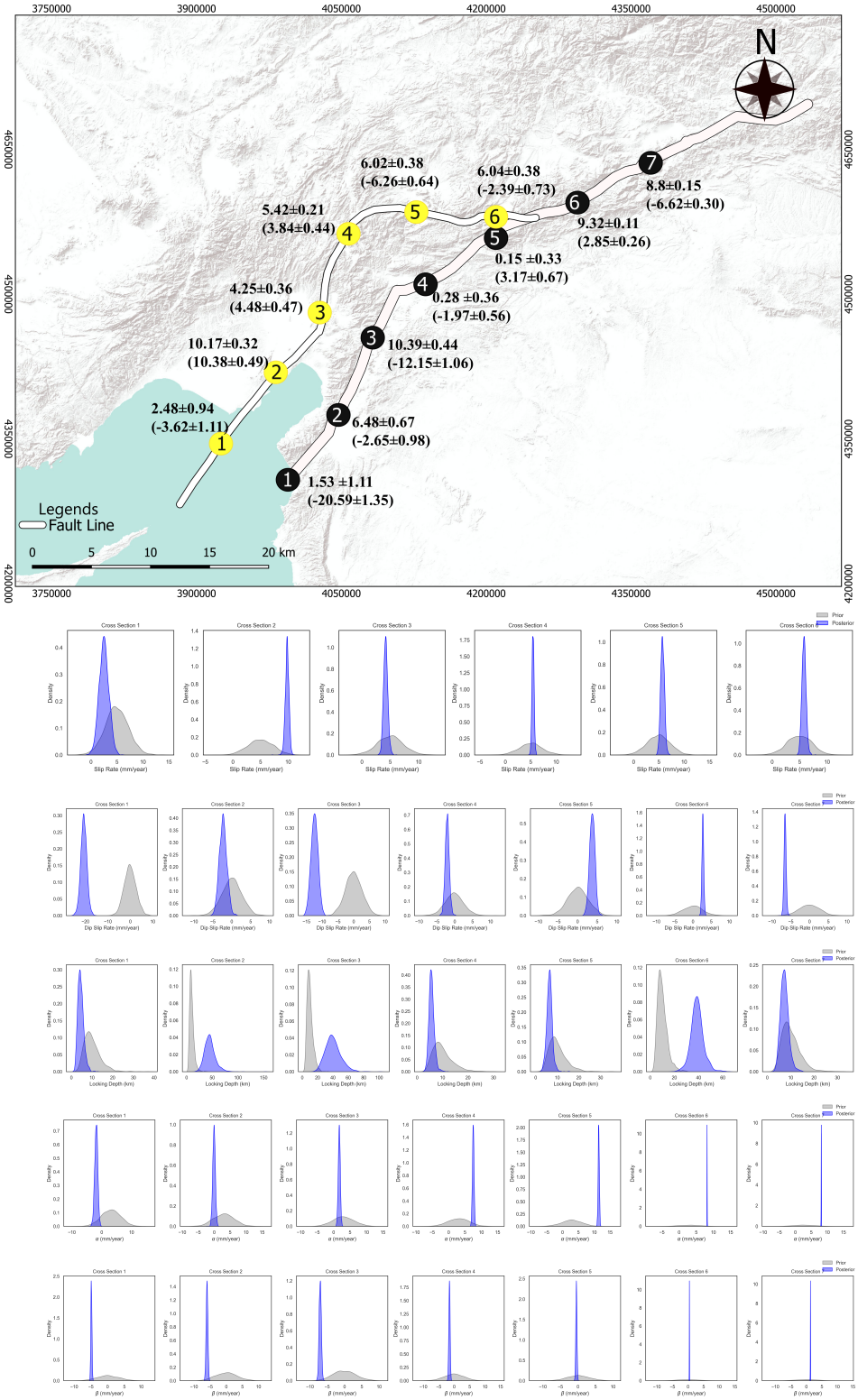

Posterior parameter distributions and estimation results for the Main Strand of the EAFZ relative to Arabia.

6.4.4. Çardak–Sürgü relative Arabia

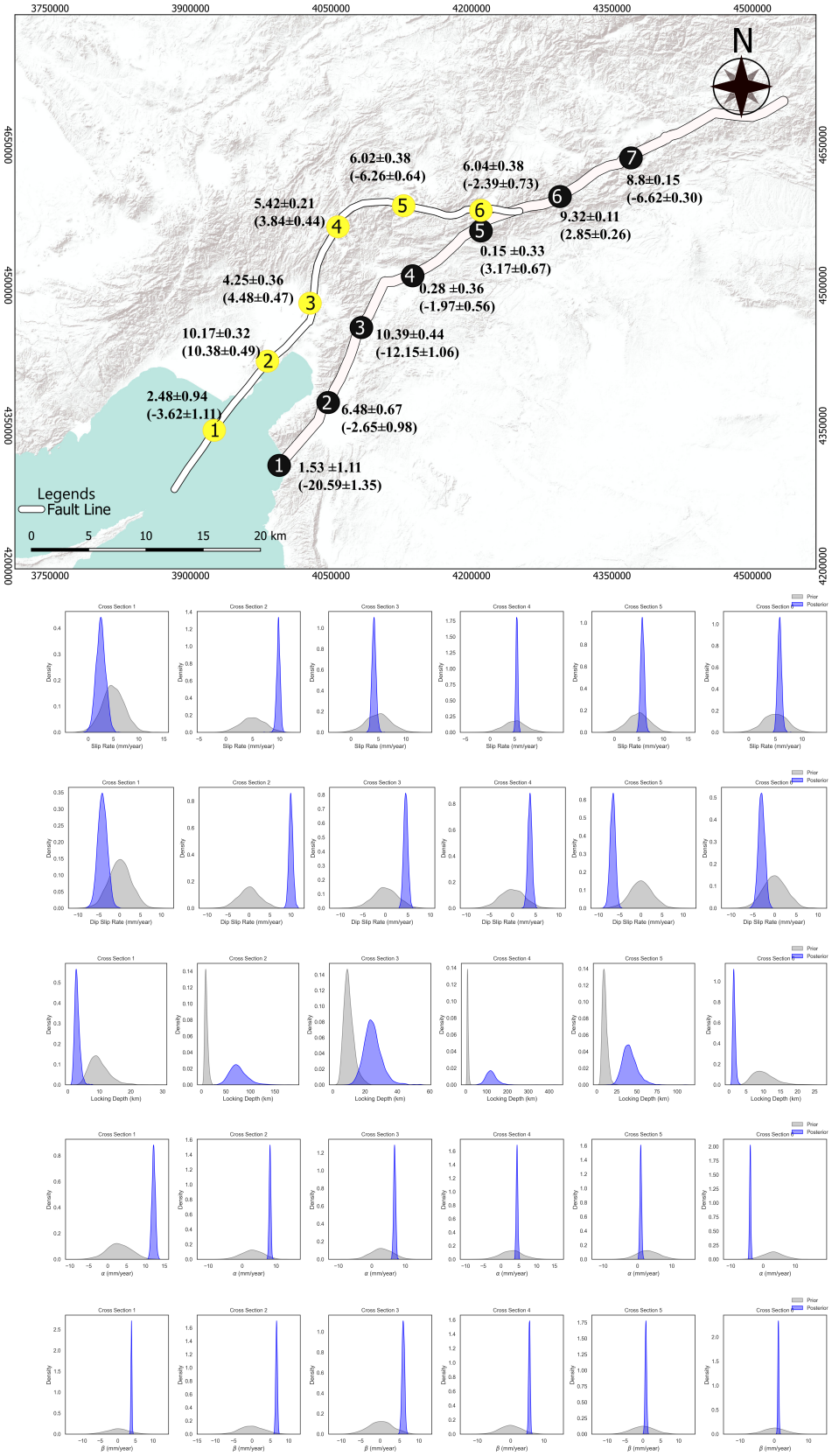

Posterior parameter distributions and estimation results for the Çardak–Sürgü segment of the EAFZ relative to Arabia.

6.5. Velocity Profiles Across Cross Sections

6.5.1. Velocity Profiles Parallel to Main Strand Fault EAFZ

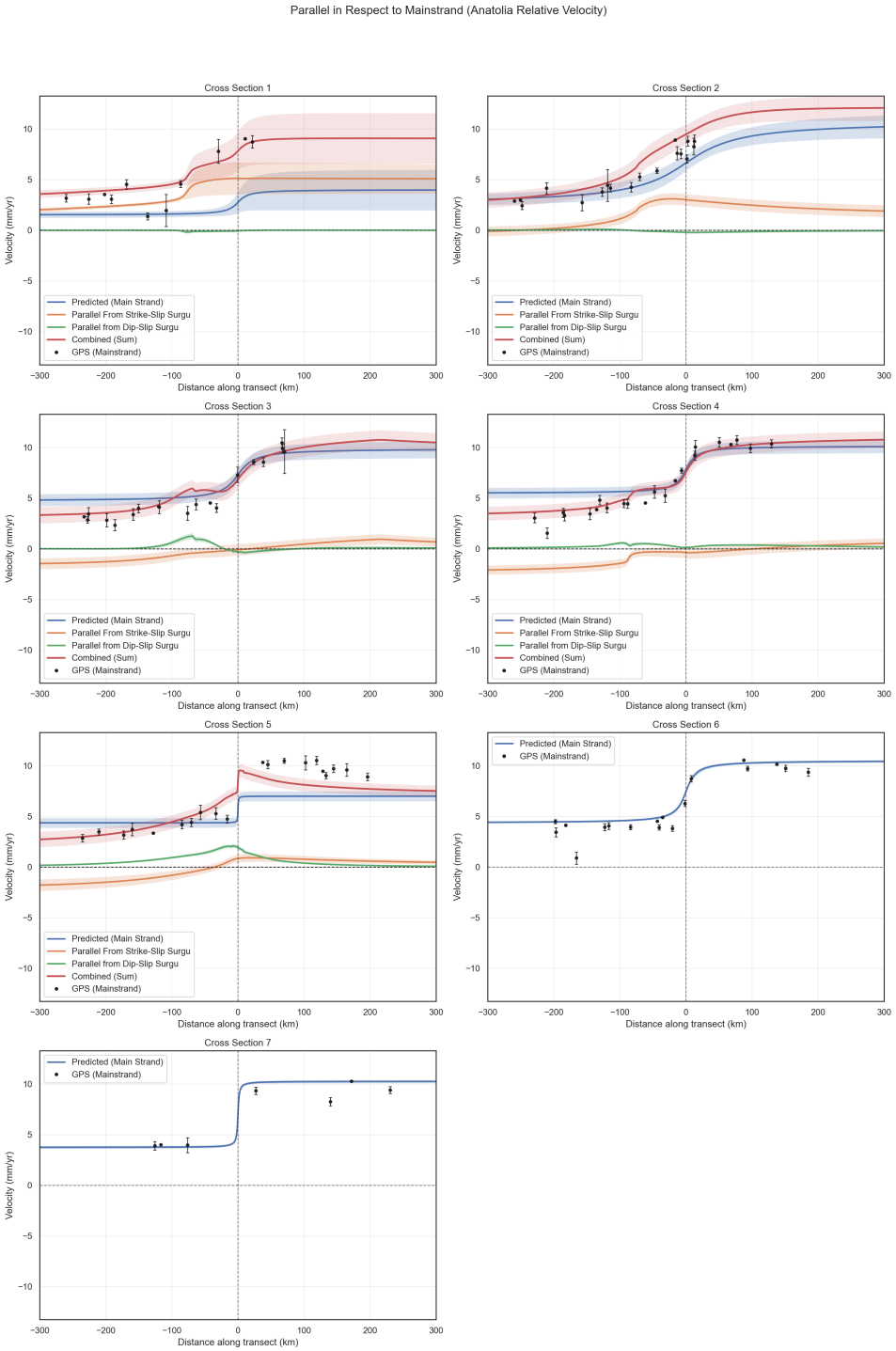

Figure 6.3: Parallel w.r.t Main Strand EAFZ (Anatolia Relative Velocity)

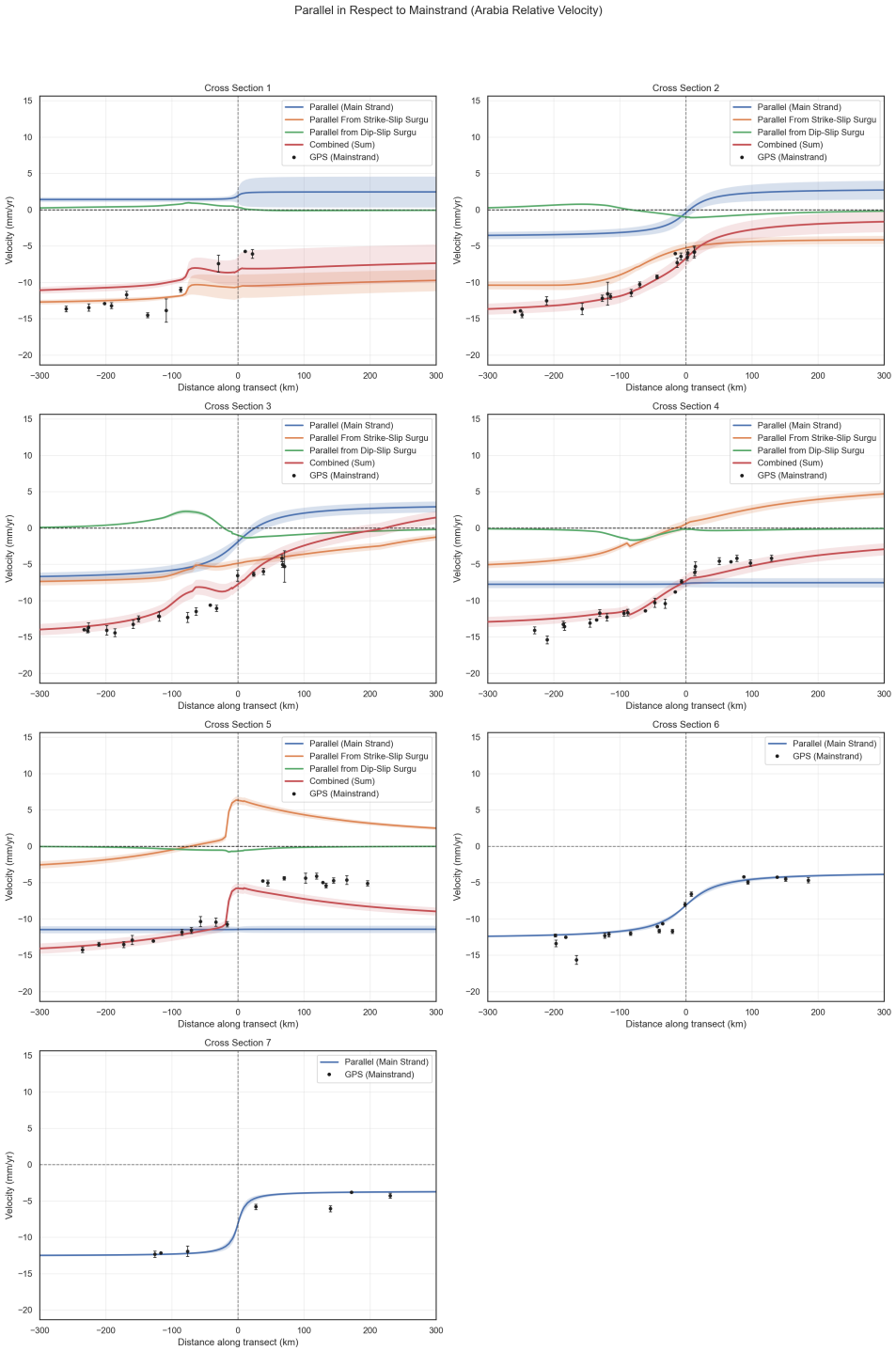

Figure 6.4: Parallel w.r.t Main Strand EAFZ(Arabia Relative)

6.5.2. Velocity Profiles Parallel to Çardak-Sürgü Fault

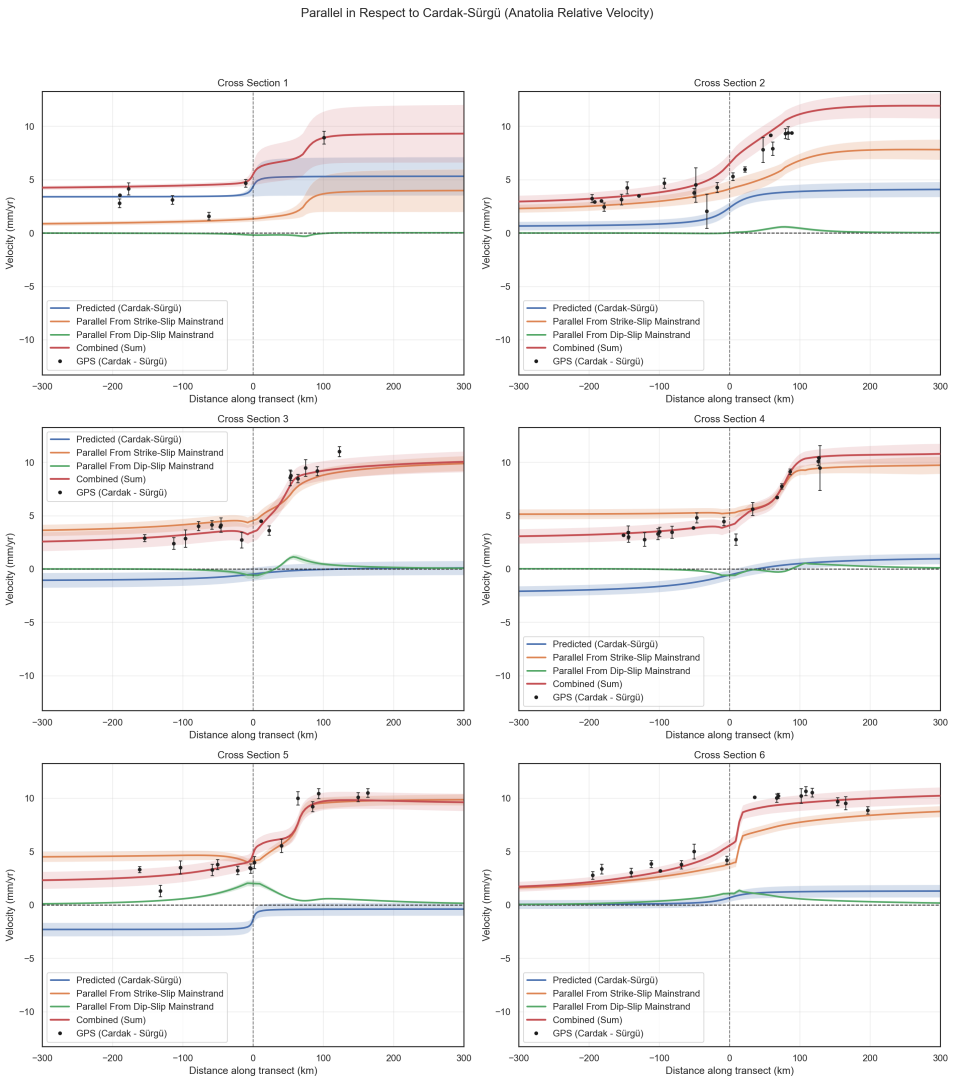

Figure 6.5: Parallel w.r.t Çardak-Sürgü (Anatolia Relative Velocity)

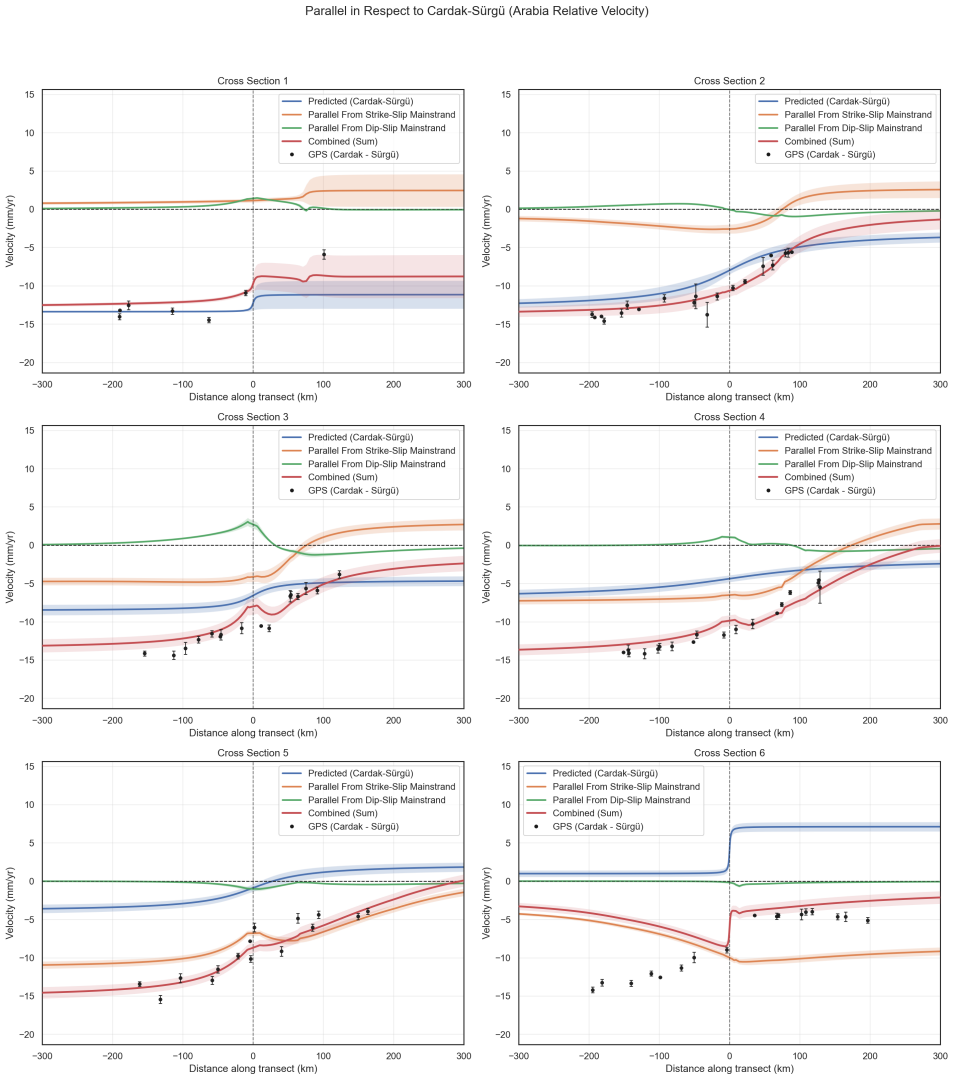

Figure 6.6: Parallel w.r.t Çardak-Sürgü (Arabia Relative Velocity)

The red line represents the resultant sum of all parallel component contributions. These include the parallel component estimated from the strike-slip model at its own cross-section, the parallel component contributions from other faults, and the parallel component arising from the dip-slip of other faults. The dashed line represents the fault that serves as the reference for each profile. In Figure 6.3 and Figure 6.4, the dashed line at zero marks the location of the main strand, since the figure shows the parallel component relative to the Main Strand. In Figure 6.5 and Figure 6.6, the dashed line indicates the location of the Çardak–Sürgü Fault, as the figure displays the parallel component relative to that fault.

6.5.3. Velocity Profiles Perpendicular to Main Strand Fault EAFZ

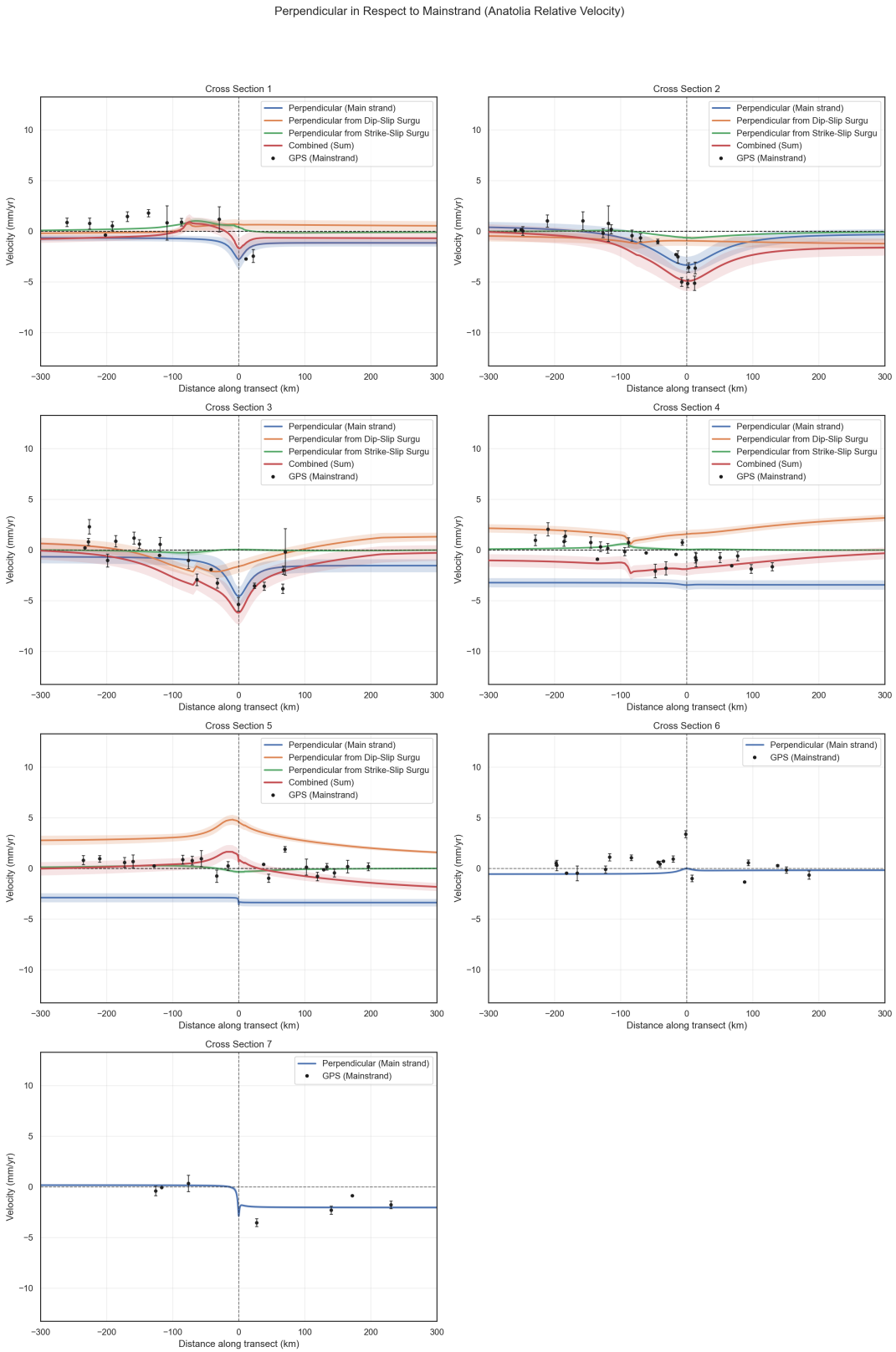

Figure 6.7: Perpendicular w.r.t Main Strand EAFZ (Anatolia Relative Velocity)

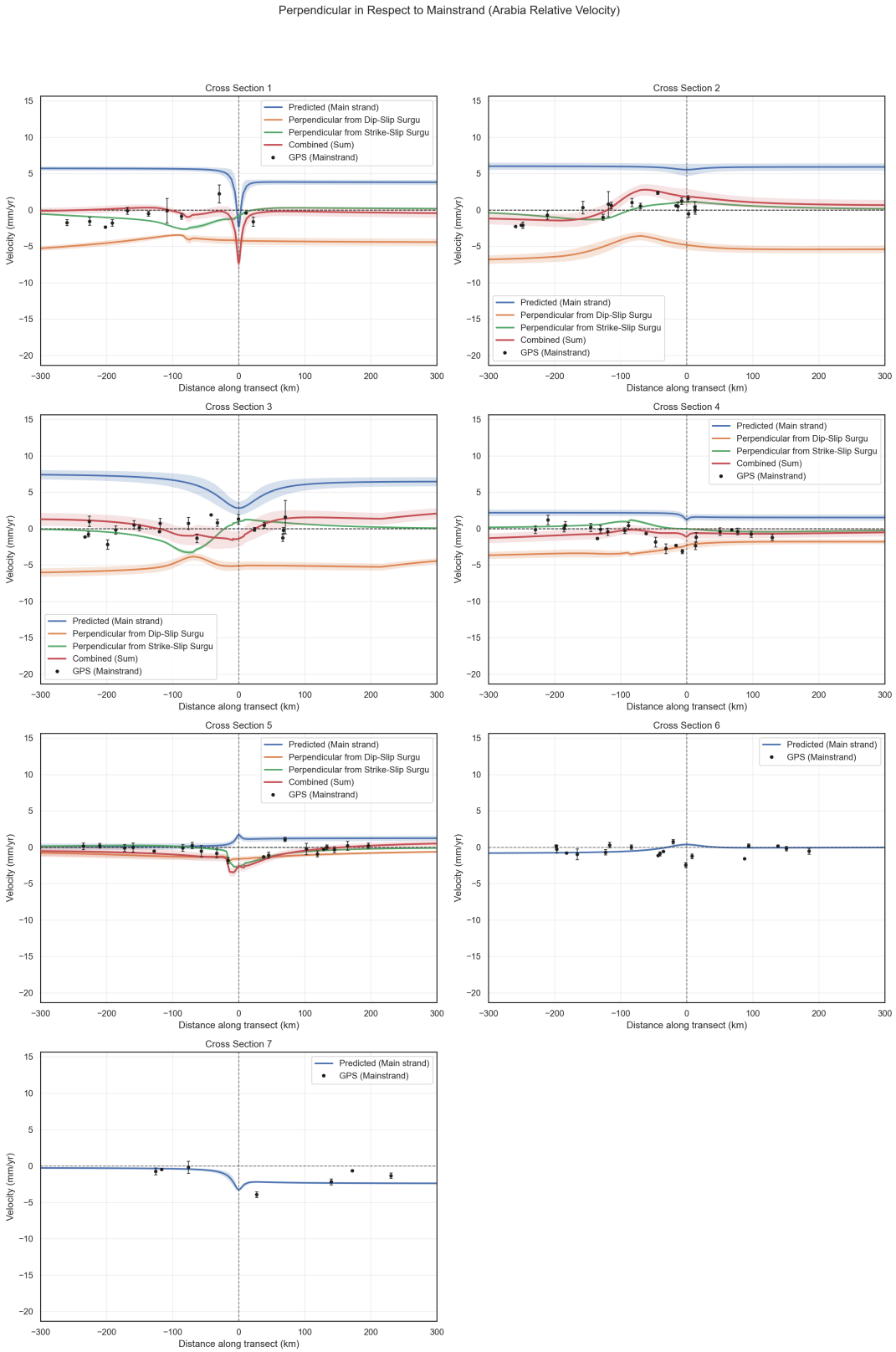

Figure 6.8: Perpendicular w.r.t Main Strand EAFZ (Arabia Relative Velocity)

6.5.4. Velocity Profiles Perpendicular to Çardak-Sürgü Fault

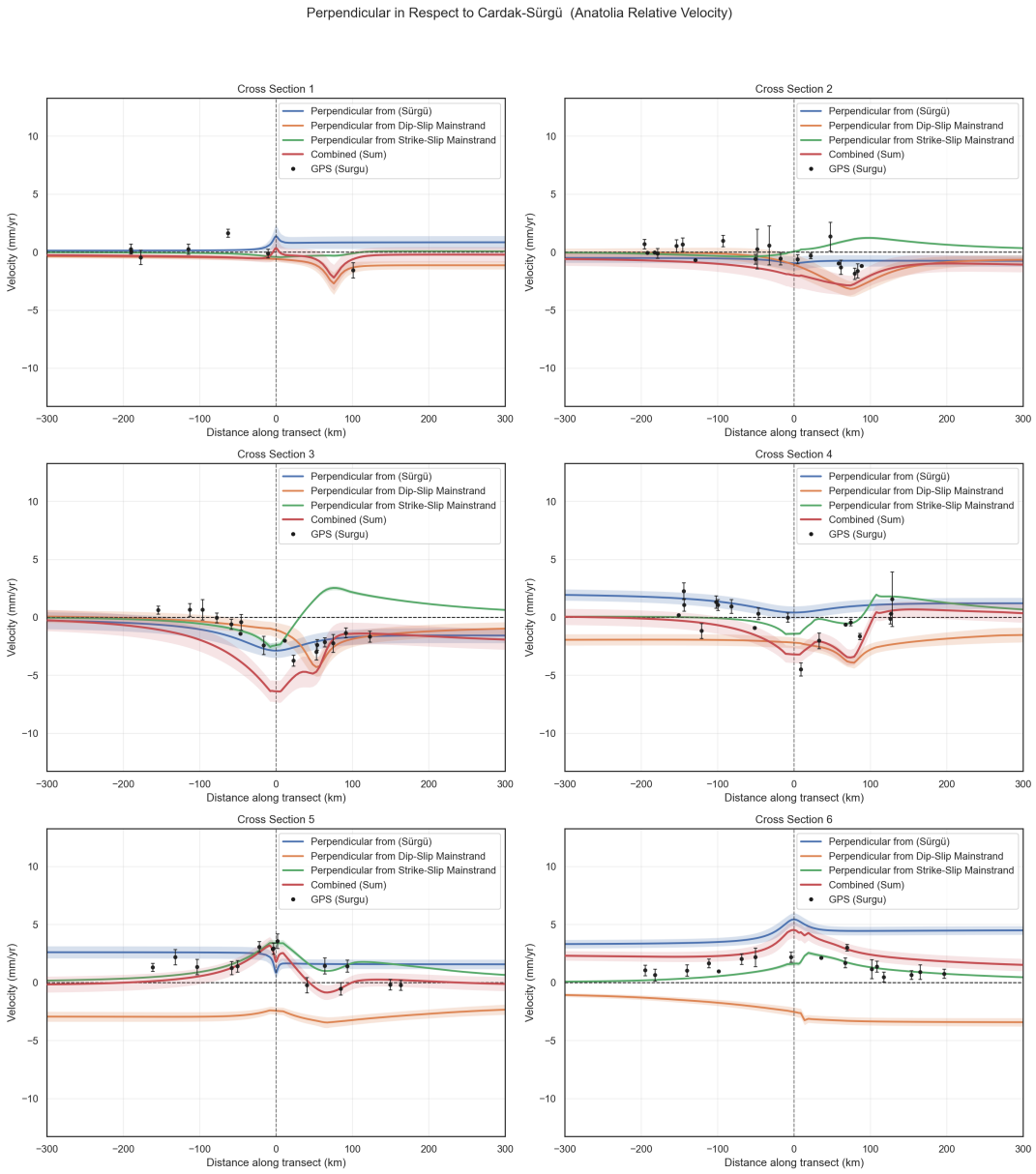

Figure 6.9: Perpendicular w.r.t Çardak-Sürgü (Anatolia Relative Velocity)

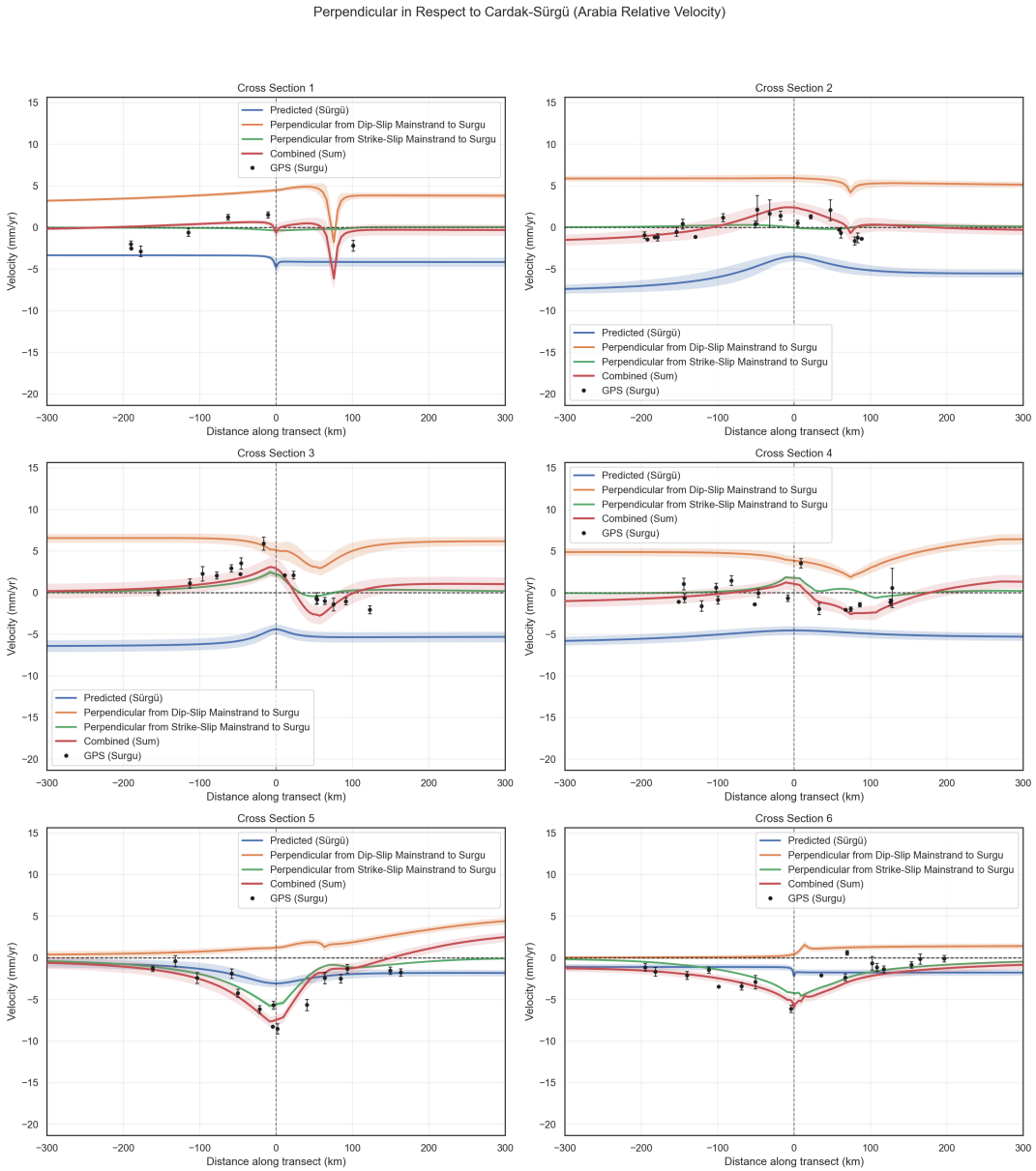

Figure 6.10: Perpendicular w.r.t Çardak-Sürgü (Arabia Relative Velocity)

The red line represents the resultant sum of all perpendicular component contributions. These include the perpendicular component estimated from the dip-slip model at its own cross-section, the perpendicular component contributions from other faults, and the perpendicular component arising from the strike-slip of other faults. The dashed line represents the fault that serves as the reference for each profile. In Figure 6.7 and Figure 6.8, the dashed line at zero marks the location of the main strand, since the figure shows the perpendicular component relative to the Main Strand. In Figure 6.9 and Figure 6.10, the dashed line indicates the location of the Çardak–Sürgü Fault, as the figure displays the perpendicular component relative to that fault.

6.6. Metrics

6.6.1. Mean Absolute Error

Since velocity can result in both negative and positive values, we used the mean absolute error (MAE) to assess the average differences between the posterior mean and the observed data. The model outputs the velocity in north (N) and east (E) components, so we also presented the MAE for these

decomposed E and N components. The MAE is obtained from both model setups.

Table 6.5: Mean Absolute Error (MAE) of velocity components relative to Anatolia and Arabia.

Component	Anatolia (mm/yr)	Arabia (mm/yr)
Northing	0.92	0.82
Easting	0.77	0.77
Total MAE	1.69	1.59

6.6.2. RMSE

Similar to the principle of MAE that the model outputs the velocity in (N) and (E) components, we'll also present the RMSE in the decomposed E and N components.

Table 6.6: Root Mean Square Error of Velocity Components

Component	Anatolia (mm/yr)	Arabia (mm/yr)
Northing	1.18	1.05
Easting	1.02	1.05
Total	1.56	1.49

6.6.3. RMSE for Every Cross Section Profile

A root mean square is also done on every profile of the cross sections that are shown earlier on section 6.5.

Table 6.7: Root Mean Square Error (RMSE) of model predictions relative to Anatolia and Arabia, computed for each cross-section.

Cross Section	Anatolia (mm/yr)	Arabia (mm/yr)
Mainstrand–Parallel 1	1.27	2.5
Mainstrand–Parallel 2	1.23	0.7
Mainstrand–Parallel 3	0.89	1.5
Mainstrand–Parallel 4	0.76	1.11
Mainstrand–Parallel 5	1.37	1.98
Mainstrand–Parallel 6	1.08	1.09
Mainstrand–Parallel 7	0.87	0.98
Sürgü–Parallel 1	1..37	1.65
Sürgü–Parallel 2	1.18	0.87
Sürgü–Parallel 3	0.74	1.21
Sürgü–Parallel 4	0.56	1.05
Sürgü–Parallel 5	0.94	1.26
Sürgü–Parallel 6	0.81	4.71
Mainstrand–Perpendicular 1	1.43	1.46
Mainstrand–Perpendicular 2	1.4	1.23
Mainstrand–Perpendicular 3	1.56	1.69
Mainstrand–Perpendicular 4	1.72	1.15
Mainstrand–Perpendicular 5	1.05	0.76
Mainstrand–Perpendicular 6	1.22	0.97
Mainstrand–Perpendicular 7	0.78	1.01
Sürgü–Perpendicular 1	0.94	1.91
Sürgü–Perpendicular 2	1.59	0.97
Sürgü–Perpendicular 3	2.29	1.53
Sürgü–Perpendicular 4	1.73	1.25
Sürgü–Perpendicular 5	1.06	1.37
Sürgü–Perpendicular 6	1.24	1.28

6.7. Discussion

6.7.1. Analysis on Estimated Strike-Slip and Dip-Slip

The estimated parameters from the model, relative to both Arabia and Anatolia, indicate a positive slip-deficit for the strike-slip component. This implies that the overall trajectory of slip-deficit along the Çardak–Sürgü Fault and the main strand of the EAFZ is left-lateral strike-slip. The use of GNSS velocities relative to Arabia and Anatolia consistently supports this left-lateral strike-slip behaviour. These results support that the Çardak–Sürgü Fault are moving left-laterally, aligns with the theory provided from Duman and Emre (2013) and opposite to Koç and Kaymakcı (2012).

In contrast, the dip-slip component yields variable results, with both positive and negative values, and the Arabia- and Anatolia-fixed reference frames do not agree on its magnitude or direction. This suggests that one of the fixed reference frames, or both of them, does not adequately capture the perpendicular motion necessary to resolve the dip-slip. The use of a deterministic assumption for the dip angle could also contribute, as noted in chapter 4, since dip-slip is highly sensitive to dip angle. Especially the Amanos segments, there's not much study that looks at the dip-angle in that area, most just assume that the Amanos segments are a vertical fault that has a dip around 90^0, to accommodate this, we already applied a dip around 85^0 for those particular segments.

The estimated strike-slip rates along the main strand of the EAFZ in this study range between 2-8 mm/year using the data relative to Anatolia and 0-11 mm/year with Arabia relative velocity (see Table 6.1 and Table 6.2). The estimated strike-slip rates along the Çardak–Sürgü Fault in this study range between 1-4 mm/year using the data relative to Anatolia and 2-11 mm/year with Arabia relative velocity (see Table 6.3 and Table 6.4). Using GNSS velocities relative to the Arabia frame generally produces higher strike-slip rates for the Çardak–Sürgü. Along the Amanos segment, the slip deficit is estimated at roughly 5 mm/year using data relative to the Anatolia frame and 6 mm/year in data relative to the Arabia frame. The slip-deficit rate obtained in this research is consistent with previous studies by Kurt et al. (2023) and Reilinger et al. (2006). They reported slip-deficit rates of 9–10 mm/year along the western part of the EAFZ, while Vavra et al. (2024) reported values of about 8–9 mm/year for the Pazarcık and Erkenek segments.

The estimated dip-slip along the main strand of the EAFZ varies from 0 to -12 mm/year when using the Anatolia-fixed frame, and from -12 to 2 mm/year when using the Arabia-fixed frame (see Table 6.1 and Table 6.2). For the Çardak–Sürgü Fault, dip-slip results also vary along the fault, ranging from –4 to 5 mm/year in the Anatolia-fixed frame (see Table 6.3) and from –3 to 10 mm/year in the Arabia-fixed frame (see Table 6.4). These values are different from the small dip-slip reported by Özbey et al. (2024), but align with the contraction rate of the eastern section of the main strand of East Anatolia Fault Zone reported by Reilinger et al. (2006) with -5 mm/year. The dip-slip results in segment 2 of both faults are higher than in other sections, likely because the tectonic influence of the Kyrenia Arc subduction zone contributes in this area (see Figure 1.1 for fault location)

The higher slip-deficit and dip-slip deficit values in Amanos arise partly because our model incorporates the Toprakkale Fault, an extension of the Çardak–Sürgü Fault located north of the EAFZ main strand, so we also took into account the mechanism from other faults.

6.7.2. Locking Depth

One notable observation from this inversion process is the variability in the locking depths. The posterior results from the data assimilation range from 1 km to 160 km for the Çardak–Sürgü fault using Arabia's relative velocity. In cross-section 4, it is shown that the locking depth reaches 160 km, which is physically unlikely, since reported values for this area are significantly smaller. A depth of around 100 km could indicate that the fault is subjected to creeping; however, we have not analysed this behaviour in detail, so no firm conclusion on creeping can be drawn at this stage. What is clear is that the model and the observations, particularly when using the Arabia-relative velocity frame, are not able to constrain the locking depth effectively for the Çardak–Sürgü Fault. In contrast, when using the Anatolia-relative data, the locking depth appears to be better constrained. This discrepancy may arise from the lack of near-field GNSS stations, or simply from limitations in the chosen reference frame; that is, using the velocity relative to Arabia does not provide sufficient information to resolve the parameter locking depth for the Çardak–Sürgü fault. The DA process tends to produce results that best fit the

model while disregarding the physical possibility of the locking depth. Although we attempted to set the prior for the locking depth consistent with values reported in previous studies, the posterior deviated significantly, indicating that the available GNSS data provide insufficient constraint. Previous studies have also acknowledged this limitation. For example, Hussain et al. (2018) and Aktug et al. (2016) either assumed a fixed locking depth or applied a grid-search approach to find the locking depth.

6.7.3. Analysis on Velocity Profile Cross Sections

The velocity profiles for each cross-section illustrate how well the model fits the observations in every cross-section. In section 6.5, the red line represents the resultant of all contributing components affecting the estimation at each cross-section. The RMSE values for each cross-section are summarised in Table 6.7. In cross-section 1 of the velocity profile (see section 6.5), some observations align more closely with the predictions from the Çardak–Sürgü Fault, as they are not fully weighted by the main strand. This occurs because, in our model, the influence of the Çardak–Sürgü Fault extends further west than the main strand, meaning certain observations are only partially weighted by the main strand mechanism. A similar principle is observed in the east, particularly in cross-section 6, where the East Anatolian Fault extends further eastward. In this case, some observations align more closely with the main strand than with the combined resultant, which reflects the influence of the weighting scheme. In cross sections 1 and 2, we can observe that there is a lack of data on the Arabian plate; this can explain the lack of constraint for the dip-slip model in this area.

When examining the model relative to Anatolia, the velocity transition to the Sürgü Fault appears to occur at x<=0. This is because, in our reference system, the Sürgü Fault is located before the Main Strand (see Figure 6.5). And when the velocity profile is considered from the Sürgü Fault perspective, the influence of the main strand begins to appear only after x=>0. (see Figure 1.1) for the location of the fault.

The profiles generally show that the strike-slip model exhibits better fits, as evidenced by the RMSE for each cross-section profile presented in subsection 6.6.3. The strike-slip model consistently demonstrates smaller RMSE values because the GNSS observations, in both the Anatolia- and Arabia-fixed frames, capture the strike-parallel signal better. However, at cross-section 5 of the Çardak–Sürgü Fault in the Arabia-fixed frame, an anomaly is observed where the model fails to reproduce the observations. The anomaly on cross-section 5 possibly occurs because the manner in which we compared the same velocity is to make them appear in the same space, similar to the linear weighting procedures, we can observe from section 5.3. As the cross-section 5 is bound by different weighting on the other side of the fault, this could be one of the causes, but it still does not explain the error since the velocity relative to Anatolia and other sections does not exhibit similar behaviour.

From the results, it can be observed that the Arabia-fixed frame does not constrain the Çardak–Sürgü Fault effectively. Consequently, the data assimilation, which incorporates observational data to improve parameter estimation, performs better using the data in relation to Anatolia. The perpendicular velocity showing poor constraint could also come from another factor influencing the dip-slip estimates, which is the dip angle (δ) assumed in this research. As discussed in Section 4, the modelled dip-slip signal is highly sensitive to δ. Since δ remains an assumption, and previous studies have not reached a consensus on the dip angle for either fault (Balkaya et al., 2023; Duman & Emre, 2013; Güvercin et al., 2022; Özbey et al., 2024; Vavra et al., 2024).

6.7.4. Comparison of Model Set-ups

This research uses two model set-ups as shown in chapter 4. Both on global RMSE, the two models set up show similar results (see Table 6.6 and Table 6.7). But the use of the Anatolia-fixed reference frame provides more reliable results, with parameters, particularly the locking depth, being better constrained compared to the data assimilation using velocities relative to Arabia. Overall, we can conclude that while both datasets allow us to obtain reasonable estimates for the Main strand, the inversion process fails to effectively constrain the locking depth of the Çardak–Sürgü Fault, especially using the Arabia-fixed frame reference.

6.7.5. Offset Term

The parameters α and β are included in the model to account for forces related to the fault mechanism that are not explained by the main slip-deficit term. This is evident from the fact that the observed velocities relative to both the Anatolia- and Arabia-fixed frames are not zero. In other words, plate velocities in the region are influenced not only by far-field plate motion but also by local tectonic effects. Differences in the magnitude of α and the variability in β indicate that each segment is also influenced with varying effects. As noted in section 2.1, the study area contains a complex fault network, so contributions from multiple sources are to be expected. At this stage, however, the scope of this research does not allow for a more detailed explanation of these additional driving forces.

6.7.6. Comparison of Estimated Slip Deficit and Coseismic Slip in the 2023 Kahramanmaraş Earthquake Doublet

In this research, the coseismic slip distribution used is taken from (Jia et al., 2023; Vavra et al., 2024). Vavra et al. (2024) estimated the coseismic slip by averaging over multiple finite-fault models. They computed the average slip on each fault segment by conserving the total seismic moment of the inversion results and normalising by the effective seismogenic thickness above the inferred locking depth. Their results provide average slip estimates for five fault segments: Amanos, Pazarcık, Erkenek, Göksun, and Çardak.

Table 6.8: Coseismic slip for each fault segment (Jia et al., 2023; Vavra et al., 2024)

Fault segment	Coseismic slip (m)
Pazarcık	5.6 ± 1.0
Erkenek	3.7 ± 0.6
Amanos	2.0 ± 0.5
Çardak	4.7 ± 0.7
Göksun	4.0 ± 1.2

Using the estimated dates of the last earthquakes from Duman and Emre (2013) and Vavra et al. (2024), we compute the interval between the 2023 Kahramanmaraş doublet earthquake and the most recent earthquake on each segment. The total slip-deficit for each segment is calculated as the square root of the sum of squared strike-slip and dip-slip components, and this value is then multiplied by the time interval to obtain a comparable measure of expected coseismic slip. This comparison provides a basis to assess whether the slip-deficit estimates tend to underpredict or overpredict the observed coseismic slip.

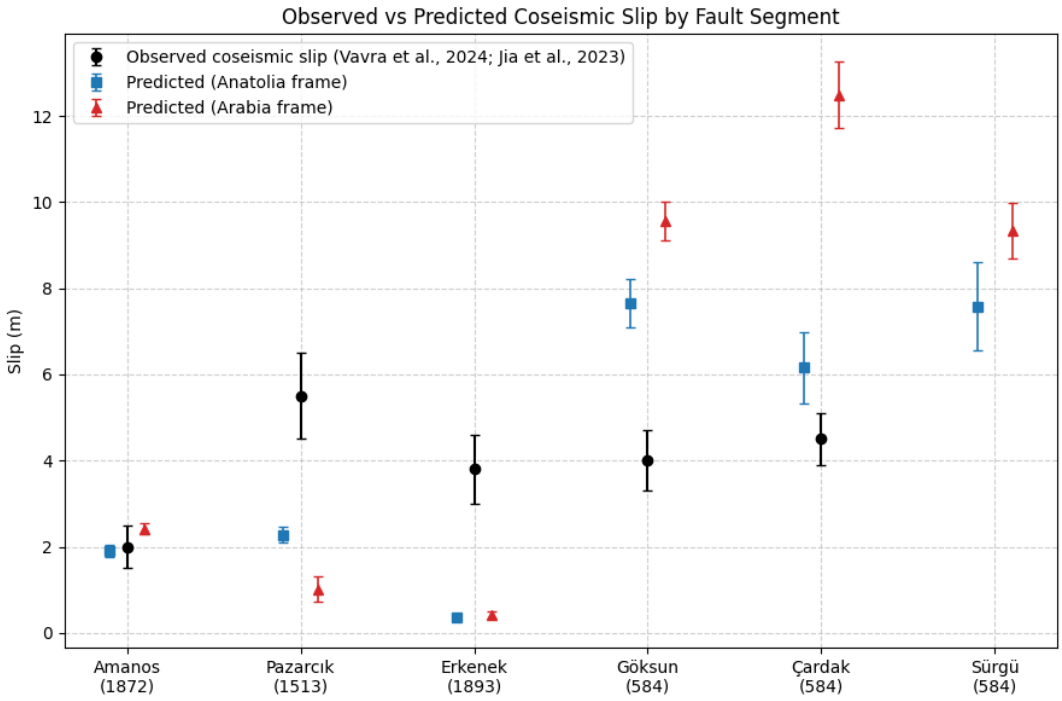

Figure 6.11: Comparison from the observed coseismic slip from Jia et al. (2023) and Vavra et al. (2024) with the obtained coseismic slip from this study

The Amanos and Çardak segments show consistency between the estimated slip budget and the observed slip, suggesting that the recurrence-based approach is reasonable for these faults. For the Erkenek and Pazarcık segment, however, the estimates appear to underpredict the observed coseismic slip. One possible explanation is that the timing of the last earthquakes reported for these segments may be underestimated, and that the actual events could have occurred earlier than the suggested years in the historical record.

In the case of the Çardak segment, the slip budget remains consistent provided that the 584 CE earthquake is taken as the most recent event on that fault, while the Göksun slip budget is overestimated. We can also observe that using the relative Arabia velocity resulted in overestimation of the coseismic slip prediction in the Çardak–Sürgü fault.

6.7.7. Limitation

The estimation of strike-slip and dip-slip using data assimilation generally works well, especially for the strike-slip estimation, but several limitations remain. First, the locking depth is poorly constrained. Second, the sensitivity of the results is strongly affected by the availability and distribution of GPS data. As shown in this study, identifying which GPS stations are influenced by both fault mechanisms plays a critical role, since even small changes in assigning stations to one or both faults can significantly change the estimated parameters. Choosing which GPS stations are affected by both fault kinematics is also influenced by the kinematics of our fault setup. It can be clearly seen that we attempted to extend the Çardak–Sürgü fault up to the Kyrenia Arc Subduction, similar to Özbey et al. (2024). Having a different kinematics setup will present different results.

Finally, the differences in results obtained under different relative reference frames highlight that the choice of velocity frame has a major impact on the estimation of the parameters.

6.7.8. Recommendation

From the results obtained, we can observe that the GPS stations reported by (Kurt et al., 2023), transformed into both Arabia- and Anatolia-fixed reference frames, do not provide a consistent basis to resolve the perpendicular velocity components that constrain the dip-slip model. Moreover, the lack of

GPS observations near-fault stations, particularly along segments of Çardak–Sürgü, limits the ability to constrain slip-deficit and locking depth estimates, especially when using an Arabia-fixed reference frame. A simple recommendation would be to reduce the number of cross sections used, so the obtained cross-section is constrained by more data or use the data of the GNSS in relation to Eurasia for the model setup, as other research has done (Aktug et al., 2016; Kurt et al., 2023).

Another kinematic set-up could improve the model output, for example, by including the Tuzgölü or Malatya Fault and avoiding a long extension of the Çokak or Toprakkale Fault. It may also be more appropriate to apply an open grid-search approach for locking depth, or to extend the grid-search to both locking depth and dip angle, rather than treating these parameters as fully free variables in the inversion, as the data that are available now are unable to constrain the locking depth. A further recommendation is to increase the number of near-fault observations, particularly along the Çardak–Sürgü Fault, or to integrate complementary datasets such as InSAR, as their observations are continuous in space, which allows us to obtain an observation at the near fault, albeit with some trade-off.

7

Conclusion

The 2D elastic dislocation model of Savage and Burford (1973), with dip-slip provided from Segall (2013), allowed us to jointly estimate strike-slip and dip-slip components along the main strand of the EAFZ and the Çardak–Sürgü Fault. Using the Ensemble Kalman Smoother for inversion of GNSS velocities (Kurt et al., 2023), I obtained interseismic parameter estimates that can be compared against coseismic slip from previous studies. Although the limited spatial distribution of GNSS stations has some limitations, the analysis provides some valuable information regarding the mechanism in the area.

7.1. What is the estimated slip-deficit rate along the EAFZ and Çardak–Sürgü Fault during the interseismic period?

The estimated parameters confirm the predominantly left-lateral strike-slip character of the EAFZ. In general, the strike-slip estimates for both faults indicate that the results obtained using Anatolia-relative velocities are more consistent with previous research. Dip-slip estimates show a mixture of normal and reverse components, highlighting the kinematics of extension and compression in the area. The slip-deficit rates for the EAFZ are estimated at 2–8 mm/yr using GNSS velocities relative to Anatolia, and 0–11 mm/yr using velocities relative to Arabia. For the Çardak–Sürgü Fault, slip-deficit rates are 1–4 mm/yr in the Anatolia-fixed frame and 2–11 mm/yr in the Arabia-fixed frame. Dip-slip rates show wider variability, ranging from 0 to –12 mm/yr in the Anatolia-fixed frame and from –12 to 2 mm/yr in the Arabia-fixed frame. For the Çardak–Sürgü Fault, dip-slip rates range from –4 to 5.5 mm/yr in the Anatolia-fixed frame and from –3 to 10 mm/yr in the Arabia-fixed frame.

Locking depth estimates vary between ∼30–50 km across segments, consistent with seismogenic thickness, especially along the main strand of the EAFZ. However, some results—most notably the locking depth of Çardak–Sürgü estimated using Arabia-relative velocities—yield values far from the estimated ones, that is, around ∼200. The Anatolia-relative solution also produces locking depths of around 50 km, which is higher than the usual estimates for the EAFZ, typically around 25 km.

7.2. How well does each model set-up fit the observation data for this research?

Using both model setups for the Anatolia and Arabia frames, they show a good model fit, indicated by small RMSE values. However, a closer look reveals that the estimated locking depth, especially using the Arabia reference frame, is poorly constrained, leading to some values of locking depth being around 100km and 160km. The results show that the parallel strike-slip model captures the strike-slip component better than the dip-slip model. This occurs because the strike-slip mechanism plays a more dominant role in the area, and the observations reflect it more clearly. As the EnKS incorporates the observations to improve the estimation of the parameters, the strike-slip outputs therefore perform better than the dip-slip estimates. The dip-slip estimation, on the other hand, is additionally influenced

by the assumed dip angle for each segment, which remains debated. In particular, for the Amanos segment, most studies simply assume a $90°$ dip due to the lack of studies regarding the dip angle at that location.

7.3. How does the estimated slip-deficit align with the 2023 Kahramanmaraş earthquake doublet?

Using the slip-deficit values obtained from the joint inversion, I find that the Amanos and Sürgü segments show slip-deficit accumulation consistent with the predicted coseismic slip and the timing of the most recent earthquakes, particularly when using velocities relative to Anatolia. However, some segments, particularly Erkenek and Pazarcık, exhibit an undershoot of the predicted coseismic slip, while Göksun shows an overshoot. In contrast, when using velocities relative to Arabia, the results tend to overshoot the predicted slip across all Çardak–Sürgü segments.

References

Aktug, B., Ozener, H., Dogru, A., Sabuncu, A., Turgut, B., Halicioglu, K., Yilmaz, O., & Havazli, E. (2016). Slip rates and seismic potential on the east anatolian fault system using an improved gps velocity field. *Journal of Geodynamics*, *94-95*, 1–12. https://doi.org/https://doi.org/10.1016/j.jog.2016.01.001

Ambraseys, N. N., & Jackson, J. A. (1998). Faulting associated with historical and recent earthquakes in the eastern mediterranean region. *Geophysical Journal International*, *133*(2), 390–406. https://doi.org/10.1046/j.1365-246x.1998.00508.x

Arpat, E., & Saroglu, F. (1972). The east anatolian fault system; thoughts on its development. *Bulletin of the Mineral Research and Exploration Institute of Turkey*, *78*, 33–39.

Balkaya, M., Akyüz, H. S., & Özden, S. (2023). Paleoseismology of the sürgü and çardak faults – splays of the eastern anatolian fault zone, türkiye. *Turkish Journal of Earth Sciences*, *32*(3), Article 11. https://doi.org/10.55730/1300-0985.1851

Carrassi, A., Bocquet, M., Bertino, L., & Evensen, G. (2018). Data assimilation in the geosciences: An overview of methods, issues, and perspectives. *WIREs Climate Change*, *9*(5), e535. https://doi.org/10.1002/wcc.535

Dong, Y., Hui, B., Wang, B., Sun, S., Yao, H., Liu, J., Zang, R., Li, Y., & Luo, Q. (2025). Transform faults and transfer faults: Plate boundary and intra-continental tectonic dynamics transition [Published online June 18, 2025]. *Science China Earth Sciences*, *68*. https://doi.org/10.1007/s11430-024-1536-7

Duman, T. Y., & Emre, Ö. (2013). The east anatolian fault: Geometry, segmentation, and jog characteristics [Supplementary material available at www.geolsoc.org.uk/SUP18568]. *Journal of Geological Research*.

Eagles, G. (2020). Chapter 4 - plate boundaries and driving mechanisms. In N. Scarselli, J. Adam, D. Chiarella, D. G. Roberts, & A. W. Bally (Eds.), *Regional geology and tectonics (second edition)* (Second Edition, pp. 41–59). Elsevier. https://doi.org/https://doi.org/10.1016/B978-0-444-64134-2.00004-3

Emre, T., Tavlan, M., Akkiraz, M. S., & İsintek, İ. (2011). Stratigraphy, sedimentology and palynology of the neogene–pleistocene rocks around akçaşehir–tire–izmir (küçük menderes graben, western anatolia). *Turkish Journal of Earth Sciences*, *20*, 27–56.

Ergintav, S., Floyd, M., Paradissis, D., Karabulut, H., Vernant, P., Masson, F., Georgiev, I., Konca, A. Ö., Doğan, U., King, R., & Reilinger, R. (2023). New geodetic constraints on the role of faults and blocks vs. distribute strain in the nubia-arabia-eurasia zone of active plate interactions. *Turkish Journal of Earth Sciences*, *32*(3), 248–261. https://doi.org/10.55730/1300-0985.1842

Evensen, G., Vossepoel, F. C., & van Leeuwen, P. J. (2022). *Data assimilation: Methods, algorithms, and applications* [Open Access under Creative Commons Attribution 4.0 International License]. Springer Nature Switzerland AG. https://doi.org/10.1007/978-3-030-96709-3

Freed, A. M. (2007). Afterslip (and only afterslip) following the 2004 parkfield, california, earthquake. *Geophysical Research Letters*, *34*(6), L06312. https://doi.org/10.1029/2006GL029155

Golriz, D., Bock, Y., & Xu, X. (2021). Defining the coseismic phase of the crustal deformation cycle with seismogeodesy. *Journal of Geophysical Research: Solid Earth*, *126*(12), e2021JB022002. https://doi.org/10.1029/2021JB022002

Govers, R., Furlong, K. P., van de Wiel, L., Herman, M. W., & Broerse, T. (2018). The geodetic signature of the earthquake cycle at subduction zones: Model constraints on the deep processes. *Reviews of Geophysics*, *56*(1), 49–76. https://doi.org/10.1002/2017RG000586

Guidoboni, E., Comastri, A., & Traina, G. (1994). *Catalogue of ancient earthquakes in the mediterranean area up to the 10th century*. ING, Roma – SGA, Bologna.

Güvercin, S. E., Karabulut, H., Konca, A. Ö., Doğan, U., & Ergintav, S. (2022). Active seismotectonics of the east anatolian fault. *Geophysical Journal International*, *230*(1), 50–69. https://doi.org/10.1093/gji/ggac045

Herman, M. W., Furlong, K. P., & Govers, R. (2018). The accumulation of slip deficit in subduction zones in the absence of mechanical coupling: Implications for the behavior of megathrust earthquakes. *Journal of Geophysical Research: Solid Earth*, *123*(9), 6206–6222. https://doi.org/10.1029/2018JB016336

Hu, Y., & Wang, K. (2016). Stress driven relaxation of heterogeneous upper mantle and time□dependent afterslip: Application to postseismic deformation. *Journal of Geophysical Research: Solid Earth*, *121*(4), 3171–3192. https://doi.org/10.1002/2015JB012508

Hussain, E., Wright, T. J., Walters, R. J., Bekaert, D. P. S., Lloyd, R., & Hooper, A. (2018). Constant strain accumulation rate between major earthquakes on the north anatolian fault. *Nature Communications*, *9*. https://doi.org/10.1038/s41467-018-03739-2

Jia, Z., Jin, Z., Marchandon, M., Ulrich, T., Gabriel, A.-A., Wang, W., et al. (2023). The complex dynamics of the 2023 kahramanmaraş, turkey, $M_w 7.8 7.7 earthquake doublet$. *Science*, *381*(6661), 985–990. https://doi.org/10.1126/science.adi0685

Katzfuss, M., Stroud, J. R., & Wikle, C. K. (2016). Understanding the ensemble kalman filter. *The American Statistician*, *70*(4), 350–357. https://doi.org/10.1080/00031305.2016.1141709

Kiratzi, A. A. (1993). A study on the active crustal deformation of the north and east anatolian fault zones. *Tectonophysics*, *225*(1-2), 191–203. https://doi.org/10.1016/0040-1951(93)90285-A

Koç, A., & Kaymakcı, N. (2012). Kinematics of sürgü fault zone (malatya, turkey): A remote sensing study [Received: 11 January 2012, Revised: 3 August 2012, Accepted: 4 August 2012, Available online: 13 August 2012]. *Tectonophysics*, *576*, 88–99. https://doi.org/10.1016/j.tecto.2012.08.001

Koç, A., & Kaymakcı, N. (2013). Kinematics of sürgü fault zone (malatya, turkey): A remote sensing study. *Journal of Geodynamics*, *65*, 292–307. https://doi.org/10.1016/j.jog.2012.08.001

KOERI-RETMC. (2021). Boğaziçi university kandilli observatory and earthquake research institute – regional earthquake-tsunami monitoring center [Accessed: 2025-09-09].

Kurt, A. İ., Özbakır, A. D., Cingöz, A., Ergintav, S., Doğan, U., & Özarpacı, S. (2023). Contemporary velocity field for turkey inferred from combination of a dense network of long term gnss observations. *Turkish Journal of Earth Sciences*, *32*, 275–293. https://doi.org/10.55730/1300-0985.1844

Marone, C. J., Scholz, C. H., & Bilham, R. (1991). On the mechanics of earthquake afterslip. *Journal of Geophysical Research: Solid Earth*, *96*(B5), 8441–8452. https://doi.org/10.1029/91JB00275

McGrayne, S. B. (2011). *The theory that would not die: How bayes' rule cracked the enigma code, hunted down russian submarines, and emerged triumphant from two centuries of controversy*. Yale University Press.

Miyamoto, H. K., Sechi, G. J., Victor, G., St Come, B., Broughton, M., Gilani, A. S. J., & Singh, A. (2024). Haiti earthquake 2021: Findings from the repair and damage assessment of 179,800 buildings. *International Journal of Disaster Risk Reduction*, *101*, 104402. https://doi.org/10.1016/j.ijdrr.2024.104402

Özbey, V., Sëngör, A. M. C., Henry, P., Özeren, M. S., Haines, A. J., Klein, E. C., Tanı, E., Zabci, C., Chousianitis, K., Güvencin, S. E., & Ögretmen, N. (2024). Kinematics of the kahramanmaraş triple junction and of cyprus: Evidence of shear partitioning [Published online: 23 August 2024]. *BSGF – Earth Sciences Bulletin*, *195*(15), 1–15. https://doi.org/10.1051/bsgf/2024012

Palin, R. M., & Santosh, M. (2021). Plate tectonics: What, where, why, and when? *Gondwana Research*, *100*, 3–24. https://doi.org/10.1016/j.gr.2020.11.001

Perfettini, H., & Avouac, J.-P. (2004). Postseismic relaxation driven by brittle creep: A possible mechanism to reconcile geodetic measurements and the decay rate of aftershocks, application to the chi-chi earthquake, taiwan. *Journal of Geophysical Research: Solid Earth*, *109*(B2), B02304. https://doi.org/10.1029/2003JB002488

Pollitz, F. F., Wicks, C., & Thatcher, W. (2003). Mantle flow beneath a continental strike-slip fault: Postseismic deformation after the 1999 hector mine earthquake. *Science*, *293*(5536), 1814–1818. https://doi.org/10.1126/science.1061361

Pousse-Beltran, L., Nissen, E., Bergman, E. A., Cambaz, M. D., Gaudreau, É., Karasözen, E., & Tan, F. (2020). The 2020 M_w 6.8 elazığ (turkey) earthquake reveals rupture behavior of the east anatolian fault. *Geophysical Research Letters*, *47*(11), e2020GL088136. https://doi.org/10.1029/2020GL088136

Ramgraber, M. (2019). Analytic element method toolbox [Accessed: 2025-08-20].

Reid, H. F. (1910). *The mechanics of the earthquake: The california earthquake of april 18, 1906* (Vol. 2). Carnegie Institution of Washington.

Reilinger, R., McClusky, S., Vernant, P., Lawrence, S., Ergintav, S., Cakmak, R., Ozener, H., Kadirov, F., Guliev, I., Stepanyan, R., Nadariya, M., Hubia, G., Mahmoud, S., Sakr, K., ArRajehi, A., Paradissis, D., Al-Aydrus, A., Prilepin, M., Guseva, T., … Karam, G. (2006). Gps constraints on continental deformation in the africa-arabia-eurasia continental collision zone and implications for the dynamics of plate interactions. *Journal of Geophysical Research: Solid Earth*, *111*(B5), B05411. https://doi.org/10.1029/2005JB004051

Rossetto, T., Peiris, N., Pomonis, A., Wilkinson, S. M., Del Re, D., Koo, R., & Gallochor, S. (2007). The indian ocean tsunami of december 26, 2004: Observations in sri lanka and thailand. *Natural Hazards*, *42*(1), 105–124. https://doi.org/10.1007/s11069-006-9064-3

Savage, J. C., & Burford, R. O. (1973). Geodetic determination of relative plate motion in central california. *Journal of Geophysical Research*, *78*(5), 832–845. https://doi.org/10.1029/JB078i005p00832

Savage, J. C., & Prescott, W. H. (1978). Asthenosphere readjustment and the earthquake cycle. *Journal of Geophysical Research*, *83*(B7), 3431–3442. https://doi.org/10.1029/JB083iB07p03431

Scholz, C. H. (2002). The seismic cycle. In C. H. Scholz (Ed.), *The mechanics of earthquakes and faulting* (2nd ed., pp. 244–299). Cambridge University Press. https://doi.org/10.1017/CBO9780511818516.007

Segall, P. (2013). *Earthquake and volcano deformation* (1st). Princeton University Press.

Şengör, A. M. C., Grall, C., İmren, C., Le Pichon, X., Görür, N., Henry, P., Karabulut, H., & Siyako, M. (2014). The geometry of the north anatolian transform fault in the sea of marmara and its temporal evolution: Implications for the development of intracontinental transform faults. *Canadian Journal of Earth Sciences*, *51*, 222–242. https://doi.org/10.1139/cjes-2013-0160

Shen, L., Hooper, A., Elliott, J. R., & Wright, T. J. (2024). Variability in interseismic strain accumulation rate and style along the altyn tagh fault [Published online: 11 August 2024]. *Nature Communications*, *15*(6876). https://doi.org/10.1038/s41467-024-51116-z

Strack, O. D. L. (2003). Theory and applications of the analytic element method. *Reviews of Geophysics*, *41*(2), 1005. https://doi.org/10.1029/2002RG000111

Styron, R., & Pagani, M. (2020). The gem global active faults database. *Earthquake Spectra*, *36*(1_{suppl}), 160–180. https://doi.org/10.1177/8755293020944182

Taymaz, T., Jackson, J., & McKenzie, D. (1991). Active tectonics of the north and central aegean sea. *Geophysical Journal International*, *106*(2), 433–490. https://doi.org/10.1111/j.1365-246X.1991.tb03906.x

Uchida, N., & Bürgmann, R. (2021). A decade of lessons learned from the 2011 tohoku-oki earthquake. *Reviews of Geophysics*, *59*(2), e2020RG000713. https://doi.org/10.1029/2020RG000713

U.S. Geological Survey. (n.d.). Focal mechanisms [Accessed: 2025-07-31]. https://www.usgs.gov/programs/earthquake-hazards/focal-mechanisms-or-beachballs

Vavra, E., Fialko, Y., Bulut, F., Garagorri, A., Yalvaç, S., & Yaltırak, C. (2024). The 2023 m_w 7.8–7.7 kahramanmaraş earthquakes were loosely slip-predictable. *Communications Earth & Environment*, *5*(1), 680. https://doi.org/10.1038/s43247-024-01969-5

Zhang, Y., Eken, T., Tang, X., Liu, D., Taymaz, T., Guo, R., Zheng, Y., Wang, J., & Sun, H. (2023). Geometric controls on cascading rupture of the 2023 kahramanmaraş earthquake doublet [Published online: 12 October 2023]. *Nature Geoscience*, *16*(10), 739–746. https://doi.org/10.1038/s41561-023-01283-3

Zoback, M. L. (2006). The 1906 earthquake and a century of progress in understanding earthquakes and their hazards. *GSA Today*, *16*(4-5), 4–11. https://doi.org/10.1130/GSAT01604A.1

A

Appendix A

A.1. Data Assimilation Algorithm

The algorithm of the Ensemble Kalman Filter (EnKF).

Algorithm 5 Ensemble Kalman Filter (EnKF)

Input:
N: Number of ensemble members
$X_{k=0} = \{\mathbf{x}^i_{k=0}\}^N_{i=1}$: Initial ensemble at time step 0
$M(\cdot)$: Forecast model
$H(\cdot)$: Observation operator
$\mathbf{y}^{\text{obs}}_k$: Observation at time step k
$\mathbf{R}$: Observation error covariance
K: Number of assimilation time steps

Output: Updated ensemble $\{\mathbf{x}^i_k\}^N_{i=1}$ for each time step $k = 1, \ldots, K$
for $k = 1$ to K **do**
    Forecast Step:
    for $i = 1$ to N **do**
        $\mathbf{x}^{i,f}_k \leftarrow M(\mathbf{x}^i_{k-1}) + v^i_k$
        $\hat{\mathbf{y}}^{i,f}_k \leftarrow H(\mathbf{x}^{i,f}_k) + w^i_k$
    end for
    Stack forecast ensembles:
    $\mathbf{X}^f_k = [\mathbf{x}^{1,f}_k, \ldots, \mathbf{x}^{N,f}_k]$
    $\hat{\mathbf{Y}}^f_k = [\hat{\mathbf{y}}^{1,f}_k, \ldots, \hat{\mathbf{y}}^{N,f}_k]$
    Compute means:
    $\bar{\mathbf{x}}^f_k = \text{mean}(\mathbf{X}^f_k)$
    $\bar{\hat{\mathbf{y}}}^f_k = \text{mean}(\hat{\mathbf{Y}}^f_k)$
    Compute differences:
    $\mathbf{X}'_k = \mathbf{X}^f_k - \bar{\mathbf{x}}^f_k$
    $\hat{\mathbf{Y}}'_k = \hat{\mathbf{Y}}^f_k - \bar{\hat{\mathbf{y}}}^f_k$
    Estimate covariances:
    $\mathbf{P}_{xy,k} = \frac{1}{N-1}\mathbf{X}'_k(\hat{\mathbf{Y}}'_k)^\top$
    $\mathbf{P}_{yy,k} = \frac{1}{N-1}\hat{\mathbf{Y}}'_k(\hat{\mathbf{Y}}'_k)^\top$
    Compute Estimated Kalman gain:
    $\mathbf{K}_k = \mathbf{P}_{xy}(\mathbf{P}_{yy} + \mathbf{R})^{-1}$
    Analysis (Update) Step:
    for $i = 1$ to N **do**
        Sample: $\boldsymbol{\varepsilon}^i_k \sim \mathcal{N}(0, \mathbf{R})$
        $\mathbf{y}^i_k = \mathbf{y}^{\text{obs}}_k + \boldsymbol{\varepsilon}^i_k$
        $\delta^i_k = \mathbf{y}^i_k - \hat{\mathbf{y}}^{i,f}_k$
        $\mathbf{x}^{i,a}_k = \mathbf{x}^{i,f}_k + \mathbf{K}_k\delta^i_k$
    end for
    Set: $\mathbf{X}^a_k = \{\mathbf{x}^{1,a}_k, \ldots, \mathbf{x}^{N,a}_k\}$
end for

A.2. Table Prior of Parameters

Table A.1: Prior distribution parameters used for generating the dip-slip ensemble for Arabia Relative.

Parameter	Mean (μ)	Std.Dev(σ)
Strike-slip velocity, V_s	8	6
Dip-slip velocity, V_d	0	7
Locking depth, D	10	15
α	3	10
β	0	10

Table A.2: Prior distribution parameters used for generating the dip-slip ensemble for the Çardak–Sürgü Fault for Arabia Relative.

Parameter	Mean (μ)	Std.Dev (σ)
Strike-slip velocity, V_s	5	5
Dip-slip velocity, V_d	0	7
Locking depth, D	10	10
α	3	10
β	0	10

Table A.3: Prior distribution parameters used for generating the dip-slip ensemble for the Main Strand of the EAFZ for Anatolia Relative.

Parameter	Mean (μ)	Std.Dev (σ)
Strike-slip velocity, V_s	8	6
Dip-slip velocity, V_d	0	7
Locking depth, D	10	15
α	5	5
β	0	10

Table A.4: Prior distribution parameters used for generating the dip-slip ensemble for the Çardak–Sürgü Fault for the setup for Anatolia Relative.

Parameter	Mean (μ)	Std.Dev (σ)
Strike-slip velocity, V_s	5	5
Dip-slip velocity, V_d	0	7
Locking depth, D	10	10
α	5	10
β	0	10

B

Appendix B

A focal mechanism is a way to represent the geometry and mechanism of a fault in a simple diagram. It is used to show the type of slip-mechanism that was captured during an earthquake. The beachball generally describes the three main mechanisms of slip: strike-slip, normal, and thrust. The beachball also contains information about the orientation of the fault, as referred to in (U.S. Geological Survey, n.d.).

The focal mechanisms are obtained by solving the earthquake's moment tensor, which they estimate using multiple seismic wave observations. The method for deriving the moment tensor will not be discussed here, as we will focus on how to interpret the focal mechanism beachball and what it represents. Focal mechanism utilises a stereonet projection to represent fault plane orientations. Stereonet is a tool for projecting a 3D object to a two-dimensional surface using a lower hemisphere projection. A vertical plane on a stereonet appears as a straight line passing through the centre of the circle, while a steeply dipping plane produces a slightly curved line, and a shallow-dipping plane results in a more pronounced curve. The start and end points of the line indicate the orientation of the fault. The orientation referred to the clockwise direction from $0°$ to $360°$.

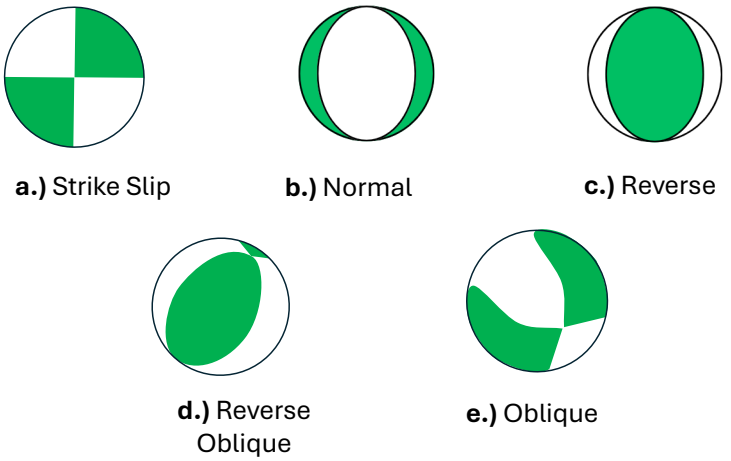

Figure B.1: Beachball Diagram. (Created by Author)

Figures B.1 show how each fault motion is represented in a beachball diagram. The upper left image shows a strike-slip fault, represented by symmetrical and orthogonal projections of the focal mechanism. The shaded green line represents compression, while the white line represents the dilatation

that occurs on the planes. The upper centre and right images show normal-slip and reverse-slip faulting, respectively. Notice that the shaded and unshaded regions are reversed between the normal and reverse mechanisms, indicating that the zones of dilatation and compression are reversed.

It is also possible for both strike-slip and dip-slip components (normal or reverse) to be present during an earthquake. This combination is known as oblique slip, where both types of movement occur simultaneously. Oblique slip is illustrated in the figure **d** and **e**. In a focal mechanism diagram, the position of the nodal plane intersections relative to the centre reflects the faulting style. Intersections located near the centre indicate a dominantly strike-slip mechanism, whereas intersections located toward the edges indicate a stronger dip-slip component. The focal mechanism solutions for the Kahramanmaraş earthquake doublet show that both events were primarily strike-slip, with only a minor dip-slip contribution.